Modeling X-ray pulsars in curved space-time

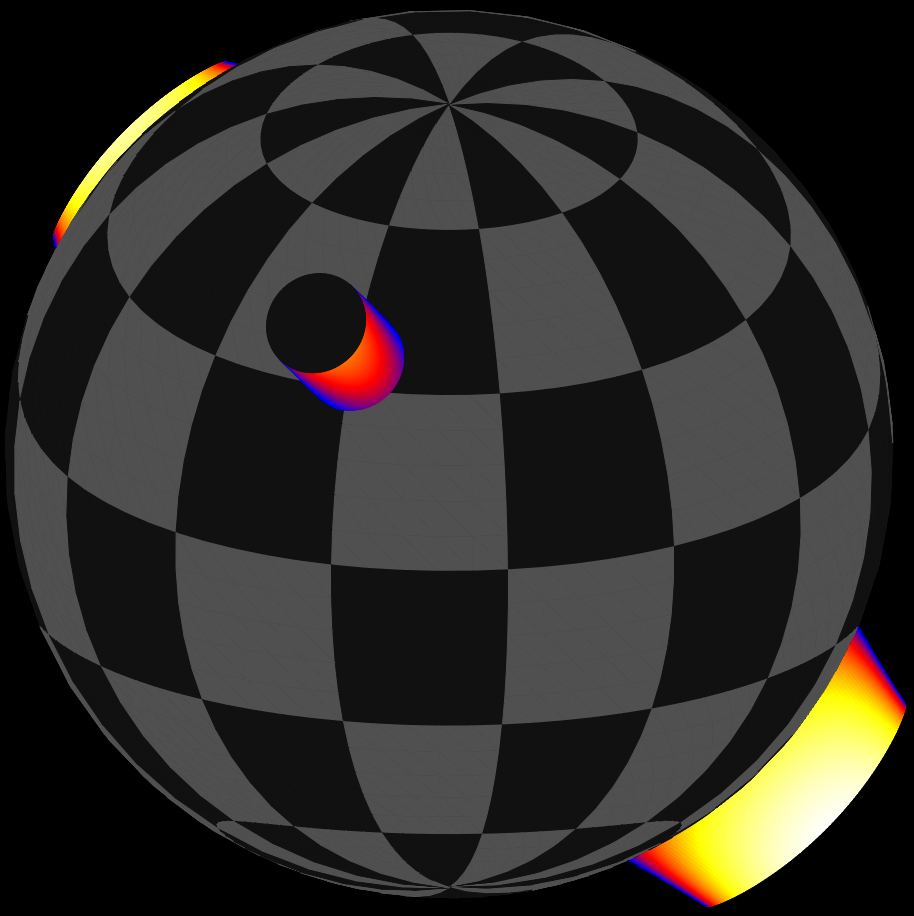

Sebastian Falkner

Modellierung von Röntgenpulsaren in gekrümmter Raumzeit

Modeling X-ray pulsars in curved space-time

Der Naturwissenschaftlichen Fakultät
der Friedrich-Alexander-Universität
Erlangen-Nürnberg

zur
Erlangung des Doktorgrades Dr. rer. nat.

vorgelegt von

Patrick Sebastian Phillippus Falkner

aus Erlangen

Als Dissertation genehmigt
von der Naturwissenschaftlichen Fakultät
der Friedrich-Alexander-Universität Erlangen-Nürnberg

Tag der mündlichen Prüfung: xx.xx.2018

Vorsitzender der Promotionsorgans: Prof. Dr. Georg Kreimer

Gutachter: Prof. Dr. Jörn Wilms
Prof. Dr. Silas Laycock

The cover picture shows the general relativistic projection of a highly magnetized accreting X-ray pulsar, which in this case is emitting from its two antipodal and identical accretion columns. The effect of light bending causes the visible surface of the neutron star to be enlarged and results in an apparent deformation and even double projection of the columns.

Zusammenfassung

Ich untersuche stark magnetisierte, akkretierende Röntgenpulsare in massereichen Doppelsternsystemen. In diesen Systemen umkreisen sich ein Neutronenstern und ein optischer Begleitstern in einer engen Umlaufbahn. Mit Massen von $\sim 1.4\,M_\odot$ und Radien von $\sim 10\,\mathrm{km}$ gehören Neutronensterne zu den kompaktesten Objekten, die uns bekannt sind. Die Raumzeit wird von Neutronensternen aufgrund ihrer Kompaktheit gekrümmt und kann nur unter der Einbeziehung der allgemeinen Relativitätstheorie beschrieben werden. Zusätzlich weisen diese Neutronensterne die stärksten beobachteten Magnetfelder ($\sim 10^{12}\,\mathrm{G}$) auf, nur überboten von Magnetaren. Der starke Wind des Begleiters wird von der Gravitation des Neutronensterns eingefangen und mit einer Massenrate von $\sim 10^{17}\,\mathrm{g\,s^{-1}}$ auf den Neutronenstern akkretiert. Das starke Magnetfeld zwingt das einfallende Plasma, den Feldlinien bis zu den magnetischen Polen zu folgen, wo sich Akkretionssäulen bilden. An den Polen wird die Materie gestoppt und dessen kinetische Energie im Röntgenbereich abgestrahlt. Die beobachteten Spektren lassen sich mit einem Potenzgesetz beschreiben und zeigen oft breite Absorptionlinien. Diese Linien sind auf zyklotronresonante Streuung an Elektronen zurückzuführen, die durch das starke Magnetfeld in Landau-Niveaus quantisiert sind. Dadurch, dass die Achsen des Magnetfeldes und der Rotation nicht immer übereinstimmen, sind Pulsationen von den lokal begrenzten Emissionsregionen an den Polen mit der Rotationsperiode im Bereich von 1 - 1000 s zu sehen.

Die physikalischen Eigenschaften dieser akkretierenden Pulsaren zu messen ist ein seit langer Zeit bestehendes Anliegen der Astrophysik. Dabei sind die Masse und der Radius des Neutronensterns von besonderem Interesse, sowie die physikalischen Bedingungen innerhalb der Akkretionssäule, wie z.B. die Magnetfeldstärke. Allerdings fehlen bis dato umfangreiche Modelle zur Beschreibung der Akkretionssäulenstruktur und der komplexen Strahlungsprozesse innerhalb dieser, was den Vergleich physikalischer Vorhersagen mit Beobachtungen erschwert. Ich kombiniere zum ersten Mal die physikalische Beschreibung der Akkretionssäule mit der vollständigen relativistischen Behandlung des Strahlungstransports im Gravitationsfeld des Neutronensterns. Dabei verwende ich ein Kontinuumsmodell, das von Postnov et al. (2015) in der Diffusionsnäherung für die dichten Regionen innerhalb der Säule berechnet wurde. Mit Hilfe des Codes von Schwarm et al. (2017a,b) wird in einer dünnen äußeren Schicht die zyklotronresonante Streuung berechnet, welche die beobachteten Absorptionslinien erzeugt. Schließlich wird der beobachtete pulsphasen- und energieabhängige Fluss unter Berücksichtigung allgemein relativistischer Effekte wie Lichtkrümmung und gravitative Rotverschiebung berechnet. Basierend auf diesem Modell diskutiere ich Schlußfolgerungen für messbare Größen. Ich zeige, dass die geometrische Konfiguration, d.h. die Inklination des Beobachters und die Position der Akkretionssäulen relativ zur Rotationsachse, einen signifikanten Einfluss auf diese Observablen hat und allgemein-relativistische Lichtkrümmung dabei eine wichtige Rolle spielt.

Die in dieser Arbeit vorgestellten Methode des Raytracings verwende ich außerdem in Verbindung mit einem einfachen phänomenologischen Emissionsprofil, um das Pulsprofil des Röntgenpulsars 4U 1626−67 und dessen energieabhängige Entwicklung zu erklären. Zusätzlich erkläre ich den Ursprung und die Pulsphasenabhängigkeit der beiden beobachteten Zyklotronlinien in GX 301−2 mit Hilfe eines einfachen Modells. Dieses Modell beschreibt

eine einzelne Säule mit zwei Emissionsregionen in verschiedenen Höhen. Aufgrund der Bewegung des einfallenden Materials unterliegt die Emission relativistischem Beaming. Mit der Abhängigkeit des Beamings vom Sichtwinkel, und damit der Pulsphase, wird die Variation der Zyklotronlinie erklärt.

Abstract

I investigate highly magnetized accreting X-ray pulsars in high mass X-ray binaries (HMXBs). These systems consist of a neutron star and an optical companion star in a close binary orbit. Neutron stars are among the most compact objects we know, with masses of $\sim 1.4\,M_\odot$ and radii of $\sim 10\,\mathrm{km}$. Due to their high compactness, space-time in the neutron star's close vicinity is not flat and general relativity is needed to describe it. Additionally, these pulsars exhibit one of the strongest magnetic fields ($\sim 10^{12}\,\mathrm{G}$) we have observed (only exceeded by Magnetars). The strong wind of the companion is captured by the gravitational well of the neutron star and is governed by its strong magnetic field. The captured matter is accreted with rates in the order of $\sim 10^{17}\,\mathrm{g\,s^{-1}}$ onto the neutron star itself. The infalling plasma is forced to follow the field lines onto the poles where accretion columns are formed. There the matter is stopped and its kinetic energy is radiated away in X-rays. The observed spectra exhibit a power-law like continuum and also often show broad absorption features caused by cyclotron resonant scattering off electrons, which are forced into quantized Landau levels by the strong magnetic field. Due to the localized emission region at the magnetic poles, which do not have to be aligned with the rotational axis, pulsations with the rotational period in the range of 1–1000 s are visible.

Measuring physical properties of accreting, strongly magnetized neutron stars has been a long-standing problem in astrophysics. These properties include the parameters of the neutron star such as its mass and radius, as well as the physical conditions within the accretion column, such as the magnetic field strength. The lack of detailed models for the structure of the accretion column and the complex radiative mechanisms inside the column have made it difficult to compare theoretical predictions with observations. I combine for the first time a physical treatment of the accretion column with a fully relativistic treatment of the radiative transfer in the neutron star's gravitational field. In particular, I use the seed photon continuum calculated by Postnov et al. (2015) in the diffusion approximation from the dense inner regions of the accretion column. This continuum is imprinted with cyclotron resonant scattering features (CRSFs) in a thin outer layer using the code by Schwarm et al. (2017a,b). Finally, general relativistic effects such as light bending and gravitational redshift are taken into account to calculate the observed phase and energy dependent flux from this column. Based on this model I discuss implications for the observable quantities and the shape of pulse profiles and cyclotron lines. I show that the geometrical setup, the observer inclination and the location of the accretion columns with respect to the rotational axis, has a significant effect on those observables and that general relativistic light bending plays an important role.

Further, I combine the ray tracing code presented in this work with a simple phenomenological emission profile to model the pulse profiles of the HMXB 4U 1626−67 and their energy evolution. In another source,the HMXB GX 301−2, I explain the origin and the phase dependence of the two observed cyclotron lines with a simple model. This model features a single column with two emission regions of different height. The observed variation with phase is caused by the dependency of the relativistic boosting due to the bulk motion of the downfalling plasma on the viewing angle and therefore pulse phase.

Contents

Chapter 1

Introduction to X-ray pulsars

In astrophysics we deal with phenomena and objects which exceed the physical boundaries we perceive on Earth and we are not able to replicate in laboratories. Observing the sky and its celestial objects and phenomena allows us to overcome these limitations and study the principles of nature at the boundaries of their validity. In this way we are able to expand our knowledge about the universe and its laws.

1.1 Neutron stars

The theoretical concept of neutron stars was introduced by Baade & Zwicky (1934), just shortly after the discovery of the neutron by Chadwick (1932). However, there is some debate whether Landau (1932) came up even before that[1] with the idea of neutron stars in his description of weird stars forming one gigantic nucleus. Nevertheless, Baade & Zwicky (1934) correctly suggested a neutron star to be the remnant of a supernova explosion, the dramatic death of a massive star which has utilized its fusion fuel. With nothing left to counter its own gravity the progenitor starts to collapse. As gravity overcomes even the Fermi pressure of degenerated electrons, these electrons are captured by their atom core transforming protons into neutrons and eventually leaving a star build up of neutrons. The binding energy released during this process of simultaneous bulk annihilation of mass via inverse β-decay powers the supernova explosion and exceeds the energy our sun produces during its whole lifetime (Zwicky, 1939).

Since they were first proposed, neutron stars have been of great theoretical interest not only because of their exotic interior, but also their place in stellar evolution. Despite the enormous energy release during their birth, neutron stars themselves were believed to be too faint to be directly detectable. Very little was actually known about possible emission properties of neutron stars at that time. In 1938 Baade (1938) already proposed the Crab Nebula to be a supernova remnant containing a neutron star, instead of being a common nova or planetary nebula. Nevertheless, it took until 1967 for the first compelling evidence for the existence of that neutron star. This evidence was provided by Hewish et al. (1968) with the discovery of

[1] See Yakovlev et al. (2013) for a detailed discussion of this debate.

precisely repeating radio pulsations observed in the direction of the Crab Nebula, a source they already described as unusual before (Hewish & Okoye, 1965). It was then quickly established that these radio pulsations are powered by a highly magnetized and rapidly spinning neutron star loosing its rotational kinetic energy (Pacini, 1967, Gold, 1968). Due to the conservation of angular momentum and magnetic flux of the progenitor star during the supernova collapse, neutron stars can reach spin periods in the sub-second regime and magnetic field strengths 10^{10} times greater than that of their progenitor (Woltjer, 1964). The pulsed nature of the emission was ascribed to the fact that the magnetic field axis is inclined with respect to the rotational axis of the neutron star.

Today we know that neutron stars are among the most compact objects, with typical masses of $\sim 1.4\,M_\odot$ and radii of $\sim 10\,\mathrm{km}$ (see, e.g., Lattimer, 2012, Steiner et al., 2013, and references therein). The equation of state (EOS) of neutron stars still puzzles physicists. The EOS determines the internal structure of neutron stars and allows to calculate possible mass-ratio relations. As shown in the left panel of Fig. 1.1, there are many different possibilities for the structure of neutron stars, which include hadronic as well as strange quark matter models. There are some general constraints on this relation. General relativity, for instance, requires a radius that exceeds the Schwarzschild radius in order for the surface to be visible. The Schwarzschild radius is given by

$$R_\mathrm{s} = 2GM_\mathrm{NS}/c^2 \approx (4.2\,\mathrm{km})\left(\frac{M_\mathrm{NS}}{1.4\,M_\odot}\right) \quad , \tag{1.1}$$

where G is the gravitational constant, c is the speed of light, and M_NS is the gravitating mass, i.e., the mass of the neutron star, and $M_\odot$ the mass of the sun. The escape velocity for objects smaller than their Schwarzschild radius exceeds the speed of light. These objects are black holes, whose surface is defined by their event horizon at R_s. Finite pressure and causality set an even lower upper limit to the compactness R_s/R of neutron stars, where the radius must be $\gtrsim 1.4R_\mathrm{s}$ (Lattimer, 2012). On the other hand, a lower boundary for the compactness of a neutron star is given by their rotational period. Below a certain limit they are believed to be shredded apart. Figure 1.1 shows this threshold for the fastest rotating pulsar PSR J1748−2446J (Hessels et al., 2006), which is spinning with a frequency of 716 Hz.

Besides their extreme compactness neutron stars can have strong, approximately dipole-like magnetic fields. Observed B-field strengths show a wide range, from relatively moderate (10^7 G) to extremely strong magnetic fields reaching up to 10^{15} G (Haensel et al., 2007). There are no other objects known which would even come close to reaching such strong B-fields, e.g., the Earth's B-field is on the order of 10^{-1} G (see, e.g., Karttunen et al., 2003) and the strongest persistent artificial field created in a laboratory[2] is on the order of 10^4 G.

Since the discovery of the Crab pulsar, hundreds of radio pulsars were discovered in our galaxy, as well as a variety of other kinds of pulsating neutron stars in different wave bands (Manchester et al., 2005). Pulsars are classified according to their primary source of power, which is either connected to their high compactness, their strong magnetic fields, or their rotational energy (Harding, 2013). As shown in the right panel of Fig. 1.1 the different types of neutron stars generally occupy different areas in the pulse period and B-field strength space. Magnetars exhibit the strongest magnetic fields observed in the universe, from which they

[2] As found at https://nationalmaglab.org/about/facts-figures/world-records on January 4th, 2018.

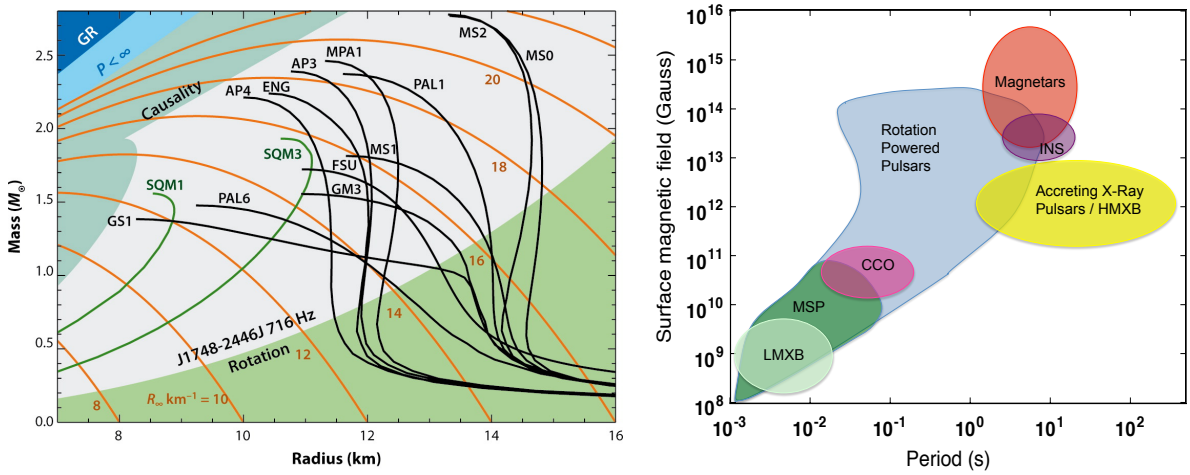

Figure 1.1.: Properties and types of neutron stars. **Left:** Theoretical mass-radius relation of a neutron star predicted for hadronic equations of state (black lines) and strange quark matter (green lines). The blue shaded regions are excluded by general relativity (GR), finite pressure ($P < \infty$), and causality. The green region is the limit derived by the highest-known rotation frequency of PSR J1748−2446J. Figure taken from Lattimer (2012). **Right:** Sketch of neutron star types categorized by there B-field strength and rotational period after Harding (2013).

gain their energy. Millisecond pulsars (MSPs), on the other hand, belong to the group of rotation-powered pulsars and, while having moderate B-field strengths, typically rotate very rapidly. Accreting X-ray pulsars are found in binary systems, in which the neutron star accretes matter from an optical companion star. Depending on the mass of the companion this class of accreting neutron stars can be divided into further subclasses. In so-called low mass X-ray binaries (LMXBs) the companion has a mass of $\lesssim 2\,M_\odot$, while in high mass X-ray binaries (HMXBs) the companion's mass is $\gtrsim 8\,M_\odot$ (Mészáros, 1992), like for example, O- or B-type stars. In the latter case the neutron stars exhibit strong B-fields and show rather long pulse periods, roughly between 1 and 1000 seconds. HMXBs are typically quite young systems in contrast to LMXBs, whose B-fields have already decayed (Bhattacharya & van den Heuvel, 1991, Zhang & Kojima, 2006) and the angular momentum transfer from the matter they have accreted spun them up to sub-second pulse periods. There are different mechanisms for the accretion in these X-ray binaries (see, e.g., Wilms, 2014, and references therein). In LMXBs, for example, disk accretion driven by Roche-Lobe overflow of the optical companion takes place. In many cases of HMXBs, on the other side, the strong stellar wind of the donor star feeds the accretion.

1.2 Highly magnetized accreting X-ray pulsars

Highly magnetized accreting X-ray pulsars are generally found in HMXB systems (Caballero & Wilms, 2012). Due to their strong magnetic field the accretion process is governed by the magnetosphere of the neutron star closer than a certain distance, independent of the primary accretion mechanism. Once the accreted matter passes the radius of equilibrium between its

own ram pressure pushing inwards and the outwards directed magnetic pressure, it is forced to follow the magnetic field lines onto the poles of the neutron star. The radius of equilibrium is called the Alfvén radius and is given by (Davidson, 1973, Elsner & Lamb, 1977)

$$\begin{aligned} r_{\mathrm{mag}} &= \left(\frac{1}{16G}\frac{R_{\mathrm{NS}}^{12}B_0^4}{M_{\mathrm{NS}}\dot{M}^2}\right)^{1/7} \\ &\approx \left(2.3\times10^8\,\mathrm{cm}\right)\left(\frac{M_{\mathrm{NS}}}{1.4\,M_\odot}\right)^{-1/7}\left(\frac{R_{\mathrm{NS}}}{10\,\mathrm{km}}\right)^{12/7}\left(\frac{B_0}{10^{12}\,\mathrm{G}}\right)^{4/7}\left(\frac{\dot{M}}{10^{17}\,\mathrm{g\,s^{-1}}}\right)^{-2/7} \end{aligned} \quad , \tag{1.2}$$

where R_{NS} is the radius of the neutron star, B_0 is the surface B-field strength at the pole of the neutron star, M_{NS} the mass of the neutron star, and $\dot{M}$ the mass accretion rate. In HMXBs with typical B-field strengths of $B_0 \sim 10^{12}$ G and mass accretion rates of $\dot{M} \sim 10^{17}\,\mathrm{g\,s^{-1}}$, the Alfvén radius is roughly 2400 km. At the Alfvén radius the magnetic torque couples the rotation of the material to that of the neutron star. In the case the rotational velocity at r_{mag} exceeds the orbital velocity, accretion is prevented by the so-called propeller effect, where the accreted matter cannot overcome the centrifugal force imposed by the co-rotating magnetosphere. This co-rotation radius is given by (Davidson, 1973)

$$r_{\mathrm{co}} = \left(\frac{GM_{\mathrm{NS}}P^2}{4\pi^2}\right)^{1/3} \approx \left(1.7\times10^8\,\mathrm{cm}\right)\left(\frac{M_{\mathrm{NS}}}{1.4\,M_\odot}\right)^{1/3}\left(\frac{P}{1\,\mathrm{s}}\right)^{2/3} \quad , \tag{1.3}$$

where P is the rotation period of the neutron star. The co-rotation radius is on the same order as the Alfvén radius, especially for short rotation periods.

Following the B-field lines, the infalling material is channeled onto the magnetic poles, where localized emission regions are formed as the accreted material is stopped at or close to the neutron star's surface. Assuming a dipolar B-field and following the critical field lines from the Alfvén radius to the poles, the polar radius of each funnel can be approximated with (Davidson, 1973)

$$r_{\mathrm{pole}} = \left(\frac{R_{\mathrm{NS}}^3}{r_{\mathrm{mag}}}\right)^{1/2} \approx (0.78\,\mathrm{km})\left(\frac{R_{\mathrm{NS}}}{10\,\mathrm{km}}\right)^{3/2}\left(\frac{M_{\mathrm{NS}}}{1.4\,M_\odot}\right)^{-1/6}\left(\frac{P}{1\,\mathrm{s}}\right)^{-1/3} \quad , \tag{1.4}$$

where in the second equality $r_{\mathrm{mag}} = r_{\mathrm{co}}$ is assumed.

1.2.1 X-ray emission

Within the accretion columns the kinetic energy released during the deceleration of the infalling plasma is transformed into radiation. Close to the neutron star the free fall velocity of the matter can reach up to 60% of the speed of light. An estimation for the luminosity of the accretion columns corresponding to the released kinetic energy assuming 100% efficiency is given by (Caballero & Wilms, 2012)

$$L^\star = \frac{G\dot{M}M_{\mathrm{NS}}}{R_{\mathrm{NS}}} \approx \left(1.86\times10^{37}\,\mathrm{erg\,s^{-1}}\right)\left(\frac{\dot{M}}{10^{17}\,\mathrm{g\,s^{-1}}}\right)\left(\frac{M_{\mathrm{NS}}}{1.4\,M_\odot}\right)\left(\frac{R_{\mathrm{NS}}}{10\,\mathrm{km}}\right)^{-1} \quad , \tag{1.5}$$

where * denotes the reference frame of the accretion column (see Sect. 2.1.4). The spectral shape of the escaping continuum radiation is characterized by reprocessing of seed photons

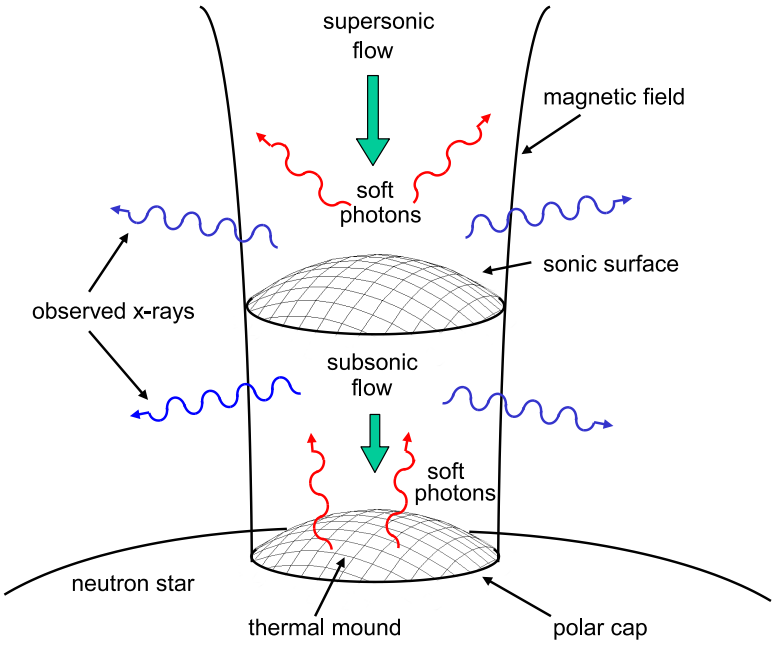

Figure 1.2.: Sketch of the formation of X-ray emission in accretion columns (Becker & Wolff, 2007). At the bottom of the column soft photons (red) are produced via black-body radiation, Bremsstrahlung and cyclotron emission. The infalling supersonic flow Compton upscatters these photons to higher energies. The plasma is decelerated to subsonic velocities at the radiative shock.

(e.g., black-body emission from the thermal mound or Bremsstrahlung) in the optically thick plasma, mainly through inverse Compton scattering ("Comptonization"). The detailed calculation of the spectral shape of the emerging continuum requires the solution of the radiative transfer equation (RTE). Different methods and techniques for solving the RTE under various assumptions have been presented, e.g., by Becker & Wolff (2005a,b, 2007), Postnov et al. (2015), Farinelli et al. (2016), and Wolff et al. (2016). The common prediction of these various calculations is that the broad-band spectrum is roughly powerlaw-like and often shows a high-energy cutoff. These models are in agreement with observations and therefore allow us to connect the continuum shape with physical properties of the column, like, e.g., the electron temperature or velocity structure.

In Fig. 1.2 the generally accepted picture of the X-ray formation process after Becker & Wolff (2007) is shown. The kinetic energy of the infalling plasma is transformed into radiation mainly through three different mechanisms. 1) At the bottom of the accretion column on the polar caps the material hitting the neutron star's surface creates a thermal mound, which produces black-body emission. 2) Throughout the column also Bremsstrahlung photons are generated by the deflection of electrons in the infalling thermal plasma. Both of these processes produce emission with a certain energy distribution, while 3) cyclotron emission additionally occurring inside the whole column is monochromatic for a certain B-field strength. This

emission is caused by the radiative de-excitation of electrons after collisional excitation with protons (see also Sect. 1.2.2).

The presence of a strong magnetic field causes photons to propagate through the medium in the form of two polarization modes due to collective plasma effects and electron-positron vacuum polarization (Mészáros & Ventura, 1978, Pavlov et al., 1980). These modes are usually called ordinary and extraordinary modes and behave differently in the scattering process. During the diffusion of these seed photons through the column they undergo bulk Comptonization, which is the inverse Compton scattering off relativistic electrons. While these photons gain energy, they decelerate the infalling plasma to subsonic velocities and cause the formation of a radiation-dominated shock (Davidson, 1973). The shock builds up once the X-ray luminosity in the column is larger than the so-called critical luminosity (Basko & Sunyaev, 1976, Becker, 1998, Mushtukov et al., 2015),

$$L^{\star}_{\rm crit} = \left(3.8 \times 10^{38}\,{\rm erg\,s^{-1}}\right) \frac{\sigma_{\rm T}}{\sqrt{\sigma_{\parallel}\sigma_{\perp}}} \left(\frac{M_{\rm NS}}{1.4\,M_{\odot}}\right) \frac{r_{\rm AC}}{R_{\rm NS}} \quad , \tag{1.6}$$

with $r_{\rm AC}$ the radius of the accretion column, $\sigma_{\rm T}$ the Thomson scattering cross section, and the scattering cross sections $\sigma_{\parallel}$ and $\sigma_{\perp}$, parallel and perpendicular to the magnetic field, respectively. In the case of pure Thomson scattering both components would equal the Thomson scattering cross section, i.e., $\sigma_{\parallel} = \sigma_{\perp} = \sigma_{\rm T}$. The process of bulk Comptonization results in the emitted spectrum having a power-law like shape. Additionally, thermal Comptonization causes an energy transfer from high to low energy photons and is, thus, the reason for the high-energy roll-over observed in the spectra.

1.2.2 Cyclotron resonant scattering features

Accreting X-ray pulsars also show spectral features in the hard X-rays, between about 1 and 100 keV, which are associated with their extreme B-fields. While the electron momentum parallel to the B-field is continuous and can be interpreted as the temperature of the plasma, the electron momentum perpendicular to the field is quantized into Landau levels in the presence of a strong B-field roughly on the order of the quantum-electrodynamical critical field strength (e.g., Canuto et al., 1971, Schwarm et al., 2017b),

$$B_{\rm crit} \approx \frac{m_{\rm e}^2 c^3}{e\hbar} = 44.14 \times 10^{12}\,{\rm G} \quad , \tag{1.7}$$

where $m_{\rm e}$ is the mass of the electron, e its charge, and $\hbar$ is the Planck constant divided by 2π. The energy of these Landau levels in the rest frame of the electron is given by

$$E'_{{\rm CRSF}n} = \frac{m_{\rm e}c^2}{\sin^2\eta_{\rm in}} \left(\sqrt{1 + 2n\frac{B}{B_{\rm crit}}\sin^2\eta_{\rm in}} - 1 \right) \quad , \tag{1.8}$$

where $n \in \mathbb{N}$ is the quantum number of the Landau level with $n = 1$ corresponding to the fundamental line and $\eta'_{\rm in}$ is the incident angle of the scattering photon with respect to the magnetic field (see, e.g., Mészáros, 1992). The prime ($'$) denotes the co-moving reference frame of infalling and emitting Plasma (see Sect. 2.1.4). For $B \ll B_{\rm crit}$ the Landau levels in Eq. 1.8 are approximately equidistant with energies

$$E'_{{\rm CRSF}n} = n \times \frac{m_{\rm e}c^2 B}{B_{\rm crit}} \approx n \times 11.6\,{\rm keV} \left(\frac{B}{10^{12}\,{\rm G}}\right) \quad , \tag{1.9}$$

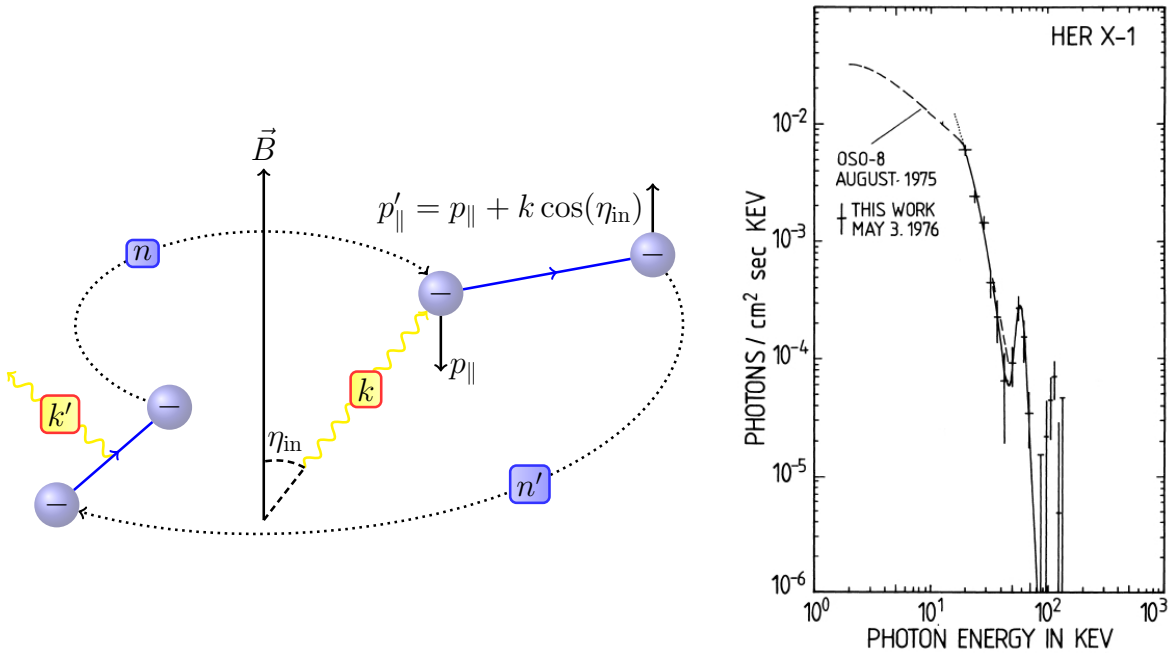

Figure 1.3.: **Left:** Sketch of a Landau level transition (F.-W. Schwarm, priv. comm.). A photon k incoming with an angle $\eta_{\rm in}$ to the B-field excites an electron with the momentum $p_\parallel$ parallel to the B-field from the Landau level n to n'. During the decay of the electron back to the level n a photon k' is emitted. **Right:** Discovery of the first CRSF observed in the spectrum of Her X-1 by Trümper et al. (1978).

which is the so called 12-B-12 rule. As a result of this quantization, the cross section for photons scattering off these electrons is increased by several orders of magnitude at the resonant energies corresponding to the energy differences between the Landau levels. An incoming photon of sufficient energy can excite an electron into a higher Landau level (Fig. 1.3, left panel). It is in principle possible to excite any Landau level as long as the photon meets the required energy, although the scattering cross section decreases rapidly with increasing n (see, e.g., Schwarm et al., 2017b). The excited electron state has only a lifetime on the oder of 10^{-15} s, which is shorter than the typical time for collisional de-excitation in the plasma of the accretion column. Therefore the de-excitation predominantly takes place via photon spawning to the next lower Landau level.

For the tenuous magnetized plasma in the accretion column, Compton scattering off these quantized electrons dominates over absorption (Bonazzola et al., 1979) and cyclotron resonant scattering features (CRSFs), or cyclotron lines, are formed. These CRSFs typically appear as broad absorption features in the observed spectra and allow us to directly measure the strength of the B-field at the location they are formed. The first observational evidence for such a CRSF was reported by Trümper et al. (1978) in the spectrum of Her X-1 (Fig. 1.3, right panel). Today we know about 35 objects with reasonable secured CRSFs and some additional candidates (Staubert et al., 2018).

Figure 1.4 shows example spectra for two accreting X-ray pulsars, namely Her X-1 and Cen X-3. The observed X-ray spectra of both sources show the typical power-law like shape with a roll-over towards high energies. After the model by Becker & Wolff (2007) the

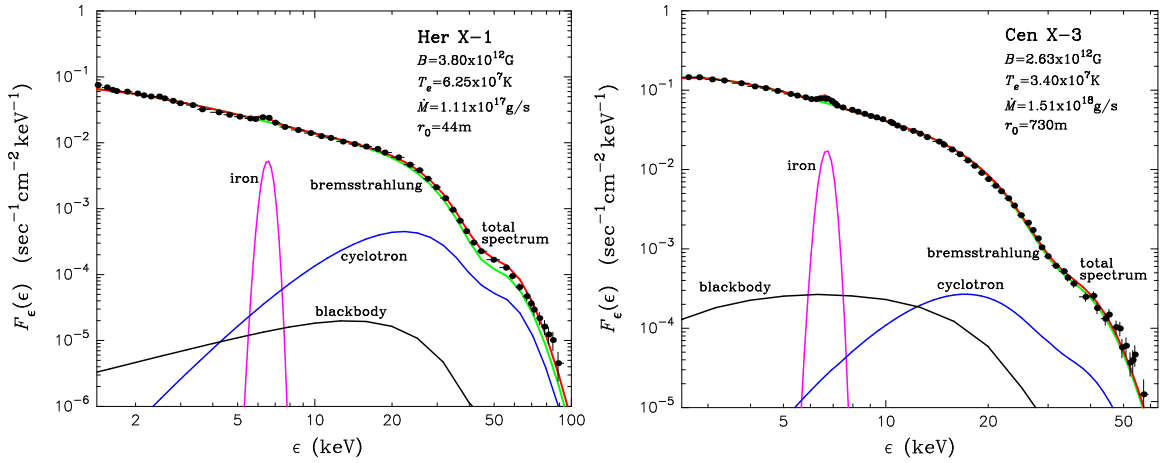

Figure 1.4.: Observed example X-ray spectra for Her X-1 and Cen X-3 (black points) described with the physical model by Becker & Wolff (2007) (red lines) and its individual components, i.e., Bremsstrahlung (green), cyclotron emission (blue) and black-body (black), and an additional iron line (magenta).

continuum is mainly shaped by the Comptonization of Bremsstrahlung, while cyclotron and black-body emission only contribute marginally to the seed photons processed within the column. A cyclotron line noticeable as broad absorption feature is also present in both sources. The additional iron emission line does not originate from the accretion column itself, but is due to fluorescence in the accretion disk surrounding the neutron star.

CRSFs are typically observed to vary with rotational period of the neutron star in energy, depth, and width due the varying viewing angle with respect to the *B*-field. The observed variations are a consequence of the strong angular dependency of the cyclotron cross section, combined with special relativistic effects such as strong beaming, as typical speeds in the accretion column can reach 60% of the speed of light. In several sources the observed CRSF energy also varies with source luminosity (e.g., Staubert et al., 2007, Tsygankov et al., 2010, Becker et al., 2012, Poutanen et al., 2013, Fürst et al., 2014b, 2015, Lutovinov et al., 2015, and references therein). These variations are typically attributed to changes in the internal structure of the accretion column or to the interaction of the column's emission with the surface of the neutron star or the accretion disk. For example, Becker et al. (2012) showed that depending on the mass accretion rate, different processes dominate the braking of matter in the accretion column. Depending on the process that dominates, the emission height and therefore also the CRSF energy reacts differently to changes in mass accretion rate and, thus, luminosity. At low luminosities, magnetohydrodynamic effects stop the material (Fig. 1.5a). An increase in the mass accretion and therefore in luminosity causes a gas shock to evolve, whose height increases with luminosity, moving the emission height further up where the smaller *B*-field results in lower CRSF energies (b). The gas shock rises until Coulomb interactions form a radiative shock, which now is responsible for stopping the material and bulk Comptonization takes place (Becker & Wolff, 2007). In this regime (c), increasing mass accretion rate compresses the column, so an increase in luminosity will be accompanied by an increase in CRSF energy (Staubert et al., 2007, Becker et al., 2012, Rothschild et al., 2017). Above a critical luminosity (Eq. 1.6), however, the radiation pressure dominates the dynamics of the plasma. In this regime,

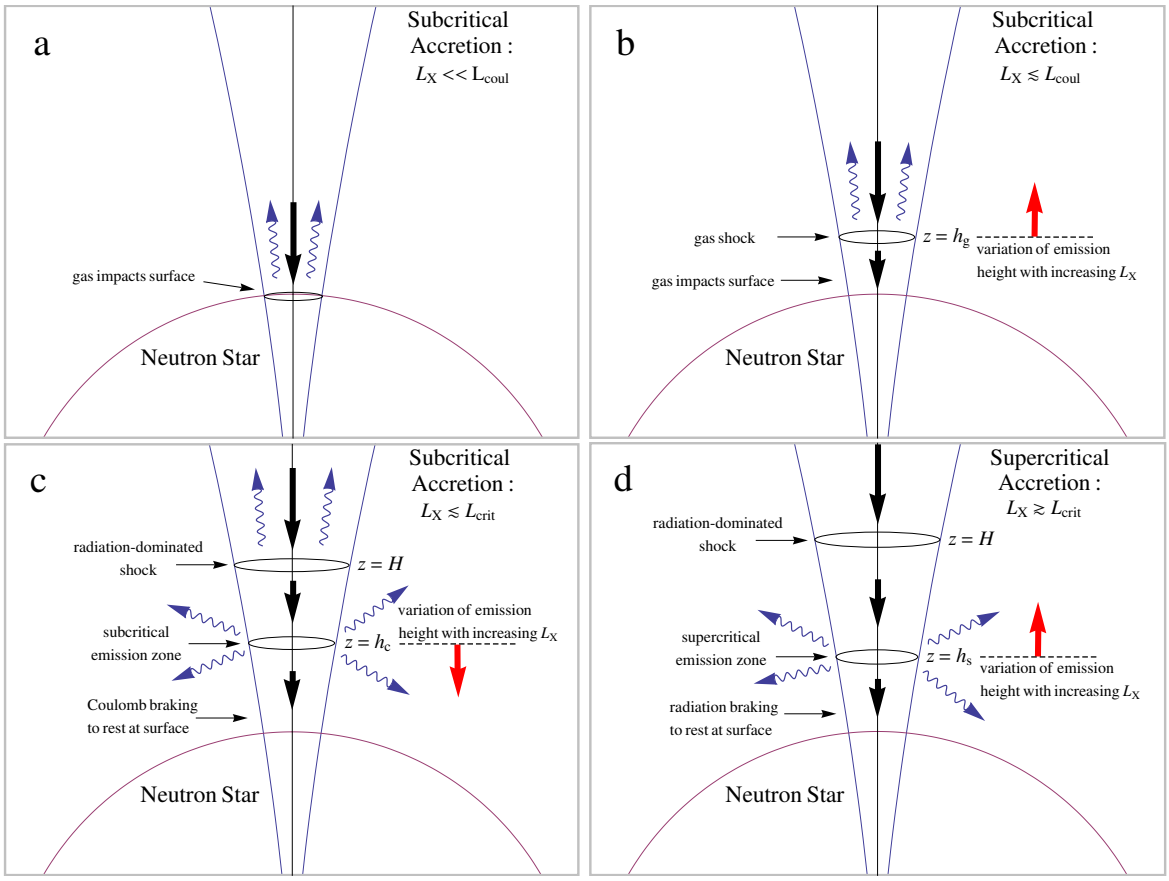

Figure 1.5.: Different theoretical accretion regimes within the accretion column determining the emission height as function of luminosity (Becker et al., 2012). **a**: At very low luminosities the infalling plasma is stopped at the surface of the neutron star. **b**: For increasing luminosity the emission height rises due to a evolving gas shock. **c**: Close to a critical luminosity a radiation dominated shock forms causing the emission height to decrease again. **d**: Above the critical luminosity the emission height rises again.

as the mass accretion rate and, thus, the luminosity increases, the shock moves upwards into regions of smaller *B*-field strengths such that we expect the CRSF energy to decrease again (d).

Poutanen et al. (2013) oppose this picture of the growth of the accretion column with luminosity being the origin of the observed emission and CRSFs. They argue that the related gradient of the *B*-field in this scenario is too large to allow us to observe CRSFs as line-like absorption features. As the energy of the cyclotron line is dominated by the *B*-field (Eq. 1.8) a large range of *B*-fields in the line forming region would lead to a superposition of many lines, which would completely smear them out in the observed spectra. Moreover, the observed variations of the CRSF energies is much smaller than would be expected from the corresponding changes in luminosity. Based on these concerns Poutanen et al. (2013) suggest that it is physically more realistic that CRSFs are formed when the radiation of the column is reflected off the neutron star's surface as there the gradient in the *B*-field is much smaller

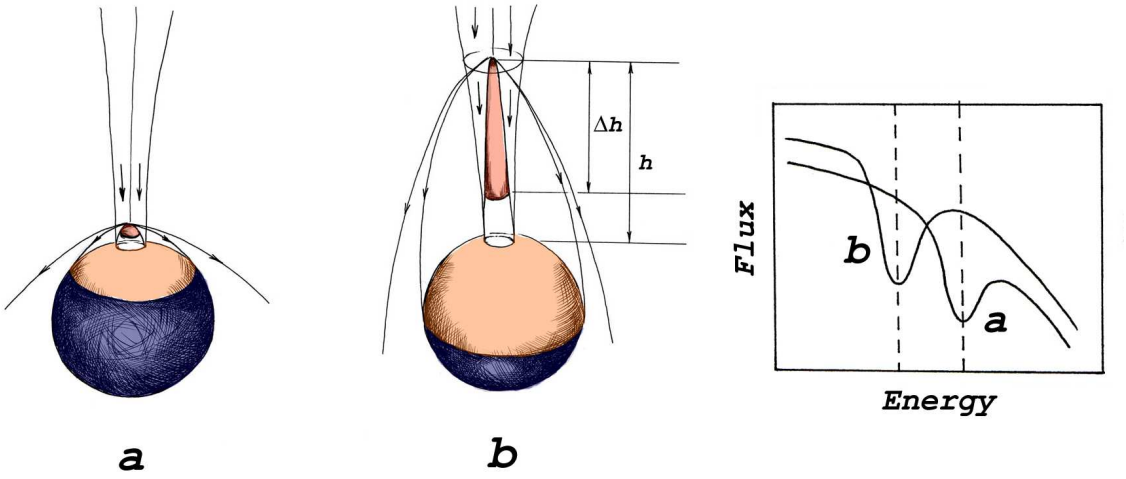

Figure 1.6.: Reflection model suggested by Poutanen et al. (2013), where CRSFs are formed on the neutron star's surface. For illustration purposes only one accretion column is shown. **a**: The low emission height of the column only illuminates a small radius around the column on the neutron star's surface, where the *B*-field is still strong. **b**: For higher emission heights this illumination radius also increases causing reflection from areas with lower *B*-fields, which results in a decrease of the observed CRSF energy.

than in the column. Additionally, due to general relativistic light bending and the relativistic downwards boosting caused by the bulk velocity of the infalling plasma a large fraction of the accretion column emission is focused towards the neutron star and hitting its surface (see Chapters 2 and 3). In their model low luminosities correspond to small accretion columns, which illuminate only a small area around the pole of the neutron star (Fig. 1.6a). Close to the column, the *B*-field is still strong and the resulting CRSFs are observed at high energies correspondingly. As the luminosity increases so does the height of the accretion column, whose emission now can illuminate a larger fraction of the surface, where lower *B*-fields result in a decrease of the observed CRSF energies (b).

Both of these scenarios might explain the observed variation of the observed CRSF energy with luminosity, but both act on assumptions and leave open questions. The accretion column model by Becker et al. (2012), for instance, is one-dimensional, neglecting the radial extension of the column in order to be able to solve their complex radiative transfer equation. In the reflection model, Poutanen et al. (2013) assume that the cyclotron lines formed by reflection have the same spectral shape as via transmission. Schwarm et al. (2017a,b), however, show that the geometry of emission regions and the origin of the seed photons influences the CRSFs. Furthermore, a large and extended emission region is problematic in terms of the observed high variations of the flux with rotational period.

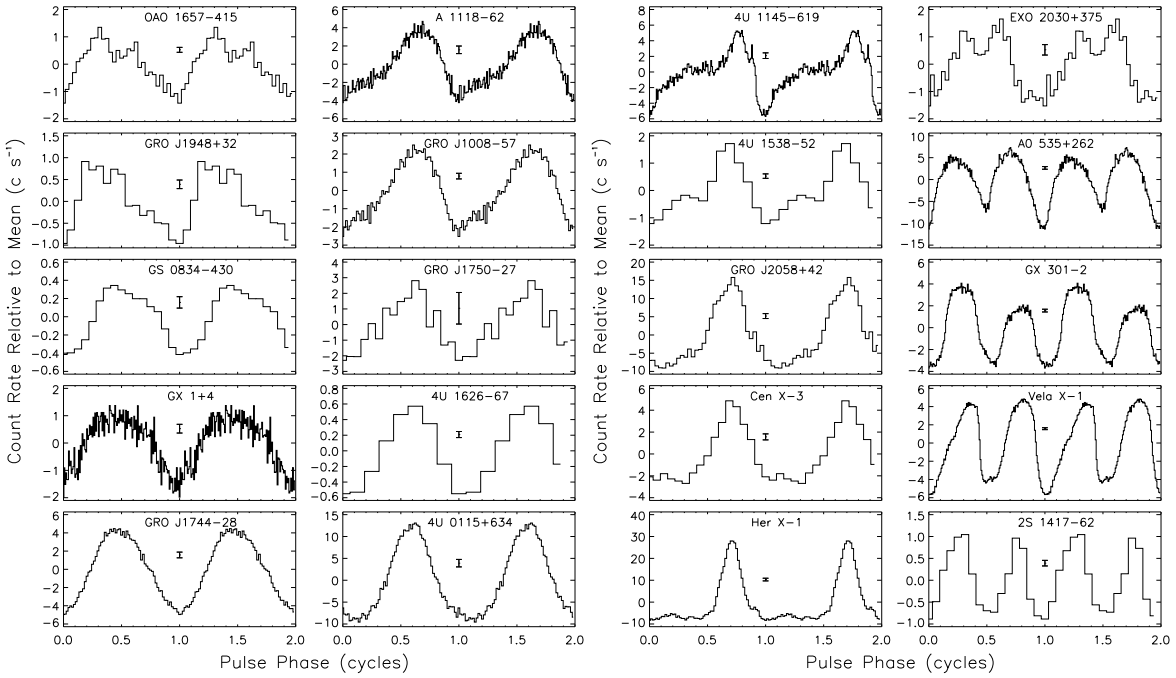

Figure 1.7.: Example pulse profiles of several accreting X-ray pulsars (taken from Bildsten et al., 1997). Note that the pulse profiles are shown for two pulse phase cycles.

1.3 Pulse profiles

In the previous section I focused on the spectral formation of the X-ray emission originating from the accretion columns. These considerations, however, do not include the geometrical effects introduced by the rotation of the neutron star. The magnetic axis and the spin axis of the neutron star are often misaligned (Parmar et al., 1989). As the neutron star rotates through our line of sight, this results in periodic changes of the observed flux (Lamb et al., 1973). While X-ray pulsars all share a similar spectral distribution, such pulse profiles exhibit various shapes as shown in Fig. 1.7. Their shapes include single peaks as well as double peaks, which range from broad to narrow and can be symmetric or highly asymmetric. But also more complex shapes have been observed.

Pulse profiles of X-ray pulsars are unique for individual source states, but often show a strong energy and luminosity dependence. The morphology of the profiles depends on the system's intrinsic geometry and the intrinsic emission profiles, which in turn depend on the mass accretion rate and therefore on the luminosity.

In order to interpret the observational data in the light of physical models, we need to be able to compare the model predictions, such as the energy and angle dependent model flux, with observations. General relativistic effects have to be taken into account due to the compactness of the neutron star and the strong influence of light bending on the relation between the intrinsic emission angle and the observed viewing angle. These angles would be identical in flat space-time with straight geodesics. In the close vicinity of the neutron star, however, the photon trajectories are deflected by up to 180° in the most extreme cases (see Chapter 2). Neglecting the effects of general relativity therefore would lead to a wrong relation between the intrinsic emission profile and the observed pulse profile. One can either

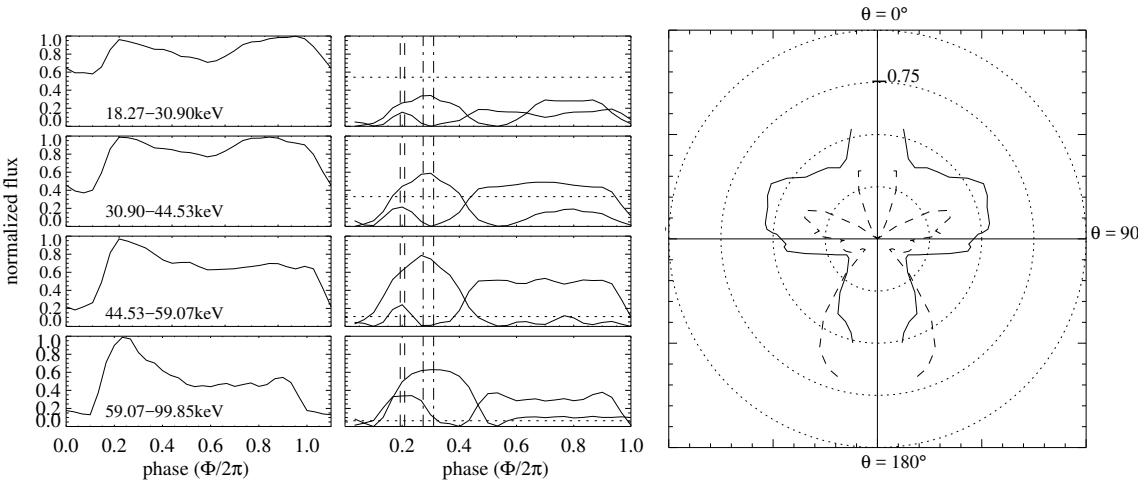

Figure 1.8.: Pulse profile decomposition of A 0535+26 (taken from Caballero et al., 2011). The original pulse profiles described with a Fourier series, normalized to unity in four different energy ranges and their decomposition in two symmetric functions are shown in the left and middle panel, respectively. The right panel shows the reconstructed beam pattern for the lowest (solid line) and highest (dashed line) energy range, where θ is the angle to the magnetic field.

start from the observed data and try to infer what the accretion column's emission looks like, or model the column emission and predict what the observer might see. An example for the former approach is the work of Kraus et al. (1995), who used a Fourier decomposition method to disentangle the observed pulse profiles into individual contributions of the intrinsic beam patterns of the poles. Figure 1.8 shows the application of this method to A 0535+26 (Caballero et al., 2011). First the pulse profile, in this case the four pulse profiles in different energy bands, are described with a Fourier series. Then possible decompositions of this Fourier series into two contributions are determined with the restriction that each is a symmetric function. This approach is based on the assumption that the observed flux originates mainly from the two emission regions at the poles of the neutron star and that their emission profile is axis-symmetric with respect to the *B*-field. These solutions, however, are not unique.

Although this decomposition was successful in providing possible beam patterns and geometries for several sources (e.g., Kraus et al., 1996, Blum & Kraus, 2000, Sasaki et al., 2010, 2012), it does not allow us to obtain any information about the underlying physical processes leading to the obtained beam patterns. In other words it does not allow us to use emission profiles based on physical models to describe the observed pulse profiles. Alternatively, a forward methodology was used to calculate the observable flux by applying emission profiles to a given geometry of the emission region (e.g., Beloborodov, 2002, Poutanen & Beloborodov, 2006, Ferrigno et al., 2011, and references therein). To solve the emerging general relativistic equations in a (semi-)analytical manner, all of these authors rely on symmetries of the emission region with respect to the center of mass, such as hot spots on a sphere with fixed radius (Beloborodov, 2002, Poutanen & Beloborodov, 2006) or conical accretion columns (Ferrigno et al., 2011).

1.3.1 Phenomenological models

The physical models describing the continuum and the cyclotron resonant scattering features seen in accreting X-ray pulsars are relatively new and still under development. In the majority of publications analyzing observed spectra of these objects phenomenological models are still used.

The basic shape common to all observed X-ray continua is roughly described by a power-law,

$$\texttt{PL}(E) \propto E^{-\Gamma} \quad , \tag{1.10}$$

where E is the observed energy and Γ is the photon index (Müller et al., 2013b, and references therein). This power-law like shape is expected from the bulk Comptonization, i.e., upscattering of photons via inverse Compton off relativistic electrons, within the accretion column (see Sect. 1.2.1) with expected photon indices of $0 < \Gamma \leq 2$ (Becker & Wolff, 2007).

In addition to the overall power-law shape, many continua feature an exponential roll-over at energies typically between 6 and 30 keV (see Fig. 1.9). There are different models, which are commonly used to describe this roll-over. The simplest one is the cut-off power-law,

$$\texttt{CutoffPL}(E) = \texttt{PL}(E) \times \exp(-E/E_{\text{fold}}) \quad , \tag{1.11}$$

where E_{fold} is the folding energy above which the decreasing influence of the roll-over dominates the continuum. The folding energy is often interpreted as the electron temperature as Becker & Wolff (2007) included thermal Comptonization to explain the observed exponential roll-over. The Fermi-Dirac cutoff (Tanaka, 1986),

$$\texttt{FDcut}(E) = \texttt{PL}(E) \times \frac{1}{1 + \exp((E - E_{\text{cut}})/E_{\text{fold}})} \quad , \tag{1.12}$$

introduces an additional degree of freedom with the cut-off energy E_{cut} to model the exponential roll-over. Note that in some cases the folding energy in the `CutoffPL` is misleadingly named cut-off energy due to the name of the model.

A similar model is the multiplicative high energy cut-off model in combination with the `PL` model,

$$\texttt{HighEcut}(E) = \texttt{PL}(E) \times \begin{cases} 1 & \text{for} \quad E < E_{\text{cut}} \\ \exp(-(E - E_{\text{cut}})/E_{\text{fold}}) & \text{for} \quad E \geq E_{\text{cut}} \end{cases} \quad . \tag{1.13}$$

Note that the `CutoffPL` is a special case of this model for $E_{\text{cut}} = 0$ keV. In contrast to the `CutoffPL` and `FDcut`, which both are continuously differentiable, the `HighECut` has a break in its derivative at the cut-off energy. Burderi et al. (2000) therefore modified this model to smooth this break, i.e.,

$$\texttt{SHighEcut}(E) = \begin{cases} \texttt{PL}(E) & \text{for} \quad E \leq E_{\text{cut}} - \Delta E_{\text{S}} \\ c_3 E^3 + c_2 E^2 + c_1 E + c_0 & \text{for} \quad E_{\text{cut}} - \Delta E_{\text{S}} < E < E_{\text{cut}} + \Delta E_{\text{S}} \\ \texttt{PL}(E) \times \exp(-(E - E_{\text{cut}})/E_{\text{fold}}) & \text{for} \quad E \geq E_{\text{cut}} + \Delta E_{\text{S}} \end{cases} \quad , \tag{1.14}$$

where ΔE_{S} is the width of the smoothness and the constants c_0, c_1, c_2, and c_3 are calculated such that the function and its derivatives in $E_{\text{cut}} \pm \Delta E_{\text{S}}$ are continuous.

An alternative continuous model is the negative and positive power law with an exponential cut-off (Mihara, 1995),

$$\texttt{NPEX}(E) = (N_1 E^{-\Gamma_1} + N_2 E^{+\Gamma_2}) \exp(-E/kT) \quad , \tag{1.15}$$

where N_1 and N_2 are the normalizations of the negative and positive power law with photon indices Γ_1 and Γ_2, respectively. Note that both photon indices are defined to be positive, and that $\Gamma_2 = 2$ is assumed in many cases (Mihara, 1995). The `NPEX` model basically consists of two `CutoffPL` with the same folding energy, which is replaced by the temperature kT.

The cyclotron resonant scattering features (see Sect. 1.2.2), which are typically noticeable as broad absorption lines in the X-ray spectrum, are often modeled by a Gaussian,

$$\texttt{gabs}(E) = \exp\left(-\frac{d_{\mathrm{CRSF}}}{\sqrt{2\pi}\sigma_{\mathrm{CRSF}}} \exp\left[-\frac{(E - E_{\mathrm{CRSF}})^2}{2\sigma^2_{\mathrm{CRSF}}}\right]\right) \quad , \tag{1.16}$$

where E_{CRSF} is the line energy of the CRSF, σ_{CRSF} its width, and d_{CRSF} its strength or also called depth. From the strength and width of the `gabs`-line its corresponding optical depth can be calculated by

$$\tau_{\mathrm{CRSF}} = \frac{d_{\mathrm{CRSF}}}{\sqrt{2\pi}\sigma_{\mathrm{CRSF}}} \quad . \tag{1.17}$$

Alternatively, a pseudo-Lorentzian absorption profile given by (Mihara et al., 1990, Makishima et al., 1990)

$$\texttt{cyclabs}(E) = \exp\left(-\tau_{\mathrm{CRSF}} \frac{(\sigma_{\mathrm{CRSF}} E/E_{\mathrm{CRSF}})^2}{(E - E_{\mathrm{CRSF}})^2 - \sigma^2_{\mathrm{CRSF}}}\right) \tag{1.18}$$

is also commonly used to model the CRSFs. The minimum of Eq. 1.18 is located at

$$E_{\mathrm{min}} = E_{\mathrm{CRSF}}\left(1 + \frac{\sigma^2_{\mathrm{CRSF}}}{E^2_{\mathrm{CRSF}}}\right) \tag{1.19}$$

in contrast to the `gabs` model, where it is found at E_{CRSF}. Consequently the cyclotron energy obtain with `cyclabs` is roughly 2–20% or respectively 1–4 keV lower than that obtain with `gabs` (Fig. 1.9).

In many accreting X-ray pulsars a soft excess around ~5 keV (e.g., Mihara, 1995) is observed, which requires an additional model component to fit the spectrum. Commonly this feature is modeled with a broad Gaussian in emission, an additional power-law as in the `NPEX` model, or with a black-body. The observed spectra also show features, which are not associated with the formation of the intrinsic emission from the accretion column itself. Between their formation and their detection, the X-ray spectra are modified by photoelectric absorption when passing through ionized or neutral material, which can be located in the close vicinity around the source, in the system of the binary, or within our Milky Way as part of the interstellar medium. This absorption is noticeable as a lack of photons in the soft X-ray regime below ~10 keV. A secondary effect of this absorption are fluorescent emission lines.

Figures 1.9 and 1.10 show an example overview of continuum and cyclotron line parameters for 23 galactic accreting X-ray pulsars based on the phenomenological models described above. The list of sources and the corresponding references are not complete as the purpose of

Figure 1.9.: Example overview of observed continuum and CRSF parameters in X-ray pulsars for illustration purposes. Shown are the flux derived X-ray luminosities, $L_{4\pi}$, the photon index, Γ, the folding energy $E_{\rm fold}$, the cut-off energy, $E_{\rm cut}$, and the CRSF energy, $E_{{\rm CRSF}n}$, width, $\sigma_{{\rm CRSF}n}$ and optical depth, $\tau_{{\rm CRSF}n}$ in the phase-averaged spectra as indicated by the overline. For each object, colors relate to the corresponding reference given as numbers below the object name on the y-axis (reference list see Fig. 1.10). For each object and reference the parameter range markers distinguish different empirical continuum models, that is `CutoffPL` (■), `HighEcut` (▲), `SHighEcut` (►), `FDcut` (▼) and `NPEX` (∗), and empirical line models `gabs` (•), `gabs+gabs` (●), `cyclabs` (♦) and `modified gauss` (×). Values obtained by physical models are marked with a ★. For details on the models see the corresponding reference. Gray boxes indicate the overall range. For multiple occurrences of a parameter, e.g., multiple CRSFs, each one is marked with an individual box with increasingly lighter gray shading for higher cyclotron line harmonics. Values were partially taken from figures, obtained from different instruments and different models and may be biased by systematic errors. Statistical errors are not included. Luminosities are only a rough representation as uncertainties in distance were not taken into account and are calculated for different energy ranges within 1 and 100 keV.

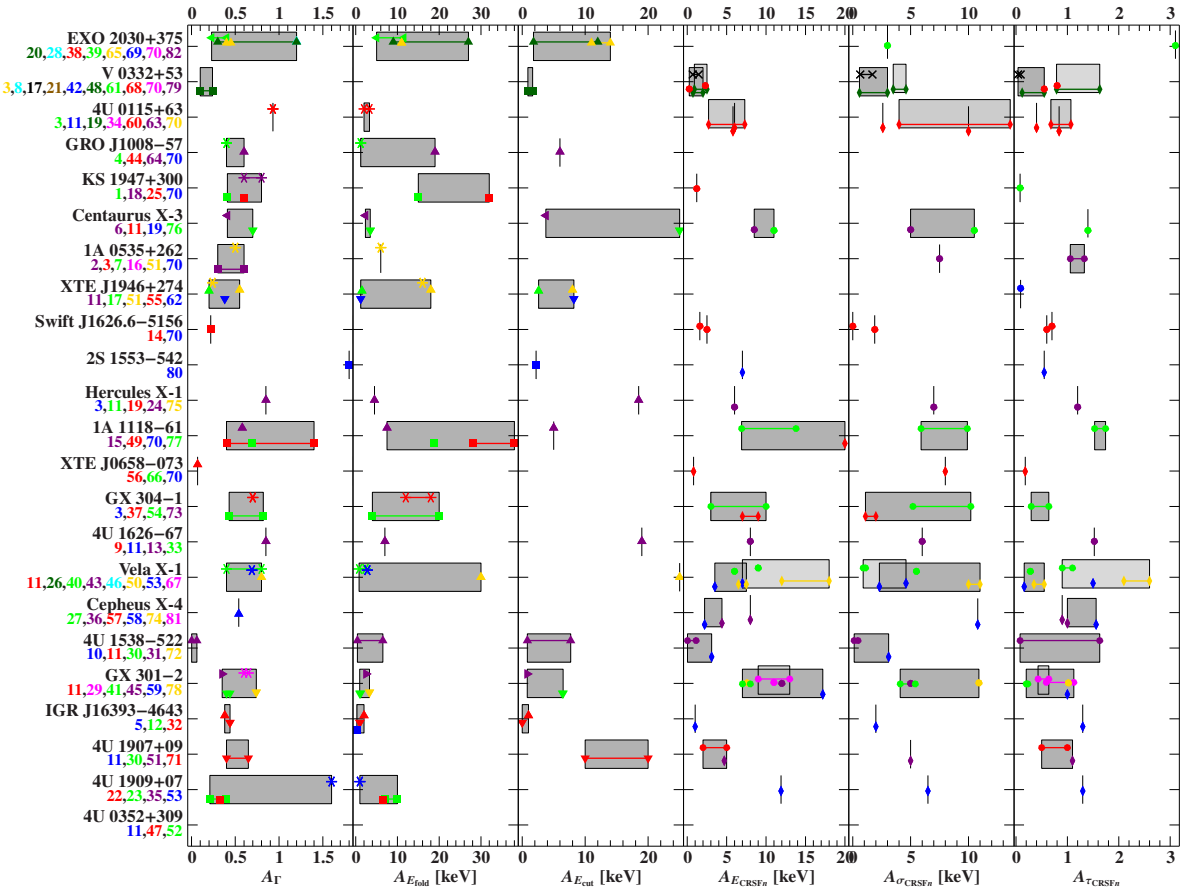

Figure 1.10.: Same as Fig. 1.9, but for phase-resolved analyses. Shown are the amplitudes occurring in the phase-resolved spectra for the photon index, A_Γ, the folding energy, $A_{E_{\rm fold}}$, the cut-off energy $A_{E_{\rm fold}}$, and the CRSF energy $A_{E_{{\rm CRSF}n}}$, width $A_{\sigma_{{\rm CRSF}n}}$ and the optical depth $A_{\tau_{{\rm CRSF}n}}$.
References. [1] Ballhausen et al. (2016); [2] Ballhausen et al. (2017); [3] Becker et al. (2012); [4] Bellm et al. (2014); [5] Bodaghee et al. (2016); [6] Burderi et al. (2000); [7] Caballero et al. (2013); [8] Caballero-García et al. (2016); [9] Camero-Arranz et al. (2012); [10] Clark et al. (1990); [11] Coburn et al. (2002); [12] D'Aì et al. (2011); [13] D'Aì et al. (2017); [14] DeCesar et al. (2013); [15] Devasia et al. (2011); [16] Müller et al. (2013a); [17] Doroshenko et al. (2017); [18] Epili et al. (2016); [19] Farinelli et al. (2016); [20] Ferrigno et al. (2016b); [21] Ferrigno et al. (2016a); [22] Fürst et al. (2011a); [23] Fürst et al. (2012); [24] Fürst et al. (2013); [25] Fürst et al. (2014a); [26] Fürst et al. (2014b); [27] Fürst et al. (2015); [28] Fürst et al. (2017); [29] Fürst et al. (2018); [30] Hemphill et al. (2013); [31] Hemphill et al. (2016); [32] Islam et al. (2015); [33] Iwakiri et al. (2018); [34] Iyer et al. (2015); [35] Jaisawal et al. (2013); [36] Jaisawal & Naik (2015); [37] Jaisawal et al. (2016); [38] Klochkov et al. (2007); [39] Klochkov et al. (2008); [40] Kreykenbohm et al. (2002); [41] Kreykenbohm et al. (2004); [42] Kreykenbohm et al. (2005); [43] Kreykenbohm et al. (2008); [44] Kühnel et al. (2017); [45] La Barbera et al. (2005); [46] La Parola et al. (2016); [47] Lutovinov et al. (2012); [48] Lutovinov et al. (2015); [49] Maitra et al. (2012); [50] Maitra & Paul (2013b); [51] Maitra & Paul (2013a); [52] Maitra et al. (2017); [53] Makishima et al. (1999); [54] Malacaria et al. (2015); [55] Marcu-Cheatham et al. (2015); [56] McBride et al. (2006); [57] McBride et al. (2007); [58] Mihara et al. (1991); [59] Mihara (1995); [60] Mihara et al. (2004); [61] Mowlavi et al. (2006); [62] Müller et al. (2012); [63] Müller et al. (2013b); [64] Naik et al. (2011); [65] Naik et al. (2013); [66] Nespoli et al. (2012); [67] Odaka et al. (2013); [68] Pottschmidt et al. (2005); [69] Reig & Coe (1999); [70] Reig & Nespoli (2013); [71] Rivers et al. (2010); [72] Rodes-Roca et al. (2009); [73] Rothschild et al. (2017); [74] Schwarm et al. (2017a); [75] Staubert et al. (2016); [76] Suchy et al. (2008); [77] Suchy et al. (2011); [78] Suchy et al. (2012); [79] Tsygankov et al. (2010); [80] Tsygankov et al. (2016); [81] Vybornov et al. (2017); [82] Wilson et al. (2008).

this figure is to convey a feeling for the parameter ranges and for comparison with the physical model presented in Chapter 3. These figures focus on parameters associated with the broad band continuum and the cyclotron line. Thus, they do not show additional components as required for a full description of the total observed spectrum, such as photoelectric absorption or a soft excess.

Figure 1.9 shows parameter ranges obtained from phase-averaged spectra. In particular, phase-averaged means that the spectra are averaged over the pulse period of the pulsar or are exceeded by their time resolution. These parameters do not only vary from source to source, but can also change within an individual source observed in different states. The main indicator for the source state is its luminosity as also shown in the figure. To distinguish between variations linked to changes of the source state and differences caused by the use of different models, the figure also indicates those models and the corresponding references. Note that the sources are sorted by their highest observed luminosity[3], nevertheless there is no obvious correlation recognizable. However, the degree of the parameter variation seems to be roughly correlated to the range of the luminosity the corresponding source was observed in.

Figure 1.10 shows results from phase-resolved spectral analyses. In particular, the amplitudes of the parameters during the pulse phase are shown. Phase-resolved analyses require a certain time-resolution of the data to resolve the pulse phase of the pulsar, while simultaneously maintaining a sufficient signal to noise ratio. Therefore, the amount of available data obtained from phase-resolved analyses is significantly less than for phase-averaged analyses. The observed spectral variabilities with respect to the pulse phase shown in Fig. 1.10 are in the order of the variations with luminosity (Fig. 1.9) or even stronger. This strong phase dependence shows the necessity of phase-resolved analyses as it allows us to interpret observations in a physically meaningful manner, while drawing conclusions from phase-averaged spectra should be taken with caution. This is especially important with regard to CRSFs because of their strong dependency on the viewing angle to the B-field. For instance, a CRSF could only be detectable in the phase-resolved spectrum or it could appear asymmetric in the phase-averaged spectrum due to phase-dependence of a symmetric line.

1.4 The aim of this thesis

In this thesis I investigate highly magnetized accreting X-ray pulsars. Of particular interest is the place of origin of their X-ray emission, i.e., the accretion columns on the polar caps of the neutron star. Although there are several physical models describing different aspects of the radiative transfer within the accretion column, a comprehensive model, however, is still needed. Especially, the detailed transformation from the intrinsic reference frame of the neutron star to that of the observer is generally neglected, which introduces geometrical effects and has to be treated general relativistically. In this thesis I present a new and flexible general relativistic ray tracing code easily combinable with physical models providing the emission profile.

In Chapter 2 I present the ray tracing method developed to account for general relativistic effects in the Schwarzschild metric like light bending and gravitational redshift. In contrast to

[3]There is a significant systematic error in the determination of the (flux derived) luminosity, which is part of the discussion in Chapter 3.

previous works this ray tracing method does not require a special geometry of the emission region and is able to apply any emission profile to emission regions of any shape. In Chapter 3 I combine two physical models to obtain a physical description of the emission emanating from accretion columns. One determines the continuum emission of the column dependent on the emission height, angle, and energy, while the other imprints this continuum with cyclotron resonant scattering features. The combination of this physical emission profile and the ray tracing method provides a self-consistent description, for the first time, from the origin of the emission to the observer. Looking at the dependency of the geometrical parameters, it becomes clear, that the geometry of the system as well as general relativity has a significant impact on observational quantities.

In Chapter 4 I show the application of the ray tracing method to observational data for two different cases. In Sect. 4.1 I use a simple phenomenological emission profile to fit the pulse profiles of 4U 1626−67 and their evolution with energy. The profile is a mixture of emission directed along and perpendicular to the B-field, called “pencil beam” and “fan beam”, respectively. In Section 4.2 I present a simple model including a single accretion column to describe the observed phase dependence of the two distinct CRSFs in GX 301−2. While the CRSF of constant energy is formed at the bottom of the column, the variation of the CRSF at lower energy and formed higher in the column is explained by the dependency of the relativistic boosting on the viewing angle.

Finally, I give the conclusion and an outlook for further studies in Chapter 5.

Chapter 2 Ray tracing in curved space-time

The discussion of this relativistic ray tracing method are based on a submitted manuscript (Falkner et al., 2018a) and therefore the subsequent sections are following it closely and in larger parts in verbatim. The development of a limited prototype of this code also was the topic of my Master's thesis (Falkner, 2013), which discusses some of the aspects presented in this Chapter in more detail.

In order to understand the observations of emission which emerges from the close vicinity of a compact object in a physical meaningful manner, general relativistic effects have to be taken into account. Such effects are light bending, which also causes a lensing effect (solid angle amplification), and gravitational redshift. These effects are especially important for neutron stars where we observe emission from the neutron star's surface and from its accretion columns. Note that in the following we consider the neutron star to rotate slowly with periods of $P \gtrsim 1\,\mathrm{s}$ as we focus on HMXBs. This assumption allows us to neglect time delays of observed photons and Doppler boosting. The non-trivial treatment of relativistic rotation (see Sect. 2.4.2) would add a significant degree of complexity to the ray tracing method described in this Chapter and would decrease its efficiency in terms of computational runtime.

For that purpose I developed a relativistic ray tracing code solving the photon trajectories in the Schwarzschild metric to calculate the observed energy and phase dependent flux based on arbitrary geometries and emission patterns of the emission regions.

2.1 General relativistic ray tracing

The following section summarizes the mathematical equations utilized by the relativistic ray tracing code. The trajectories of photons in the Schwarzschild metric are solved to obtain the projection of the geometry on the observer sky. Applying an emission profile to the given geometry then allows us to calculate the observed energy and phase dependent flux. We choose a numerical approach similar to the work by Beloborodov (2002), Poutanen & Beloborodov (2006), and De Falco et al. (2016), who derived the observed flux for infinitesimal spots on a

sphere. We expand this approach by radially extended emission regions in a way similar to Ferrigno et al. (2011) did for conical accretion columns, which allows photon trajectories with a turning point. The method described in the following, however, allows us for the first time to model arbitrary geometrical emission regions, without any required symmetry or any other restriction to the geometrical shape.

2.1.1 Equations of motion

Solving the geodesic equation based on the Schwarzschild metric in spherical coordinates (t, r, θ, ψ) one obtains the equations of motion for photons. In particular, exploiting spherical symmetry and the conservation of angular momentum ($\theta \equiv \pi/2$), the components of the photon's four-velocity can be written as (see, e.g., Misner et al., 1973)

$$u^t \equiv \frac{\mathrm{d}t}{\mathrm{d}\lambda} = (1 - R_\mathrm{s}/r)^{-1} \tag{2.1}$$

$$u^r \equiv \frac{\mathrm{d}r}{\mathrm{d}\lambda} = \left[1 - b^2\,(1 - R_\mathrm{s}/r)\,/r^2\right]^{1/2} \tag{2.2}$$

$$u^\theta \equiv \frac{\mathrm{d}\theta}{\mathrm{d}\lambda} = 0 \tag{2.3}$$

$$u^\psi \equiv \frac{\mathrm{d}\psi}{\mathrm{d}\lambda} = b r^{-2} \quad , \tag{2.4}$$

where R_s is the Schwarzschild radius (Eq. 1.1) and b the impact parameter, i.e., the distance between the trajectory and the line of sight, which connects the center of the neutron star and the observer (Fig. 2.1). The impact parameter can be expressed in terms of the radial emission angle α, i.e., the angle between the radial position vector, $\boldsymbol{n}$, and the initial emission direction of the photon, $\boldsymbol{k}^\star$. With Eqs. (2.2–2.4),

$$\tan(\alpha) = \left.\frac{|u^\psi|}{|u^r|}\right|_{\theta=\frac{\pi}{2}} \tag{2.5}$$

such that

$$b = \frac{R \sin\alpha}{\sqrt{1 - R_\mathrm{s}/R}} \quad . \tag{2.6}$$

The trajectory of the photon can then be described by the elliptical integral

$$\begin{aligned} \psi_b(R) &= \int_R^\infty \frac{\mathrm{d}\psi}{\mathrm{d}\lambda}\frac{\mathrm{d}\lambda}{\mathrm{d}r}\,\mathrm{d}r \\ &= \int_R^\infty \frac{\mathrm{d}r}{r^2}\left[\frac{1}{b^2} - \frac{1}{r^2}\left(1 - \frac{R_\mathrm{s}}{r}\right)\right]^{-1/2} \quad , \end{aligned} \tag{2.7}$$

where ψ is the polar angle between the direction to the observer at infinity and the current location R of the photon (see Fig. 2.1). Note that R is not necessarily equal to the radius of the neutron star which is denoted with R_NS, i.e., $R \geq R_\mathrm{NS}$.

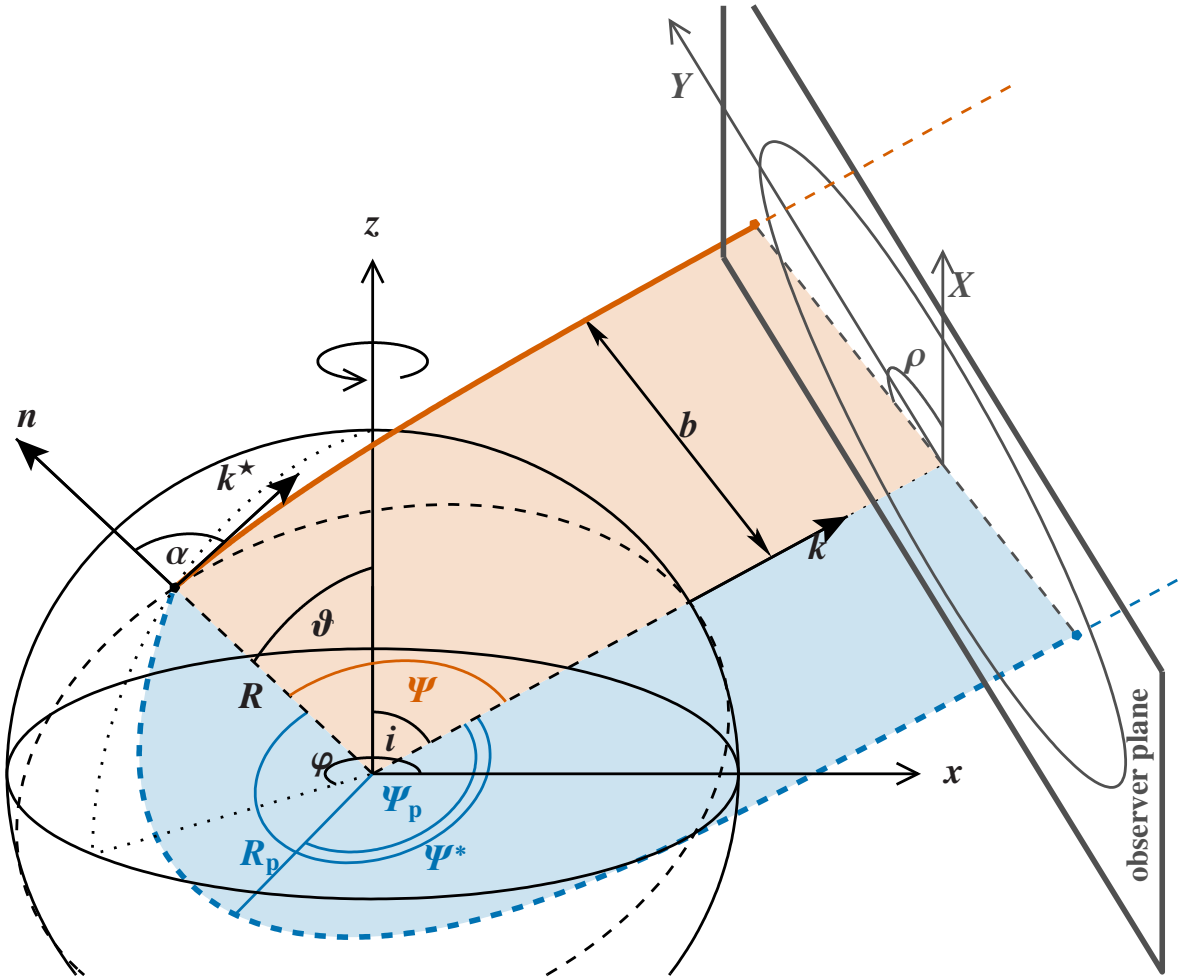

Figure 2.1.: Visualization of the ray tracing parametrization. The orange solid line represents the trajectory of photons emitted at (R, φ, ϑ) in the direction $\boldsymbol{k}^\star$ with the emission angle α with respect to the radial vector $\boldsymbol{n}$. R represents the radius of emission. The photon reaches the observer plane (at infinity) at the impact point ($X = b\cos\rho, Y = b\sin\rho$) at a distance b. The direction $\boldsymbol{k}$ towards the observer is defined to lie in the x,z-plane, inclined by the inclination i with respect to the z-axis, which is also the axis of rotation. The angle between $\boldsymbol{n}$ and $\boldsymbol{k}$ is the apparent emission angle Ψ. The blue dashed line represents the second possible trajectory, Ψ^*, to the observer of a photon emitted at (R, φ, ϑ). In this case the photon is emitted towards the neutron star, that is, $\alpha > 90°$ and exhibits a periastron at $(R_\mathrm{p}, \Psi_\mathrm{p})$.

The travel time, i.e., the time the photon following the trajectory in Eq. (2.7) needs to reach the observer, is given by

$$\begin{aligned} ct_b(R) &= \int_R^\infty \frac{\mathrm{d}t}{\mathrm{d}\lambda}\frac{\mathrm{d}\lambda}{\mathrm{d}r}\,\mathrm{d}r \\ &= \int_R^\infty \mathrm{d}r \left(1-\frac{R_\mathrm{s}}{r}\right)^{-1}\left[1-\frac{b^2}{r^2}\left(1-\frac{R_\mathrm{s}}{r}\right)\right]^{-1/2} . \end{aligned} \tag{2.8}$$

For an observer placed at infinity the travel time also is infinity. To avoid this problem we define a more suitable parameter, the time delay

$$\begin{aligned} c\Delta t_b(R) &= c\left[t_b(R) - t_0(R_{\rm ref})\right] \\ &= \int_R^\infty \mathrm{d}r \left(1 - \frac{R_{\rm s}}{r}\right)^{-1} \left\{\left[1 - \frac{b^2}{r^2}\left(1 - \frac{R_{\rm s}}{r}\right)\right]^{-1/2} - 1\right\} - R_{\rm s} \ln\left(\frac{R - R_{\rm s}}{R_{\rm ref} - R_{\rm s}}\right) - R + R_{\rm ref} \quad , \end{aligned} \tag{2.9}$$

which is the difference of the travel time $t_b(R)$ of a photon emitted at radius R with and impact parameter b and the reference travel time $t_0(R_{\rm ref})$ with a freely chosen reference radius $R_{\rm ref}$ and impact parameter $b = 0$. For simultaneous emitted photons the time delay in Eq. (2.9) describes the difference in arrival times at the observer. This time delay is in the order of 10^{-4} s and depends only slightly on the compactness of the neutron star and the dimension of the emission region. Therefore the time delay is negligible for pulsars with a spin period $\gtrsim$1 s and is only important for rapidly spinning pulsars such as millisecond pulsars.

Those trajectories in Eq. (2.7) with $\alpha \geq 90°$, i.e., photons emitted towards the neutron star, can exhibit a periastron at

$$R_{\rm p}(b) = -2\sqrt{\frac{b^2}{3}} \cos\left[\frac{1}{3}\arccos\left(\frac{3\sqrt{3}}{2}\frac{R_{\rm s}}{b}\right) + \frac{2\pi}{3}\right] \quad , \tag{2.10}$$

where $\alpha = 90°$ corresponds to the periastron itself. Equation (2.10) is only valid for $b > b_{\rm c}$, with the critical impact parameter

$$b_{\rm c} = \frac{3\sqrt{3}}{2} R_{\rm s} \quad , \tag{2.11}$$

and the critical radius

$$R_{\rm c} = R_{\rm p}(b_{\rm c}) = \frac{b_{\rm c}}{\sqrt{3}} = \frac{3}{2} R_{\rm s} \quad , \tag{2.12}$$

below which photon trajectories do not exhibit a periastron and spiral inwards to the center of mass. From Eq. (2.6) we derive the maximum radial emission angle,

$$\alpha_{\rm max} = \pi - \arcsin\left(\frac{b_{\rm c}}{R}\sqrt{1 - \frac{R_{\rm s}}{R}}\right) \quad . \tag{2.13}$$

To account for periastra, the photon trajectory in Eq. (2.7) and the corresponding time delay in Eq. (2.9) have to be considered, such that

$$\Psi_b(R) = \begin{cases} \psi_b(R) & \text{for} \quad \alpha \leq 90° \\ 2\psi_b(R_{\rm p}) - \psi_b(R) & \text{for} \quad \alpha > 90° \end{cases} \tag{2.14}$$

and

$$\Delta T_b(R) = \begin{cases} \Delta t_b(R) & \text{for} \quad \alpha \leq 90° \\ 2\Delta t_b(R_{\rm p}) - \Delta t_b(R) & \text{for} \quad \alpha > 90° \end{cases} \quad . \tag{2.15}$$

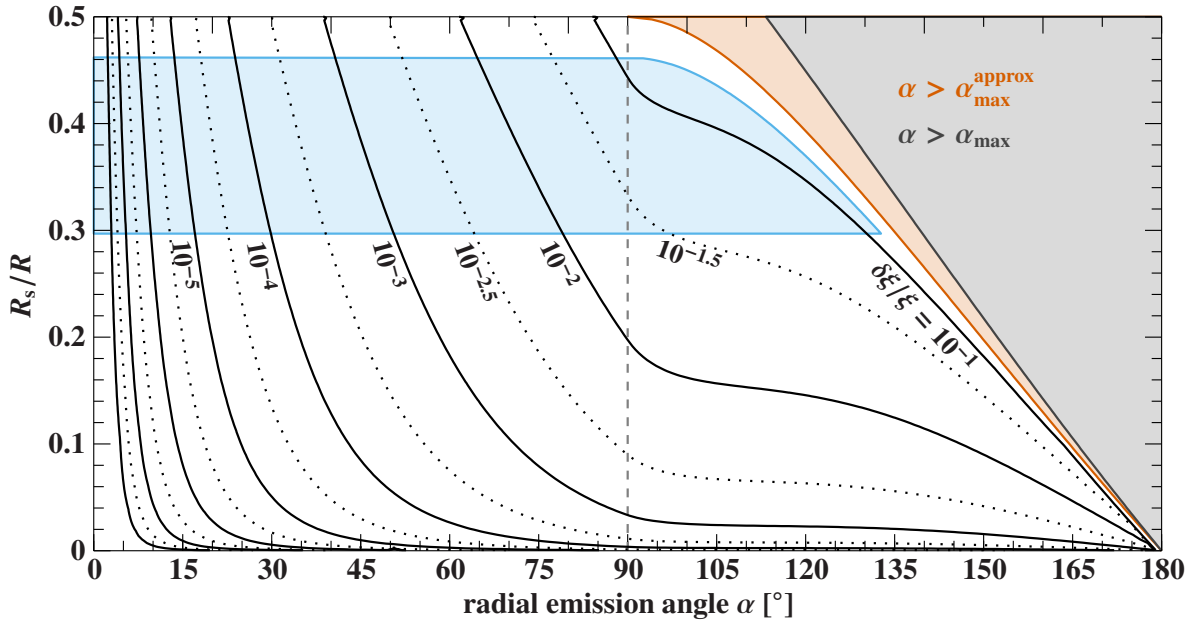

Figure 2.2.: Accuracy of the analytical photon trajectory approximation (Eq. 2.16). This figure is similar to Beloborodov (2002, Fig. 2) and shows contour lines (solid, dotted) of constant deviation $\delta\xi/\xi$ of the bending angle $\xi = \Psi - \alpha$ of the analytical approximation (Eq. 2.16) to the exact solution (Eq. 2.14). The black and orange shaded regions relate to the maximum radial emission angles, α_{max} and α_{max}^{approx}, for the exact and approximated case, respectively. The blue shaded area confines the region that can be occupied by a neutron star with $M_{NS} = 1.4\,M_\odot$ (see, e.g., Steiner et al., 2013). Note that the y-axis of Beloborodov (2002, Fig. 2) actually begins at $R_s/R = 0.01$ and not at 0 as implied in their figure.

2.1.2 Analytic approximation

Beloborodov (2002) presents a very accurate analytical approximation for the photon trajectory in Eq. (2.7) given by

$$1 - \cos\alpha = (1 - \cos\psi)(1 - R_s/R) \quad , \tag{2.16}$$

which De Falco et al. (2016) derive in a more general approach. This approximation requires that $R > 2R_s = R_c^{approx}$. Note that the critical radius in this approximation is larger than that of the exact solution (Eq. 2.12). In other words, in the approximation of Beloborodov (2002) a neutron star with a radius of $2R_s$ would look like a neutron star of a radius $\frac{3}{2}R_s$ based on the exact calculation. Objects therefore appear to be more compact when using the approximate solution rather than the exact calculation.

Considering the bending angle, $\xi = \Psi - \alpha$, which is the most crucial parameter for ray tracing, its deviation, $\delta\xi/\xi$, from the exact solution is small (Fig. 2.2), reaching 10% only in the extreme case of $\alpha \to \alpha_{max}$ (Eq. 2.13).

For $\alpha \leq 90°$ the accuracy map in Fig. 2.2 matches that of Beloborodov (2002, Fig. 2), which shows the correctness of our numerical calculation of the photon trajectory given by Eq. (2.14). Note that as expected we obtain $\delta\xi = 0$ for $R_s/R \to 0$ and arbitrary α, as the apparent and radial emission angle are equal, i.e., $\alpha = \Psi$.

2.1.3 Sky projection

By setting $\theta \equiv \pi/2$ in the geodesic Equations (2.1–2.4) we can reduce the three dimensional problem into a plane, where a trajectory can be identified only by its impact parameter b. In order to obtain the projected image of a three-dimensional object in the observer plane we need to distinguish between trajectories lying in different planes. The transformation between these planes is basically a rotation around the line of sight, which can be described with the azimuthal angle ρ in the observer plane (see Fig. 2.1). This azimuthal angle allows us to define the impact point (X, Y) of a photon trajectory in the observer plane as

$$X = b\cos\rho \qquad \text{and} \qquad Y = b\sin\rho \quad , \tag{2.17}$$

where ρ is defined by

$$\begin{aligned}\cos\rho &= \frac{[\boldsymbol{k}\times(\boldsymbol{n}\times\boldsymbol{k})]\cdot\boldsymbol{e}_y}{|\boldsymbol{k}\times(\boldsymbol{n}\times\boldsymbol{k})|} \\ &= \frac{\sin\vartheta\sin\varphi}{\sqrt{\sin^2\vartheta\sin^2\varphi + (\sin i\cos\vartheta - \cos i\sin\vartheta\cos\varphi)^2}}\end{aligned} \tag{2.18}$$

and

$$\begin{aligned}\sin\rho &= \frac{\left|[\boldsymbol{k}\times(\boldsymbol{n}\times\boldsymbol{k})]\times\boldsymbol{e}_y\right|}{|\boldsymbol{k}\times(\boldsymbol{n}\times\boldsymbol{k})|} \\ &= \frac{\sin i\cos\vartheta - \cos i\sin\vartheta\cos\varphi}{\sqrt{\sin^2\vartheta\sin^2\varphi + (\sin i\cos\vartheta - \cos i\sin\vartheta\cos\varphi)^2}} \quad ,\end{aligned} \tag{2.19}$$

where

$$\boldsymbol{k} = \begin{pmatrix} \sin i \\ 0 \\ \cos i \end{pmatrix} \tag{2.20}$$

is the direction vector to the observer, which is inclined to the z-axis by the inclination angle i, and

$$\boldsymbol{n} = \begin{pmatrix} \sin\vartheta\cos\varphi \\ \sin\vartheta\sin\varphi \\ \cos\vartheta \end{pmatrix} \tag{2.21}$$

is the radial normal vector. The angle ψ is geometrically described by

$$\cos\psi = \boldsymbol{k}\cdot\boldsymbol{n} = \cos i\cos\vartheta + \sin i\sin\vartheta\cos\varphi \quad . \tag{2.22}$$

The initial emission direction $\boldsymbol{k}^\star$ can be expressed as

$$\boldsymbol{k}^\star = \frac{\sin\alpha}{\sin\Psi}\boldsymbol{k} + \frac{\sin(\Psi-\alpha)}{\sin\Psi}\boldsymbol{n} \quad . \tag{2.23}$$

Note that in case of geometrical projection in flat space-time $\boldsymbol{k}^\star = \boldsymbol{k}$ as $\Psi = \alpha$. Finally, we can express the solid angle occupied by an infinitesimal spot $\mathrm{d}S$ for an observer at distance D in terms of the impact parameters,

$$\mathrm{d}\Omega = \mathrm{d}X\,\mathrm{d}Y/D^2 \quad . \tag{2.24}$$

2.1.4 Observed flux and frames of reference

Using the definitions of the previous sections we are now able to determine the energy- and phase-resolved flux observed from the neutron star. In order to do so, we need to integrate the specific intensity I_E as measured in the observer's rest frame over the solid angle in the observer's sky, Ω, occupied by the surface of the emitting area, S, at rotational phase ϕ, that is

$$F_E(\phi) = \iint_S I_E \, \mathrm{d}\Omega \quad . \tag{2.25}$$

Note that while the geometry of the emitting surface, S, may be static, the corresponding solid angle, which represents the projection on the observer's sky, depends on the rotational phase as well as the line of sight, i.e., $\Omega = \Omega(\phi, S, \boldsymbol{k})$ (Eq. 2.24).

Regarding the specific intensity it is important to distinguish between the different reference frames. In Eq. (2.25) I_E is given in the rest frame of the observer. However, the emission pattern has to be applied to the emitting surface in the rest frame of the neutron star. The transformation of the specific intensity between the rest frame of the neutron star and the rest frame of the observer is given by

$$I_E(\boldsymbol{k}) = \left(\frac{E}{E^\star}\right)^3 I^\star_{E^\star}(\boldsymbol{k}^\star) \quad , \tag{2.26}$$

where

$$E = E^\star \sqrt{1 - \frac{R_\mathrm{s}}{R}} = E^\star / (1 + z) \tag{2.27}$$

refers to the gravitational redshift z a photon suffers, which is emitted at the radius R away from the center of mass with the Schwarzschild R_s. Equation (2.23) gives the transformation between the observed ($\boldsymbol{k}$) and the intrinsic emission direction ($\boldsymbol{k}^\star$) of the photon. Quantities referring to the rest frame of the neutron star or to that of the accretion column are marked with a superscript star (*). This notation is applied to quantities which are not clearly defined in a certain reference frame. For example the radial emission angle α is defined in the rest frame of the neutron star, while its equivalent in the rest frame of the observer is defined as the apparent emission angle Ψ.

In case the bulk motion of the infalling plasma which emits the photons is considered an additional reference frame is introduced. The corresponding transformation of the specific intensity is analog to Eq. (2.26)

$$I^\star_{E^\star}(\boldsymbol{k}^\star) = \left(\frac{E^\star}{E'}\right)^3 I'_{E'}(\boldsymbol{k}') \quad , \tag{2.28}$$

where

$$E' = E^\star \frac{1 + \beta\mu^\star}{\sqrt{1 - \beta^2}} \quad \text{and} \quad \boldsymbol{k}' = \frac{\sqrt{1 - \beta^2}}{1 + \beta\mu^\star} \left[\boldsymbol{k}^\star - \mu^\star \boldsymbol{e}_\beta + \frac{\mu^\star + \beta}{\sqrt{1 - \beta^2}} \boldsymbol{e}_\beta \right] \tag{2.29}$$

is obtained through the Lorentz transformation (see Einstein, 1905) accounting for the bulk velocity $\beta\boldsymbol{e}_\beta$ measured downwards the accretion column in units of the speed of light. $\mu^\star = \boldsymbol{k}^\star \cdot \boldsymbol{e}_\beta$ denotes the projected emission direction in the rest frame of the neutron star, while

$$\mu' = \boldsymbol{k}' \cdot \boldsymbol{e}_\beta = \frac{\mu^\star + \beta}{1 + \beta\mu^\star} \tag{2.30}$$

is that in the rest frame of the emitter. Quantities given in the rest frame of the emitter are marked with a prime ($'$).

2.2 Procedure of the numerical implementation

The following section describes the numerical procedure of the relativistic ray tracing code based on the mathematical equations discussed in the previous section. In contrast to previous works (Beloborodov, 2002, Poutanen & Beloborodov, 2006, Ferrigno et al., 2011) my method calculates the observed flux numerically without the requirement of a special symmetry or any other restrictions to the geometry.

Figure 2.3 gives an overview of the numerical procedure that implements the steps outlined in the previous sections. We first define the geometrical setup, i.e., mass ($M_{\rm NS}$) and radius ($R_{\rm NS}$) of the neutron star, and the spatial extent of the emission region and its location. Using an approach common in Computer graphics, we achieve the independence of symmetrical requirements by sampling the emitting region with a mesh of small triangular[1] surface elements as shown in the left panel of Fig. 2.4. In particular, we sample the surface S of the emitting region with a set of vertices $\boldsymbol{R}_l(R, \varphi(\phi), \vartheta)$, with the index set $l \in L \subset \mathbb{N}$ numbering the individual vertices and where $|L|$ depends on the chosen resolution. These vertices form a mesh of triangular surface elements

$$\Delta \boldsymbol{S}_n = \frac{1}{2}(\boldsymbol{R}_{n_1} - \boldsymbol{R}_{n_0}) \times (\boldsymbol{R}_{n_2} - \boldsymbol{R}_{n_0}) \quad , \tag{2.31}$$

such that each normal vector points outwards and their sum adds up to the emission region, i.e, $\sum_n |\Delta \boldsymbol{S}_n| = S$, where n numbers the surface elements and $n_m \in L$ with $m \in \{0, 1, 2\}$ relates to the corresponding vertices. In other words, each vector $\boldsymbol{R}_l$ may be a vertex in several (up to six) surface elements. The vertex coordinate

$$\varphi(\phi) = \varphi_0 + \phi \tag{2.32}$$

then depends on the initial azimuthal position $\varphi_0 = \varphi(0)$ and on the rotational phase ϕ (see Fig. 2.1). There are no restrictions or requirements to the geometrical shape of the emitting surface, except for $R > R_{\rm c}$.

A pre-calculated interpolation table (Fig. 2.3) is used to perform the relativistic projection. This projection is represented by the solid angle Ω corresponding to the emitting surface S. Based on the geometrical position, which is determined by the radius R and the angle Ψ, we want to calculate the light bending parameters (b, α) required for the projection. The tabulation step is necessary as the calculation of photon trajectories exhibiting a periastron requires the periastron to be known beforehand (see Eq. 2.14). The periastron, however, is determined by the impact parameter, b, of the trajectory (see Eq. 2.10), while the calculation of b requires the emission angle α and the emission radius R (Eq. 2.6). Using Eq. (2.6) and Eq. (2.14) we therefore calculate b and Ψ for given sets of R and α, which together provide the interpolation table. To improve the efficiency the radial range of the table can be limited to the geometrical extent in the given setup.

[1] A triangle formed by three points is the simplest way to define a plane surface (Euclid, ca. 300 BC).

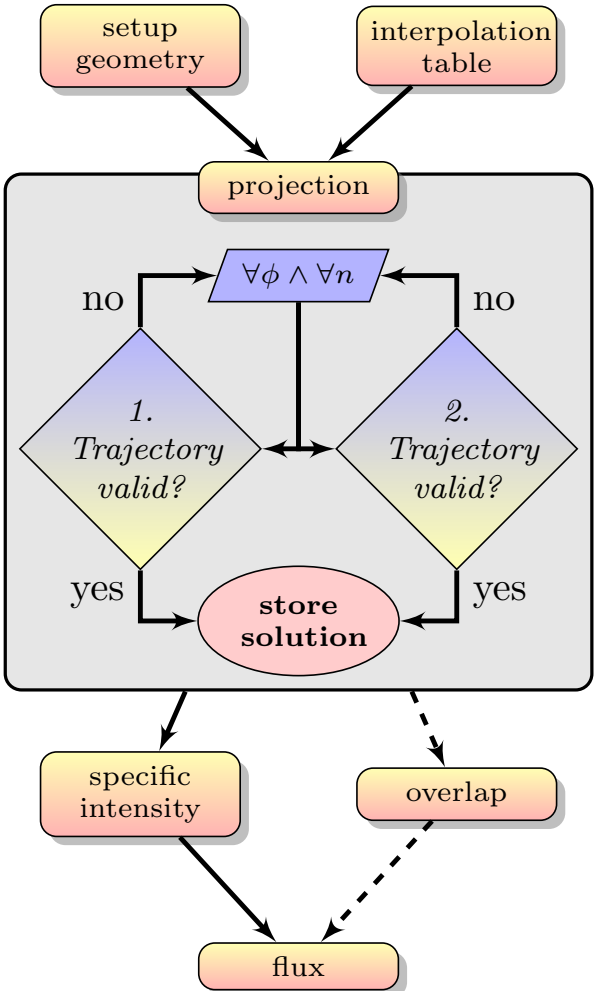

Figure 2.3.: Flow chart sketching the steps of the numerical procedure of the relativistic ray tracing method (see Sect. 2.2). As a first step the geometrical setup, the emitting surface, is defined by a mesh of triangular surface elements. Additionally an interpolation table has to be provided, which contains information of possible photon trajectories. Based on these inputs the main step, the projection onto the observer sky, can be performed. In this step at each phase ϕ for each surface element n the two solutions for photon trajectories (Eq. 2.14) are determined and saved if valid. In an optional step (dashed arrows) overlapping projections are filtered. In the end the given specific intensity is applied to the valid projections of each individual surface element and the resulting overall observed flux is determined.

The main step is the projection (Fig. 2.3) of the 3-dimensional geometrical structure onto the observer sky depending on the rotational phase. This projection is given by the solid angles, $\Delta\Omega_n$, occupied by the corresponding surface elements, $\Delta\boldsymbol{S}_n$. The numerical approximation of the solid angle in Eq. (2.24) is

$$\Delta\Omega_n = \frac{1}{2D^2}\left[(X_{n_2} - X_{n_0})(Y_{n_1} - Y_{n_0}) - (X_{n_1} - X_{n_0})(Y_{n_2} - Y_{n_0})\right] \quad . \tag{2.33}$$

Equation (2.33) represents the triangular area enclosed by the impact points (X_{n_m}, Y_{n_m}) at the observer plane corresponding to its vertex set $\boldsymbol{R}_{n_m}$ forming the surface element $\Delta \boldsymbol{S}_n$.

The calculation of the solid angles is performed on a given grid of rotational phases ϕ_j in a series of steps. At each phase only a subset of the surface elements has a valid projection. The individual steps and different criteria for a valid projection at given phase are described in the following.

First, using Eq. (2.22) we determine Ψ_{n_m} for all according vertex sets n_m geometrically based on the line of sight, $\boldsymbol{k}$, and the current location, $\boldsymbol{R}_{n_m}$. From the interpolation table we can then obtain the corresponding ray tracing parameters, b_{n_m} and α_{n_m}, for the two possible trajectory sets, Ψ_{n_m} and $2\pi - \Psi_{n_m}$ (see Fig. 2.1). Both solutions are checked for validity. A trajectory set is dismissed, if for any n_m

$$\alpha_{n_m} > 90^\circ \quad \wedge \quad b_{n_m} < R_{\mathrm{NS}} / \sqrt{1 - R_{\mathrm{s}}/R_{\mathrm{NS}}} \tag{2.34}$$

or equivalently

$$R_{\mathrm{p}}(b_{n_m}) < R_{\mathrm{NS}} \tag{2.35}$$

as these intersect with the neutron star surface. In other words the corresponding surface element, $\Delta \boldsymbol{S}_n$, would be at least partially invisible, i.e., in the shadow of the neutron star (see Fig. 3.13). To obtain the initial photon emission direction $\boldsymbol{k}_n^\star$ for each valid solution, single ray tracing parameters are determined by averaging according to

$$\alpha_n = \frac{1}{3} \sum_m \alpha_{n_m} \quad \text{and} \quad b_n = \frac{1}{3} \sum_m b_{n_m} \quad . \tag{2.36}$$

From Eq. (2.23) we then obtain the corresponding initial emission direction $\boldsymbol{k}_n^\star$ and the emission angle, η_n, relative to the surface normal vector, where

$$\cos \eta_n = \boldsymbol{k}_n^\star \cdot \Delta \boldsymbol{S}_n / |\Delta \boldsymbol{S}_n| \quad . \tag{2.37}$$

Surface elements with relative emission angles $\eta_n > 90^\circ$, i.e., trajectories pointing inwards into the emitting surface, are dismissed. As a result there are either zero, one, or even two projections, $\Delta\Omega_n$, for each surface element, $\Delta \boldsymbol{S}_n$, at a given phase. The latter case is very improbable and requires a special kind of geometry, which exhibits surface elements with normal vectors pointing towards the neutron star surface, for example an emission region detached from the neutron star surface.

An optional step is to check for overlapping projections (Fig. 2.3), i.e, solid angles $\Delta\Omega_n$ that (partially) occupy the same area in the observer sky. This check is very time consuming and also unnecessary in most cases. An example are solid columns which are located roughly on opposite sides of the neutron star. Their projections do not occupy the same area at any phase (see, e.g., Fig. 3.12). For hollow columns or columns located very close to each other, however, it is likely that there are photon trajectories which are intercepted by another part of the emission region. In such cases adjacent solid angles in the observer's sky have to be checked for overlaps and those shadowed by another are tagged as invalid.

Finally, at each phase we apply the specific intensity, I_E, to each surface element with at least one valid solution and determine the overall observed flux with

$$F_E(\phi) = \sum_n I_E \Delta\Omega_n \quad , \tag{2.38}$$

which represents the numerical approximation of Eq. (2.25). In particular that means, that each surface element is allowed to exhibit an individual specific intensity. Note that I_E is given in the observer rest frame accounting for gravitational redshift (Eqs. 2.26 and 2.27) and for relativistic boosting due the bulk motion of the infalling emitting plasma (Eqs. 2.28 and 2.29).

2.3 Code comparison

As application and verification of the ray tracing code presented in Sect. 2.2 we compare its result to that of Ferrigno et al. (2011). In their work they present semi-analytical calculations of pulse profiles accounting for light bending. They exploit the special symmetry conical accretion columns exhibit to solve the differential solid angle analytically. In particular the apparent emission angle Ψ is constant along the vertical extent of the conical column (see Ferrigno et al., 2011, for details).

First, we adopt the geometrical setup used by Ferrigno et al. (2011). The two conical accretions columns have the same dimensions, i.e., a half opening angle $\omega_{\mathrm{AC1,2}} = 4°$ and a height $h_{\mathrm{AC1,2}} = 2$ km. As shown in the left panel of Fig. 2.4 the two columns are positioned asymmetrically on the neutron star. The position of a column is defined by its polar angle Θ_{AC} with respect to the rotational axis z, which corresponds to the inclination of the magnetic field, and its azimuthal angle Φ_{AC} with respect to the x-axis, while the x,z-plane encloses the line of sight ($\boldsymbol{k}$) to the observer. The first column is located at ($\Theta_{\mathrm{AC1}} = 74°$, $\Phi_{\mathrm{AC1}} = 178°$) and the second column at ($\Theta_{\mathrm{AC2}} = 148°$, $\Phi_{\mathrm{AC2}} = 293°$). The asymmetry is determined by the displacement

$$\begin{aligned} \Delta_{\Phi_{\mathrm{AC}}} &= \Phi_{\mathrm{AC1}} - \Phi_{\mathrm{AC2}} - \pi \\ \Delta_{\Theta_{\mathrm{AC}}} &= \pi - \Theta_{\mathrm{AC1}} - \Theta_{\mathrm{AC2}} \end{aligned} \tag{2.39}$$

from the symmetric antipodal case ($\Delta_{\Phi_{\mathrm{AC}}} = \Delta_{\Theta_{\mathrm{AC}}} = 0$). In the present case the displacement is $\Delta_{\Phi_{\mathrm{AC}}} = -65°$ and $\Delta_{\Theta_{\mathrm{AC}}} = -43°$. The geometrical parameters are summarized in Table 2.1. Note that despite the asymmetrical configuration the axes of the accretion columns are perpendicular to the neutron star surface, which is achieve by assuming the B-field axes to be aligned with the neutron star center. Without this assumption an asymmetric setup would be the result of a misalignment of the Dipole-axis causing tilted accretion columns.

Ferrigno et al. (2011) use a mixture of two Gaussian as emission patterns,

$$I^{\star}(\alpha) = \sum_{j=1}^{2} N_j \exp\left[-\frac{1}{2}\left(\frac{\alpha - \alpha_j}{\sigma_j}\right)^2\right] \quad , \tag{2.40}$$

which is a function of the radial emission angle α (see Fig. 2.1) with peak emissivities $\alpha_1 = 0°$ and $\alpha_2 = 150°$, and beam widths $\sigma_1 = \sigma_2 = 28°$.[2] In other words their emission pattern resembles a mixture of pencil and fan beam emission, while the fan beam is directed downwards to the neutron star surface as shown in the left panel of Fig. 2.5. Note that this phenomenological emission pattern is independent of the energy.

The right panel of Fig. 2.4 shows the relativistic projection of the object shown in the left of Fig. 2.4 and the observed specific intensity I (Eq. 2.40) applied to the two asymmetrically

[2] Ferrigno et al. (2011) actually stated that $\sigma_1 = \sigma_2 = 45°$, which however does not match the corresponding emission pattern in their Fig. 9.

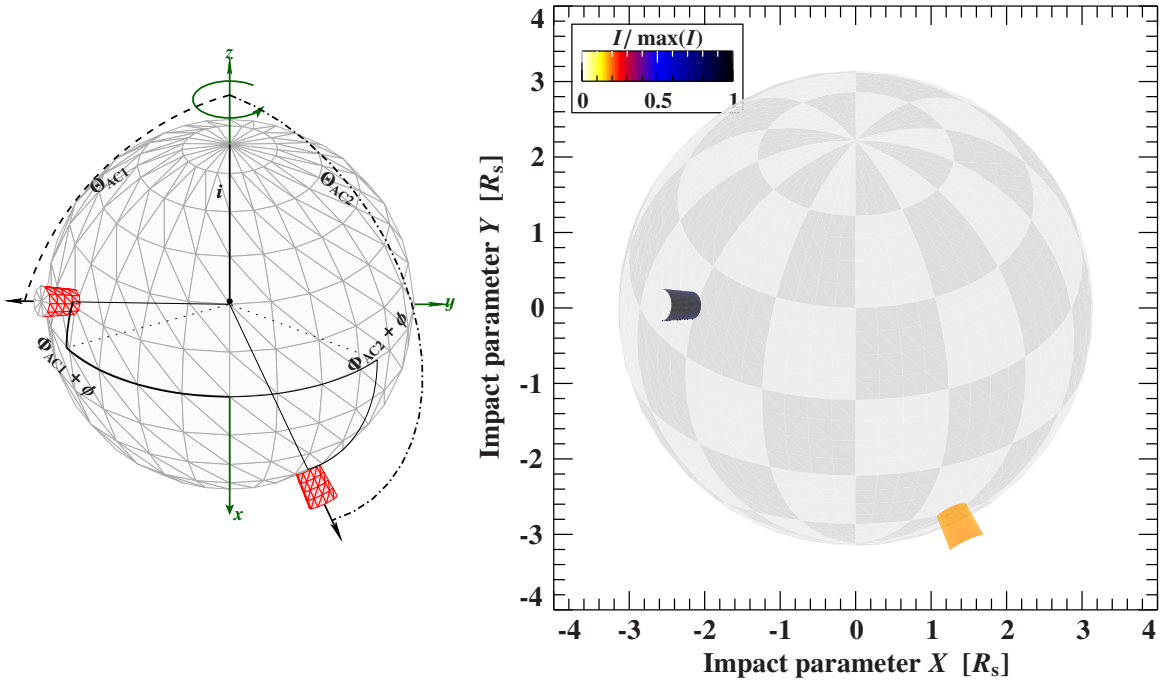

Figure 2.4.: **Left:** Geometrical setup used by Ferrigno et al. (2011) featuring a neutron star with two asymmetrical positioned conical accretion columns. The inclination i of the observer is defined to lie in the x,z-plane and is measured with respect to the rotational axis z (see also Fig. 2.1). The position of the accretion columns is determined by their polar angles, $\Theta_{\rm AC1}$ and $\Theta_{\rm AC2}$, and their according azimuthal angles, $\Phi_{\rm AC1}$ and $\Phi_{\rm AC2}$ (see Table 2.1). The geometry is displayed at phase $\phi = 0.33$. The size of the surface elements is enhanced for visualization purposes. **Right:** Relativistic sky projection of the object shown left roughly to scale. Color coded is the observable specific intensity I (Eq. 2.40).

position columns. It is noticeable that the relativistic projection enlarges the visible fraction of the neutron star's surface, for example both poles are visible which is not the case for the

Table 2.1.: Parameters for the asymmetrical two-column setup in Ferrigno et al. (2011).

global		accretion columns			emission pattern		
			AC1	AC2		pencil ($j=1$)	fan ($j=2$)
$M_{\rm NS}$	$1.4 M_\odot$	$h_{\rm AC}$	2 km	2 km	N_j	100	100
$R_{\rm NS}$	10 km	$\omega_{\rm AC}$	4°	4°	α_j	0°	150°
i	60°	$\Phi_{\rm AC}$	178°	293°	σ_j	28°	28°
		$\Theta_{\rm AC}$	74°	148°			
		displacement					
		$\Delta_{\Phi_{\rm AC}}$	−65°				
		$\Delta_{\Theta_{\rm AC}}$	−42°				

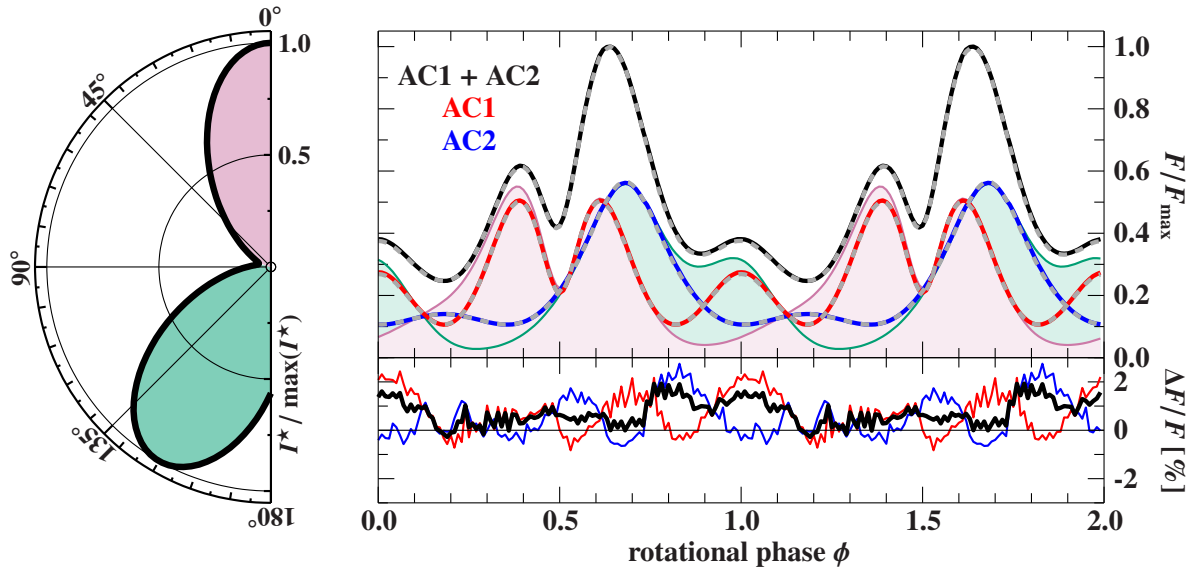

Figure 2.5.: **Left:** Overall normalized intrinsic emission pattern $I^\star$ (black). Purple and green shaded regions indicate the individual contributions of the first ($j = 1$) and second component ($j = 2$), respectively (Eq. 2.40). **Right:** Normalized pulse profiles in comparison. Dashed gray lines relate to calculations by Ferrigno et al. (2011, bottom right panel in Fig. 9) and solid lines to the numerical ray tracing method presented here. Red and blue corresponds to the contribution of the two conical accretion columns, AC1 and AC2, respectively. Purple and green shaded regions again indicate the individual contributions of the first ($j = 1$) and second component ($j = 2$) of both columns combines to the pulse profile, respectively. The overall pulse profile is shown in black. Bottom panel shows the relative difference of the results of the ray tracing code presented here and that by Ferrigno et al. (2011). Parameter values are listed in Table 2.1.

geometrical projection. Also the projection of the columns is deformed. Looking at the second column, its radius seems to be enlarged and its height shortened. Additionally, the viewing angle to the column appears different, i.e., more from above than in the geometrical case. This increase of visibility is a well known effect of general relativistic light bending: Ftaclas et al. (1986) already pointed out that light bending significantly decreases the probability of seeing only one (of two) hot spots compared to the non-relativistic case, while Riffert & Meszaros (1988) stated that this effect to be even stronger for extended accretion columns.

The right panel of Fig. 2.5 shows the overall pulse profile resulting from this asymmetrical configuration (Table 2.1) and the individual contribution of each accretion column. Additionally, the contributions of the pencil- and fan-beam component of the emission pattern to the overall pulse profile are indicated. The pulse profile of each accretion column is symmetric with respect to phase, while their combination is not. This asymmetry of the overall pulse profile is the result of the asymmetric positioning of the columns in phase, i.e., $\Delta_{\Phi_{AC}} \neq 0$. From the first column (AC1) we mainly observe its pencil beam, while it is the fan beam for the second column (AC2). In comparison the ray tracing method described in the previous sections recreates the results by Ferrigno et al. (2011, bottom right panel in Fig. 9) very well,

with deviations overall less than 2%. Note that the calculations by Ferrigno et al. (2011) are based on the analytical approximation by Beloborodov (2002) described in Sect. 2.1.2.

2.4 Possible future features

In the following possible future features and extension for the previously discussed ray tracing code are presented, which are not implemented yet. The statements and results regarding the following methods are based on proof of concept studies, which also ensure the feasibility of these features.

2.4.1 Adaptive mesh refinement

The ray tracing code described in Sect. 2.2 requires a geometry predefined with a mesh of surface elements. This mesh is static in terms of the number of its vertices. In other words the size of each of these surface elements is fixed once the geometry is defined. On the other side, the projection onto the observer plane at different phases is achieved by rotating the mesh around its rotational axis (z-axis). The relativistic projection, however, causes a non-linear deformation of the triangular surface elements. The degree of this deformation increases with the apparent emission angle Ψ (Eq. 2.22) which changes with phase. The projection of a surface element is defined by the projections of its three vertices and therefore is also triangular. Due to the deformation the triangular shape of the projection is only an approximation, which introduces a certain deviation to the exact solution.

To decrease these deviations the size of according surface elements has to be decreased. As the deformation depends on the rotational phase the only option in the case of a static mesh is to decrease the size of all surface elements, which results in a much longer runtime. It would be advantageous to address only those surface elements, which exceed a certain limit of deformation at a given phase.

Such an adaptive mesh refinement could be realized similar to what is described in the following. Analog to the steps described in Sect. 2.2 an initial mesh of vertices $\boldsymbol{R}_l$ is defined, which sufficiently samples the geometrical structure of the neutron star and its emission regions with the according surface elements $\Delta\boldsymbol{S}_n(\boldsymbol{R}_{n_m})$. Instead of directly proceeding with the projection the adaptive mesh refinement sets in. At each rotational phase the vector set $\boldsymbol{R}_{n_m}$ defining the surface element $\Delta\boldsymbol{S}_n$ is temporarily extended by the the median vectors of the three connectors, i.e,

$$\boldsymbol{R}_{n_m} \rightarrow \left\{ \begin{array}{l} \boldsymbol{R}_{n_0}, \boldsymbol{R}_{n_1}, \boldsymbol{R}_{n_2}, \\ \boldsymbol{R}_{n_3} = \dfrac{1}{2}(\boldsymbol{R}_{n_0} + \boldsymbol{R}_{n_1}), \\ \boldsymbol{R}_{n_4} = \dfrac{1}{2}(\boldsymbol{R}_{n_1} + \boldsymbol{R}_{n_2}), \\ \boldsymbol{R}_{n_4} = \dfrac{1}{2}(\boldsymbol{R}_{n_2} + \boldsymbol{R}_{n_0}) \end{array} \right\} \quad . \tag{2.41}$$

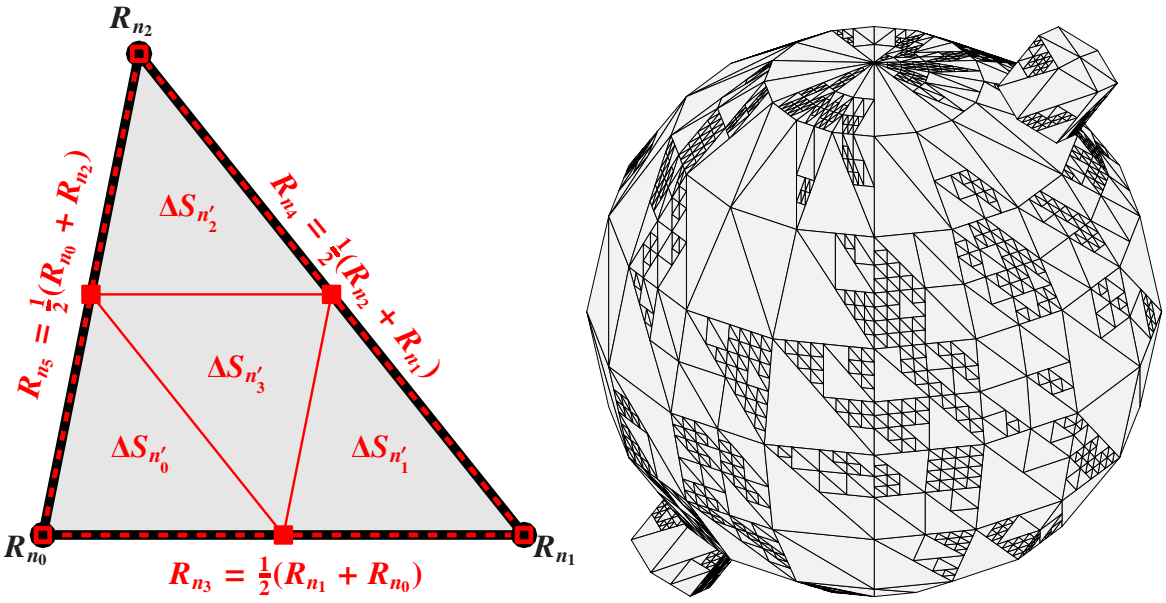

Figure 2.6.: Visualization of the adaptive mesh refinement. The geometry is defined with a static mesh of large surface elements. For demonstration purposes the adaptive mesh refinement is applied randomly with a limit of three iterations.

As shown in Fig. 2.6 these new vertices subdivide the original surface element $\Delta \boldsymbol{S}_n$ into four new surface elements, i.e.,

$$\Delta \boldsymbol{S}_n(\boldsymbol{R}_{n_m}) \rightarrow \begin{cases} \Delta\tilde{\boldsymbol{S}}_{n_0}(\{\boldsymbol{R}_{n_0}, \boldsymbol{R}_{n_3}, \boldsymbol{R}_{n_5}\}) \\ \Delta\tilde{\boldsymbol{S}}_{n_1}(\{\boldsymbol{R}_{n_1}, \boldsymbol{R}_{n_4}, \boldsymbol{R}_{n_3}\}) \\ \Delta\tilde{\boldsymbol{S}}_{n_2}(\{\boldsymbol{R}_{n_2}, \boldsymbol{R}_{n_5}, \boldsymbol{R}_{n_4}\}) \\ \Delta\tilde{\boldsymbol{S}}_{n_3}(\{\boldsymbol{R}_{n_3}, \boldsymbol{R}_{n_4}, \boldsymbol{R}_{n_5}\}) \end{cases} . \tag{2.42}$$

After this subdivision of the mesh the projection of the old and new vertices is performed to obtain the solid angles $\Delta\Omega_n(\Delta \boldsymbol{S}_n)$ of the original surface elements and their corresponding four subdividers $\Delta\tilde{\Omega}_{n_i}(\Delta\tilde{\boldsymbol{S}}_{n_i})$. If the deviation

$$\Delta\Omega_n(\Delta \boldsymbol{S}_n) - \sum_{i=0}^{3} \Delta\tilde{\Omega}_{n_i}(\Delta\tilde{\boldsymbol{S}}_{n_i}) < \epsilon_{\text{lim}} \tag{2.43}$$

for the n-th element is smaller than a given limit ϵ_{lim} the refinement for this surface element is rejected and excluded from the further refinement process. Otherwise, the new median vertices and the according surface elements are accepted and incorporated in the original sets. This process continues until either the condition in Eq. (2.43) is fulfilled for all surface elements or an iteration limit is reached.

This adaptive mesh refinement allows us to automatically ensure that the resolution of the mesh is sufficient to determine the general relativistic projection and only adapts it where necessary. In comparison to a static mesh computational runtime can be saved as it is not required to set a high resolution from the beginning.

As an example, the right panel of Fig. 2.6 shows an object with a refined mesh limited to three iterations. Note that the refinement here is randomly applied for illustration purposes

and not constraint by the condition in Eq. (2.43). The geometry of the neutron star and its two antipodal accretion columns are well described by a rather rough mesh. The mesh refinement does not change the smoothness of the geometry as the subdivision only takes place in the plane defined by the original surface element. Smoothing the geometrical structure is not its purpose, but to provide additional sampling points such that the general relativistic projection is ensured to be performed accurately.

2.4.2 Effects of fast rotation

All previous considerations are based on the assumption of slow rotation with spin periods of $P \gtrsim 1$ s, where photons emitted simultaneously can be assumed to be observed simultaneously. For faster rotations this statement is not true anymore. With increasing spin frequency the order of the rotation period gets comparable to the order of the time delay and additionally special relativistic effects have to be taken into account. The topic of this work are highly magnetized accreting X-ray pulsars, which exhibit rotational periods slow enough to neglect these effects. Nevertheless, effects of fast rotation might be of interest for future applications.

The derivation of the solid angle in Sect. 2.1.3 is based on the equations described in Sect. 2.1.1. These formulas, however, are valid only for values given in the stationary frame of the neutron star. In particular these formulas are based on the assumption that the observed phase equals the intrinsic phase is globally true, i.e., $\phi \equiv \phi^\star$ independent of the location $\boldsymbol{R}$. To account for the effects of special relativity a transformation between the stationary and the co-rotating frame is necessary. In combination with the phase shift introduced by the time delay this transformation results in a complex non-global relation between the intrinsic and observed time. In other words, it is not possible to define a simultaneous time-frame for both, the co-rotating frame of the neutron star and the observer.

2.4.2.1 Photon arrival times

Time cannot be considered global anymore, if the rotation period of the neutron star becomes of the same order as the delay of the photon arrival times given in Eq. (2.15). Therefore we have to distinguish between the intrinsic time $t^\star$ in the stationary frame of the neutron star (Fig. 2.1) and the observed time t. The transformation between these two frames, however, depends on the location $\boldsymbol{R}$.

From Eq. (2.15) we know that photons emitted simultaneously in the stationary frame of the neutron star at a time $t^\star$ arrive at the observer at different times

$$t = t^\star + \Delta T(\boldsymbol{R}(t^\star)) \quad , \tag{2.44}$$

with a relative time delay ΔT according to the current location $\boldsymbol{R}$. The azimuthal position at the intrinsic time $t^\star$ is given by

$$\varphi(t^\star) = \varphi_0 + 2\pi f t^\star \quad , \tag{2.45}$$

where f is the spin frequency of the neutron star and

$$\phi^\star = 2\pi f t^\star \tag{2.46}$$

denotes the rotational phase measured in reference frame of the neutron star.

For the relativistic projection, however, simultaneity in the observer frame is desired. As we cannot simple invert Eq. (2.44) all calculated quantities would have to be interpolated at a given observer time. Alternatively, the approximation

$$\Delta T(\boldsymbol{R}(t^\star)) \approx \Delta T(\boldsymbol{R}(t)) \tag{2.47}$$

can be used (Poutanen & Beloborodov, 2006), with which the time in the stationary frame can be expressed as a function of the observed time,

$$t^\star \approx t - \Delta T(\boldsymbol{R}(t)) \quad . \tag{2.48}$$

The according phase in the stationary frame is then given by

$$\phi^\star \approx \phi - 2\pi f \Delta T(\boldsymbol{R}(\phi)) \quad . \tag{2.49}$$

With this approximation we can maintain simultaneity in the observer frame, while the resulting non-simultaneity in the stationary frame of the neutron star can be accounted for by rotating each vertex $\boldsymbol{R}$ to its local valid phase $\phi^\star$. In other words, to achieve simultaneity at the observer we adjust the location of each vertex to account for the local time delay. As a result, the geometry originally defined in the neutron star's rest frame gets deformed before the projection procedure depending on the given phase.

2.4.2.2 Special relativistic rotation

In addition to the significance of the time delay in photon arrival times fast rotation requires to account for special relativistic effects. In the stationary frame (Fig. 2.1) the rotational velocity around the z-axis in units of the speed of light is given by

$$\boldsymbol{\beta}_{\mathrm{rot}} = \frac{2\pi f}{c}\, \boldsymbol{e}_z \times \boldsymbol{R} = \frac{2\pi f R}{c} \sin\vartheta\, \boldsymbol{e}_\varphi \quad , \tag{2.50}$$

where $\boldsymbol{e}_\varphi$ is the azimuthal unit vector. The direction and the amount of the rotational velocity depends on the current location $\boldsymbol{R}$. Therefore each vertex $\boldsymbol{R}$ has its own individual frame of reference at each given phase, which has to be accounted for in the Lorentz transformation (Eq. 2.29). Following Poutanen & Beloborodov (2006) such an instantaneous frame can be introduced to determine the transformation of the quantities into the stationary and the observer frame. By invoking spherical symmetry, i.e., R = const., it is possible to derive a simple analytical transformation. In the ray tracing method described in this work, however, some additional adjustments are required to account for the radial extent of the emission region, especially in the case of the calculation of the solid angle presented in Sect. 2.2.

Chapter 3

Self-consistent modeling of accretion columns

In this Chapter I present a self-consistent and physically motivated forward methodology to obtain the phase and energy dependent observed flux of an accreting X-ray pulsar. This forward methodology combines three different models, namely a two-dimensional accretion column model in a modified radiation-diffusion limit (Postnov et al., 2015), a cyclotron scattering model (Schwarm et al., 2017a,b), and the new relativistic ray tracing method presented in Chapter 2. This work will be published in Falkner et al. (2018a,b) and therefore the following sections are following them closely and in larger parts in verbatim.

Each model describes different aspects and processes within and around the accretion column based on a common framework. We divide the column itself into two parts (Fig. 3.1), a dense, optically thick ($\tau \gtrsim 1$) inner volume, in which the continuum emission is formed, and a spatially and optically thin layer surrounding this dense region. In the latter region, CRSFs are imprinted onto the continuum. We then transfer the emitted radiation into the observer frame by accounting for light bending and gravitational redshift using the flexible general relativistic code described in Chapter 2.

I emphasize that when performing these calculations we are dealing with three different reference frames, which were introduced in Sect. 2.1.4. The continuum and CRSFs are generated in the rest frame of the down-falling plasma producing and processing the radiation. Note that as the bulk velocity is height dependent each height has its own rest frame. Quantities given in this reference frame are marked with a prime ($'$). Photons generated in the plasma then have to be transformed into the rest frame of the neutron star[1], indicated with a star (*), in order to obtain the emission profile of the column. The transformation into the frame of reference of the observer is then provided by the general relativistic ray tracing.

Here we investigate the regime of strong magnetic fields of $B \sim 10^{12}$ G and accretion rates of $\dot{M} \sim 10^{17}\,\mathrm{g\,s^{-1}}$. These values are sufficiently high to form a (filled) accretion column, which is radiation dominated at its base (Postnov et al., 2015). Furthermore, we consider the

[1] The rest frame of the neutron star is the same as that of the accretion column.

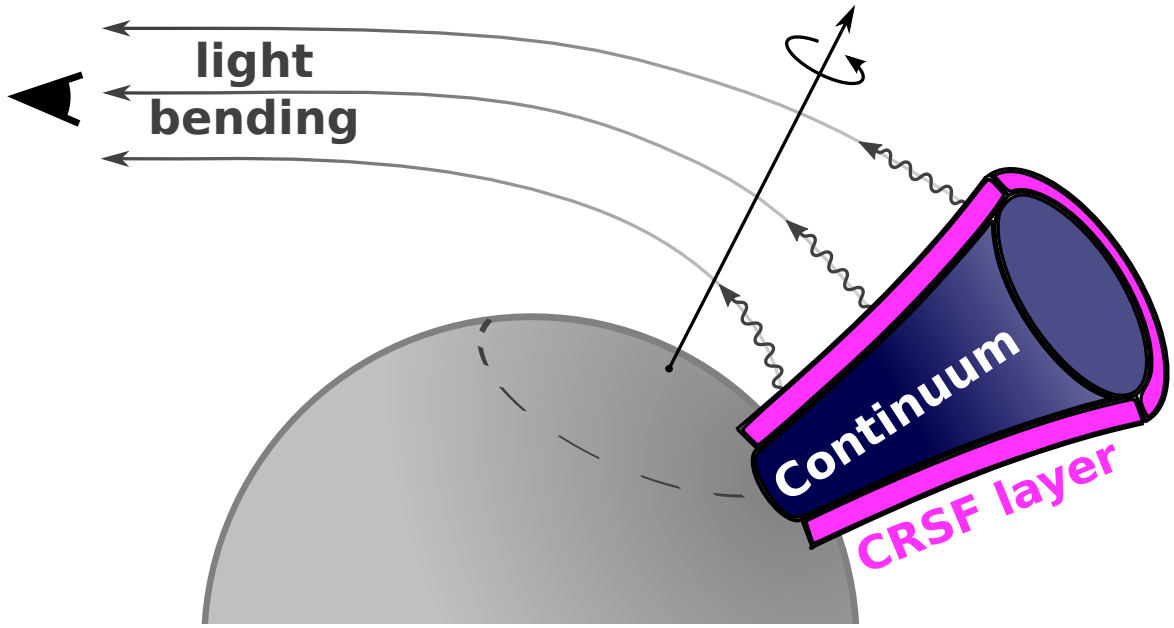

Figure 3.1.: Sketch of the modular physical accretion column model with its three components.

column to be cylindrical and focus on the radiation emerging from its sidewalls as fan-beam. It is commonly accepted from theoretical considerations and observations that this type of column dominates the emission above a critical luminosity (e.g., Wang & Welter, 1981, White et al., 1983, Parmar et al., 1989, Poutanen & Gierliński, 2003). We concentrate on the directly observable fan beam emission. The discussion of possible reflected emission from the neutron star's surface requires additional models describing the atmosphere, although in principle our approach is well suited to take them into account. The atmosphere of neutron stars and its composition, however, is not well understood and therefore is not included in the present model, but subject to future investigations.

In the following I describe the individual parts of this modular model in greater detail. In Sect. 3.1 I describe the continuum and CRSF model, which determine the structure of the accretion column and the formation of its emission self-consistently. Additionally, the resulting emission profile in the rest frame of the accretion column is discussed, which accounts for relativistic boosting due to the local bulk velocity. In Sect. 3.2 I then present observable implications obtained from this combined model and their dependency on the system's intrinsic geometry. Section 3.3 discusses the results of the previous section and relates them to observations.

3.1 Accretion column model

3.1.1 Continuum emission

Based on Wang & Frank (1981) and Lyubarskii (1986), Postnov et al. (2015) performed two-dimensional simulations of axially symmetric accretion columns to study their continuum

emission. They solved the radiative transfer equation in the diffusion approximation to obtain the temperature and velocity distribution within the column volume depending on the vertical and radial location. Additionally, the calculations utilize the grey approximation (e.g., Mihalas, 1978) with effective electron scattering cross sections along and perpendicular to the magnetic field.

Lyubarskii (1986) showed that in the case of a hot and optically thick plasma in a strong B-field the emergent spectrum is formed in the regime of saturated Comptonization. In strong B-fields, collective plasma effects and electron-positron vacuum polarization result in strongly polarization-dependent photon propagation (Mészáros & Ventura, 1978, Pavlov et al., 1980). These polarization modes are called the ordinary and the extraordinary modes. Lyubarskii obtained the analytical solution of the differential Fokker-Planck equation in the diffusion limit in the regime of saturated Comptonization. In optically thick plasmas Comptonization is predominantly effective when acting on extraordinary photons, since here the continuum scattering cross sections are independent of the scattering angle (they are still strongly energy dependent). These photons primarily escape through the sidewalls of the accretion column. Ordinary photons, for which the electron scattering cross sections are strongly angle dependent, escape in directions almost tangential to the surface of the column and provide only an insignificant contribution to the total emitted flux.

The angular dependence of the specific intensity is normally assumed to be proportional to $(1 + 2\cos\zeta')$, where ζ' is the angle with respect to the normal of the emitting surface in the co-moving frame of the emitting plasma (e.g., Lyubarskii, 1986, Postnov et al., 2015). Hence the maximum emission is reached for $\zeta' = 0$ (Fig. 3.2). Starting with this assumption, we can combine Equations (34), (35), and (43) from Lyubarskii (1986), with which the local specific intensity of extraordinary photons in this regime can be written as[2]

$$\mathcal{I}'_{E'}(\mu', \mu_\mathrm{S}, h) = \frac{3}{7\pi}\left[1 + 2\mu_\mathrm{S}\sqrt{1-\mu'^2}\right]\left(\frac{E'}{kT(h)}\right)^2 \frac{F_\perp(h)}{E'} \exp\left(-\frac{E'}{kT(h)}\right) \quad . \tag{3.1}$$

The photon energy E' and $\mu' = \cos\eta'$, where η' is the angle between the B-field and the photon emission direction $\boldsymbol{k}'$, are both given in the rest frame of the emitting plasma (see Fig. 3.2). In the following all primed quantities correspond to the co-moving frame of the plasma, and $\mu_\mathrm{S} = \cos\eta_\mathrm{S}$ is the cosine of the angle of the surface normal to the projection of $\boldsymbol{k}'$ onto the plane perpendicular to the B-field. As the bulk velocity is anti-parallel to the B-field, the plane in which η_S is measured is perpendicular to the velocity vector, and therefore $\mu_\mathrm{S} = \mu'_\mathrm{S}$.

The local electron temperature T used in Eq. (3.1) depends on the location in the column and is given by (Postnov et al., 2015)

$$T(r,h) = \left[\frac{3\dot{M}v_0 c}{4\sigma_\mathrm{SB}\pi r_\mathrm{AC}^2}\left(1 - \sqrt{Q}\right)\right]^{1/4} \quad , \tag{3.2}$$

where the radius r is measured from the center of the column, which has a radius r_AC. The other relevant quantities are the height h, which is measured from the neutron star's surface, the Stefan-Boltzmann constant σ_SB, the mass accretion rate $\dot{M}$, and

$$Q(r,h) = \left(\frac{v(r,h)}{v_0}\right)^2 \tag{3.3}$$

[2]The constant factor of $3/7\pi$ in Eq. (3.1) is chosen such that $\int_0^\infty \int_{-1}^{1} \int_{-\pi/2}^{\pi/2} \mathcal{I}'_{E'} \cos\eta_\mathrm{S} \sqrt{1-\mu'^2}\, \mathrm{d}\eta_\mathrm{S}\, \mathrm{d}\mu'\, \mathrm{d}E' = F_\perp(h)$.

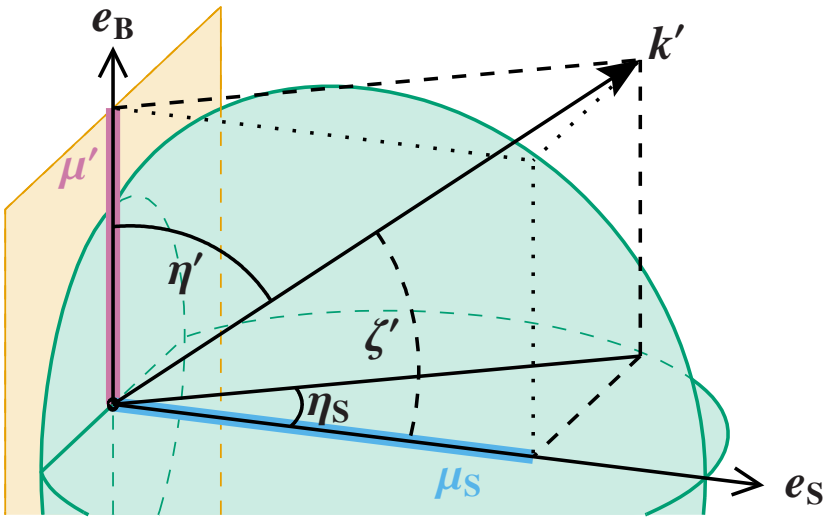

Figure 3.2.: Local co-moving reference frame of the emitting plasma. The direction of the local B-field and the local normal to the emitting (column) surface are denoted by $\boldsymbol{e}_\mathrm{B}$ and $\boldsymbol{e}_\mathrm{S}$, respectively, where $\boldsymbol{e}_\mathrm{B} \cdot \boldsymbol{e}_\mathrm{S} = 0$. The local emission direction of the photon is denoted by $\boldsymbol{k}'$. The photon emerges from the plane of the emitting surface (orange) with an angle ζ' with respect to the surface normal $\boldsymbol{e}_\mathrm{S}$. The angle η' is measured with respect to the B-field, with $\mu' = \cos\eta' = \boldsymbol{k}' \cdot \boldsymbol{e}_\mathrm{B}$. While $\eta_\mathrm{S} = \eta'_\mathrm{S}$ is the angle between the surface normal $\boldsymbol{e}_\mathrm{S}$ and the projection of $\boldsymbol{k}'$ into the plane perpendicular to the B-field, with $\mu_\mathrm{S} = \cos\eta_\mathrm{S}$. The emission pattern, i.e, the angle-dependence of the specific intensity in Eq. (3.1), projected into the three planes of the reference frame is shown in green. The maximum emission is reached for $\zeta' = 0°$ or equivalently $\eta' = 90°$ and $\eta'_\mathrm{S} = 0°$.

where $v(r,h)$ is the velocity inside the column and $v_0 \sim 10^{10}\,\mathrm{cm\,s^{-1}}$ is the initial free-fall velocity of the infalling plasma near the neutron star's surface (see Postnov et al., 2015). In their calculations Postnov et al. (2015) determine the accretion column radius r_AC based on the Alfvén radius as described by Lamb et al. (1973). The radial and vertical component of the radiative transfer equation in the modified diffusion approximation, that is the flux perpendicular and parallel to the magnetic field, can be written as

$$F_\perp(r,h) = \left[\frac{{v_0}^2 c}{2\varkappa_\perp}\frac{\partial Q}{\partial r}\right] \cdot \left[1 + \frac{v_0 \pi r_\mathrm{AC}^2}{6\dot{M}\varkappa_\perp\left(1-\sqrt{Q}\right)}\left|\frac{\partial Q}{\partial r}\right|\right]^{-1} \tag{3.4}$$

and

$$F_\parallel(r,h) = \left[\frac{{v_0}^2 c}{2\varkappa_\parallel}\frac{\partial Q}{\partial z} + \frac{4\dot{M}v_0^2\left(Q-\sqrt{Q}\right)}{\pi r_\mathrm{AC}^2}\right] \cdot \left[1 + \frac{v_0 \pi r_\mathrm{AC}^2}{6\dot{M}\varkappa_\parallel\left(1-\sqrt{Q}\right)}\left|\frac{\partial Q}{\partial z}\right|\right]^{-1} \quad , \tag{3.5}$$

(see Postnov et al., 2015, Eqs. 11–12). Here, $\varkappa_\perp$ and $\varkappa_\parallel$ are the scattering cross sections per unit mass perpendicular and parallel to the magnetic field, respectively. Assuming the accreted matter consists purely of hydrogen, the mean opacity for Thomson scattering is

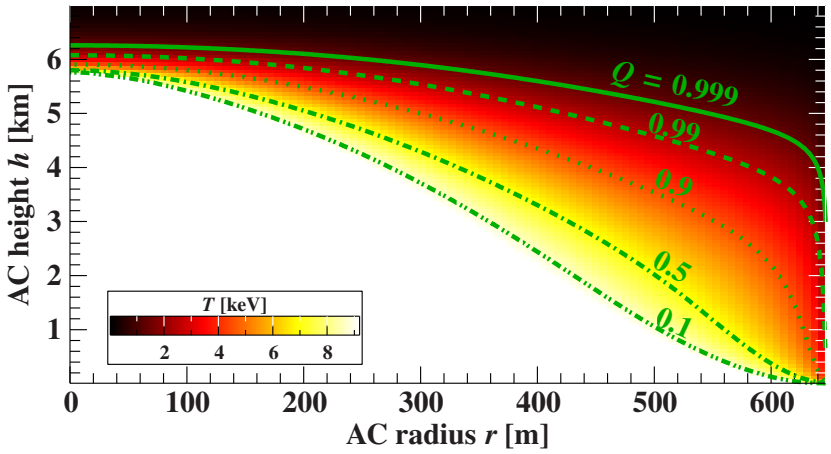

Figure 3.3.: Column structure provided by Postnov et al. (2015). Green lines show the contours of the dimensionless velocity Q for an accretion column of radius $r_{\mathrm{AC}} = 647\,\mathrm{m}$ accreting with a rate $\dot{M} = 5 \times 10^{17}\,\mathrm{g\,s^{-1}}$ and an initial free fall velocity of $v_0 = 1 \times 10^{10}\,\mathrm{cm\,s^{-1}}$. The temperature T throughout the column is shown as colormap.

$\varkappa_{\mathrm{T}} \approx \sigma_{\mathrm{T}}/m_{\mathrm{p}} = 0.398\,\mathrm{cm^2 g^{-1}}$, where σ_{T} is the Thomson cross section and m_{p} is the proton mass. Following Postnov et al. (2015), we assume $\varkappa_{\perp} = \varkappa_{\mathrm{T}}$ and $\varkappa_{\parallel} = \varkappa_{\mathrm{T}}/10$.

Postnov et al. (2015) determine the structure of the accretion column for a variety of different mass accretion rates from a numerical solution of Eq. (3.4) and Eq. (3.5) (see their Fig. 2). Figure 3.3 shows the structure of an accretion column according to a mass accretion rate $\dot{M} = 5 \times 10^{17}\,\mathrm{g\,s^{-1}}$. The initial free fall velocity is $v_0 = 1 \times 10^{10}\,\mathrm{cm\,s^{-1}}$, which is reduced to a settling velocity at the bottom of the column of $\sim 0.14\,v_0$. The region of the radiation-dominated shock, where the accreted matter is decelerated, strongly depends on the radius within the column. With increasing radius r the shock reaches further down to the bottom of the column and extends vertically. As expected from Eq. (3.2) the temperature closely follows the velocity distribution.

From the solution of the column structure provided Postnov et al. (2015) we determine the corresponding energy flux throughout the column. In particular we are interested in the the radial component of the energy flux $F_{\perp}(h)$ emerging the column sidewalls at a certain height and the corresponding temperature $T(h)$ at the boundary layer. With these quantities we can determine the accretion column's specific intensity $\mathcal{I}'_{E'}$ of the continuum. Note that the vertical component of the emerging energy flux is negligible compared to the radial component (Postnov et al., 2015).

At a first glance the radius r_{AC} of the column would be the obvious choice for the boundary. For small optical depths ($\tau \lesssim 1$), however, the transfer equation in Eqs. (3.4–3.5) loses validity. This is true despite the modification, the denominators, to improve the validity of these equations in the outer layers of the accretion column (see Postnov et al., 2015, and references therein). Looking at the evolution of the emerging intrinsic luminosity

$$\mathcal{L}^{\star}(r) = 2\pi r \int_0^{h_{\mathrm{AC}}} F_{\perp}(r, h)\,\mathrm{d}h \tag{3.6}$$

shown in the left panel of Fig. 3.4, we see the luminosity increasing with radius until a certain point after which it significantly drops. Without the modification the luminosity shows the

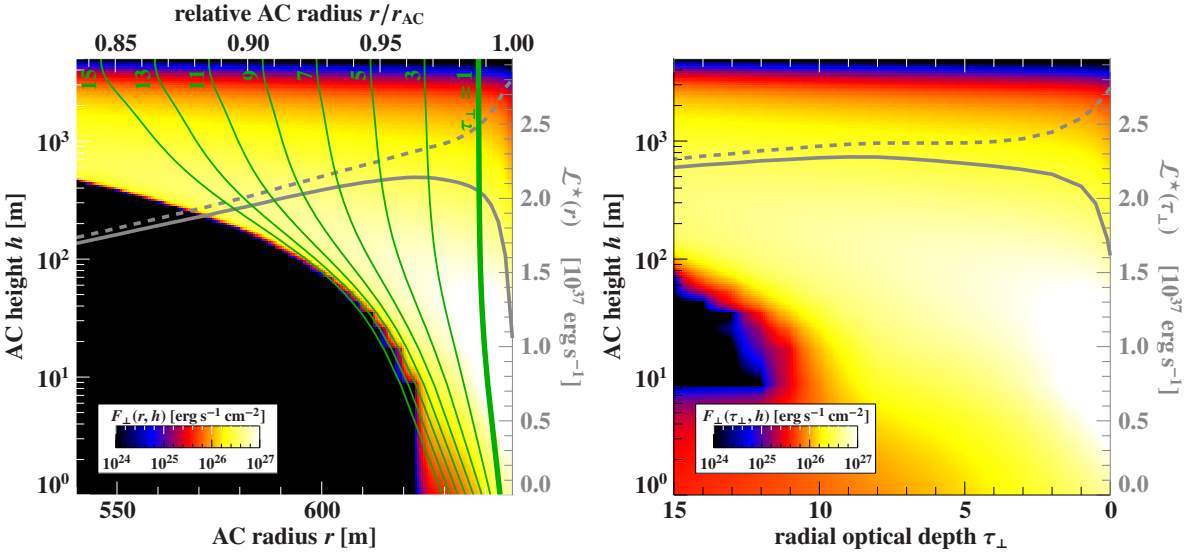

Figure 3.4.: Perpendicular component of the radiative flux depending on height and radius (**left**) and height and radial optical depth (**right**). Green lines represent the contours of the radial optical depth. Gray lines show the luminosity emerging at the surface of constant radius (**left**) and constant radial optical depth (**right**). Solid and dashed gray lines relate to Eq. (3.4) with and without the modifying denominator, respectively.

opposite behavior of a steepening slope close to the boundary. The expectation, however, is a saturation of the luminosity towards the boundary, where $\tau \lesssim 1$.

The right panel of Fig. 3.4 shows the same scenario, but with the radius substituted by the radial component of the local optical depth perpendicular to the B-field given by

$$\tau_\perp(r,h) = \int_{r_{AC}}^{r} \frac{\dot{M}\varkappa_\perp}{\pi r_{AC}^2 v_0 \sqrt{Q}}\, \mathrm{d}\tilde{r} \quad , \tag{3.7}$$

which is measured inwards, with $\tau_\perp(r_{AC}) = 0$. From Eq. (3.7) we obtain the luminosity

$$\mathcal{L}^\star(\tau_\perp) = 2\pi \int_0^{h_{AC}} r(\tau_\perp, h) F_\perp(r,h)\, \mathrm{d}h \tag{3.8}$$

of the column emerging at a given radial optical depth. With this definition we see in Fig. 3.4 that the behavior towards the boundary has improved, but there is still a steepening of the slopes visible. Instead of using the geometrical radius of the column, r_{AC}, in the evaluation of Eqs. (3.4–3.5) we therefore use the radius of constant radial optical depth $r(\tau_\perp = 1, h)$ to represent the boundary. In particular we use

$$F_\perp(h) = F_\perp(\tau_\perp = 1, h) \quad \text{and} \quad T(h) = T(\tau_\perp = 1, h) \tag{3.9}$$

in Eq. 3.1 to calculate the specific intensity of the column. On the one hand, we choose $\tau_\perp = 1$ because the relative deviation from the geometrical radius is very small, $r(\tau_\perp = 1, h)/r_{AC} \geq 98.7\%$, and therefore the assumption of a cylindrical column is still fulfilled. While, on the other hand, the evaluation of the radiative transfer equation at this boundary leads to more reliable results.

3.1.2 Cyclotron line formation

Based on Monte Carlo (MC) simulations of the scattering processes in optically thin and highly magnetized plasma Schwarm et al. (2017a) provide a convolution model for the calculation of CRSFs for arbitrary input continua.

This model uses pre-calculated tables containing the Green's functions for the radiative transfer problem. The tables have been calculated by injecting monoenergetic photons into a given medium, processing them under the assumption that the only type of interaction is cyclotron scattering between electrons and photons, and collecting the output photons escaping the medium. The resulting photons are binned in terms of energy to obtain the Green's functions, the profiles of which can be interpreted as the response of the medium to photons of each particular input energy. Schwarm et al. (2017a,b) describe the process in detail, following the same MC scheme described by Araya & Harding (1999). Non-resonant photons often escape the medium immediately. Resonant photons, on the other hand, tend to scatter very often as their mean free path is shorter by orders of magnitude compared to that of non-resonant photons (Schwarm et al., 2017b). Apart from the B-field strength, the electron temperature parallel to the B-field, and the emission angle, the geometry of the line forming region plays another important role. The influence of the geometry on the cyclotron line shape and emission patterns has been found to be essential for the understanding of CRSFs. Here, we use a cylinder geometry in which photons are emitted from a line along the B-field axis into a surrounding cylinder which has an optical depth $\tau_{\perp}^{\mathrm{CRSF}}$ perpendicular to the B-field axis (Fig. 3.1). The optical depth parallel to the B-field has been set to $\tau_{\parallel}^{\mathrm{CRSF}} = 1000\tau_{\perp}^{\mathrm{CRSF}}$, which approximates a column of infinite height. The pure vacuum modes are used in this model to describe photon polarization states, which is justified by small optical depths in the primary escaping direction (Araya & Harding, 1999). In the following we choose a radial optical depth of $\tau_{\perp}^{\mathrm{CRSF}} = 3 \times 10^{-4}$, which is the primary escaping direction for a cylinder geometry. Note that this rather small optical depth is sufficiently large for the formation of the CRSFs as the cross section in the resonance is several orders of magnitudes larger than in the off-resonance (Schwarm et al., 2017a,b).

The model is able to produce synthetic spectra for a single emission angle, as required for the combination with the relativistic ray tracing model presented in Chapter 2. Interpolation and extrapolation methods ensure that to first order the behavior between pre-calculated grid points is approximated correctly. The strongly energy and angle dependent CRSF spectra provide, for the first time, a possibility for a physical model of the emission from accreting X-ray pulsars.

3.1.3 Emission profile of the accretion column

A crucial point is the combination of the different models, especially in the case of the two models describing the accretion column. In the scenario presented here we use the model described in the previous section to imprint CRSFs on the continuum emission calculated with the model described in Sect. 3.1.1. The continuum photons generated in the dense inner region of the accretion column act as seed photons injected into the thin outer CRSF volume, which we assume to have a negligible spatial extent in radial direction with respect to that of the

continuum volume. This assumption is justified by the fact that the radial optical depth of the CRSF volume is much smaller than that of the continuum formation region, i.e, $\tau_{\perp}^{\mathrm{CRSF}} \ll \tau_{\perp}$.

The CRSF volume itself is characterized by its temperature, magnetic field strength, and optical depth perpendicular to the B-field axis. It is divided into infinitesimally small horizontal slabs to allow us for parameter gradients in the temperature and the magnetic field strength.[3] Nevertheless, we assume $\tau_{\parallel}^{\mathrm{CRSF}}$ of each CRSF slab to be large, which prevents the transition of photons between the individual CRSF slabs. In other words, we assume that photons do not travel between these horizontal slabs and will escape the column at the same height they were injected into the CRSF forming layer. This assumption is a compromise between a physical picture of the accretion column and feasibility of the calculation. A justification for this picture is the spatially thin extent of CRSF layer in the radial direction, which we can assume due to the enormous scattering cross section in the resonance. The mean travel distance of photons in vertical and radial direction is roughly the same. As this distance is limited by the radial extent of the CRSF layer the vertical redistribution of photons is negligible and in particular is much smaller than the vertical extent of the accretion column. Furthermore, we are mainly interested in the angular and energetic redistribution caused by the CRSF medium, whereas the continuum model provides the height dependence of the specific intensity.

The specific intensity of the column including CRSFs is denoted by

$$I'_{E'} = I'_{E'}\left(\mathcal{I}'_{E'}(\mu', \mu_{\mathrm{S}}, h), T, B, \mu', \tau_{\perp}^{\mathrm{CRSF}}\right) \tag{3.10}$$

and results from the convolution of the continuum emission $\mathcal{I}'_{E'}$ (Eq. 3.1) with the CRSF model by Schwarm et al. (2017a,b).

In our case of a cylindrical column[4] the B-field axis and the column axis are aligned. We assume the B-field strength to decrease with height following the dipole approximation,

$$B(r, h) = B_0 \frac{R_{\mathrm{NS}}^3}{2}\left[\frac{5(R_{\mathrm{NS}}+h)^2 r^2 + 4(R_{\mathrm{NS}}+h)^4 + r^4}{[r^2 + (R_{\mathrm{NS}}+h)^2]^5}\right]^{1/2} , \tag{3.11}$$

where $B_0 = B(0,0)$ is the surface magnetic field strength at the center of the column's base and R_{NS} the radius of the neutron star. In Eq. (3.10) the continuum emission (Eq. 3.1) is imprinted with CRSFs at energies $E'_{\mathrm{CRSF}n}$ (Eq. 1.8).

The specific intensity derived in Eq. (3.10) is given in the local rest frame of the emitting plasma. In order to obtain the emission profile of the entire accretion column we have to take into account the height dependency of the relativistic bulk motion to transform the local specific intensity emitted from different parts of the accretion column into a common frame of reference. An obvious choice for such a reference frame is the rest frame of the neutron star. The transformation between the specific intensity in the local rest frame of the plasma (marked with $'$) and the emission profile in the rest frame of the neutron star (marked with *) is obtained through the Lorentz transformation given in Eqs. (2.28–2.30). Note that the velocity vector is antiparallel to the B-field. The CRSF layer is assumed to be coupled to the continuum emitting volume such that both have the same velocity and the same temperature distribution (Eq. 3.2).

[3] As shown by Schwarm et al. (2017a) these parameters have a strong impact on the cyclotron line.

[4] The models by Postnov et al. (2015) and Schwarm et al. (2017a,b), both assume a cylindrically symmetrical magnetic field.

Table 3.1.: Input parameters for the accretion column model. Note that $\dot{M}$ relates to the mass accretion rate of the accretion column and not to that of the neutron star in a whole.

parameter	short	value
initial free fall velocity	v_0	$1 \times 10^{10}\,\mathrm{cm\,s^{-1}}$
mass accretion rate	$\dot{M}$	$5 \times 10^{17}\,\mathrm{g\,s^{-1}}$
accretion column radius	r_{AC}	647 m
accretion column height	h_{AC}	5 km
radial optical depth of boundary	$\tau_\perp$	1
surface magnetic field strength	B_0	$2.5 \times 10^{12}\,\mathrm{G}$
radial optical depth of CRSF layer	$\tau_\perp^{\mathrm{CRSF}}$	3×10^{-4}
neutron star radius	R_{NS}	10 km
neutron star mass	M_{NS}	$1.4\,\mathrm{M}_\odot$

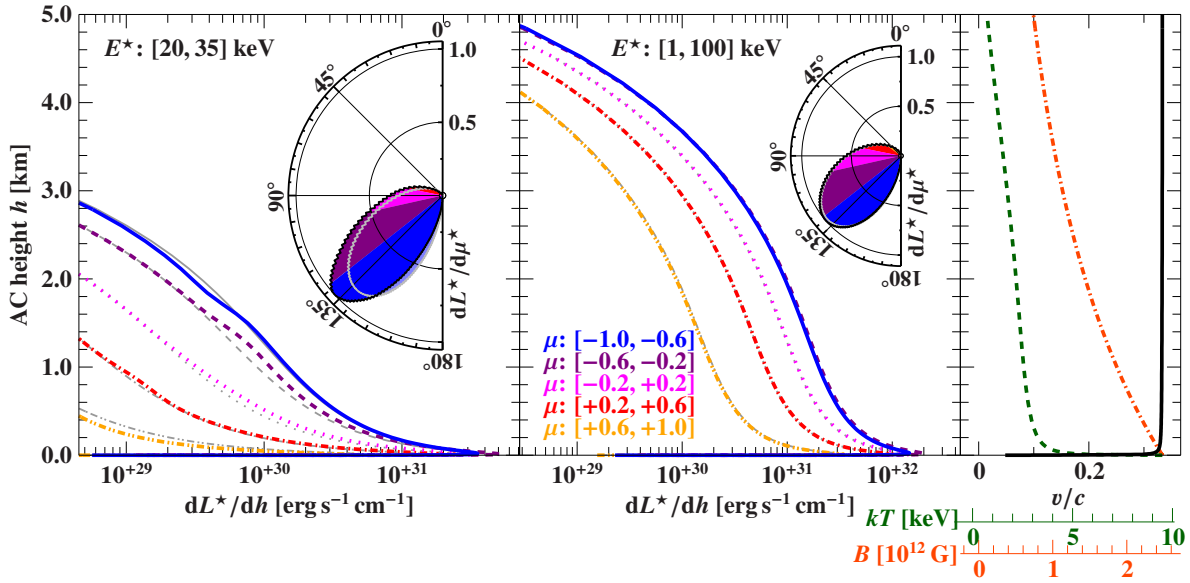

Figure 3.5.: Height dependent emission profile and properties of the accretion column in the rest frame of the neutron star. **Left/middle:** Differential intrinsic luminosity (Eq. 3.12) based on the specific intensity $I^\star_{E^\star}$ integrated over two different energy ranges within different $\mu^\star$ bins shown as colored lines. Gray lines relate to the pure continuum based on $\mathcal{I}^\star_{E^\star}$, that is, without CRSFs. The inset shows the height and energy integrated beam pattern with respect to the angle $\eta^\star$. The colors correspond to the angle bins in the main figure. **Right:** Velocity (solid black), temperature (dashed green), and magnetic field strength distribution (dash-dotted orange) at the boundary layer of the accretion column, i.e., $r = r(\tau_\perp = 1)$.

Figures 3.5 and 3.6 show the height dependent emission profile and other properties of the accretion column for the parameters listed in Table 3.1. In Fig. 3.5 the height dependence of the emissivity is shown in different emission angle bins. All bins show the same behavior, reaching peak emissivity at the bottom of the column. The relative contribution is clearly dominated

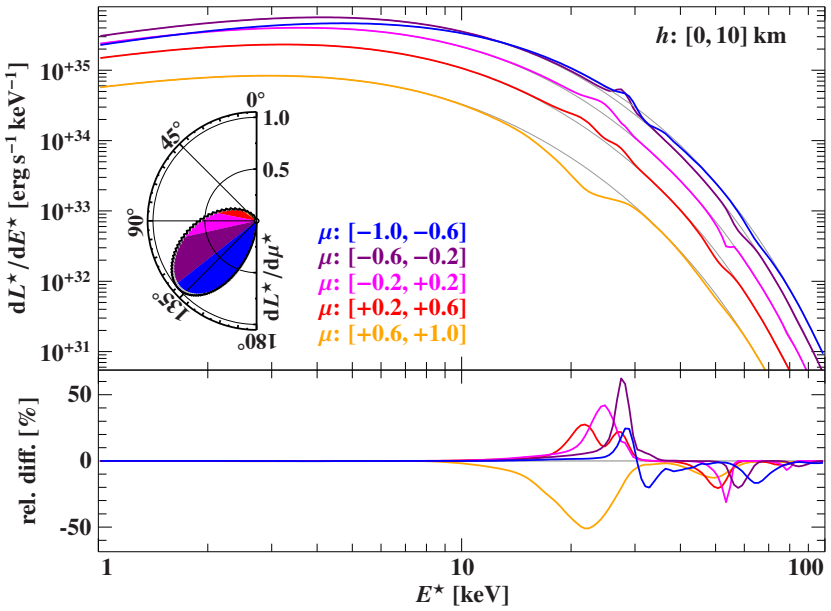

Figure 3.6.: Energy dependent emission profile of a single accretion column in the rest frame of the neutron star. **Top:** Differential intrinsic luminosity (Eq. 3.12) representing the height integrated emerging spectra in different emission angle ranges also indicated in the inset (same as in Fig. 3.5). Gray lines refer to the case without CRSFs. **Bottom:** Relative difference of the spectra to their pure continuum contribution.

by large angles, pointing downwards to the neutron star's surface, due to relativistic boosting (Fig. 3.5, middle). In the left panel of Fig. 3.5, showing the emissivity profile in a small energy range around the fundamental CRSF, the height and angle dependent redistribution due to the cyclotron resonant scattering is noticeable. The bulk velocity at the boundary layer is almost equal to the initial free fall velocity for most parts of the column and only starts to decrease drastically at $h \sim 100\,\mathrm{m}$ above the neutron star's surface (Fig. 3.5, right). The electron temperature shows a similar, but smoother evolution as it is directly derived form the bulk velocity (Eq. 3.2). Figure 3.6 shows the height integrated spectra emerging from the column in the same emission angle bins. Here the effect of the relativistic boosting is responsible for the shift of the CRSF line energy as well as the hardening of the continuum for higher emission angles.

The variation of the luminosity is presented with respect to the intrinsic luminosity in the rest frame of the neutron star $L^\star$, given by

$$L^\star = 2\pi r_{\mathrm{AC}} \int_{E^\star_{\mathrm{min}}}^{E^\star_{\mathrm{max}}} \int_{h_{\mathrm{min}}}^{h_{\mathrm{max}}} \int_{-1}^{1} \int_{-\pi/2}^{\pi/2} I^\star_{E^\star} \cos\eta_{\mathrm{S}} \sqrt{1-\mu^{\star 2}}\, \mathrm{d}\eta_{\mathrm{S}}\, \mathrm{d}\mu^\star\, \mathrm{d}h\, \mathrm{d}E^\star, \tag{3.12}$$

where the X-ray band from 1 to 100 keV approximately contains the total luminosity of the accretion column.

The total intrinsic luminosity of the (single) accretion column is $L^\star = 2.2 \times 10^{37}\,\mathrm{erg\,s^{-1}}$, of which 100% is emitted below a height of 5 km, 67% below 1 km, and 20% below 0.1 km (see Fig. 3.5, middle). Therefore we can consider the column to have a height of $h_{\mathrm{AC}} = 5\,\mathrm{km}$.

In the frame of the moving plasma, the emission is concentrated in the direction normal to the cylindrical column wall (Fig. 3.2). However, due to the boosting (relativistic aberration) caused by the bulk velocity the emission in the frame of the star is predominantly directed downwards, that is, towards the neutron star. In particular 76% of the emission has an emission angle $\eta^\star > 90°$ or $\mu^\star < 0$. The spectra emerging from the column are shown in Fig. 3.6, they strongly depend on the emission angle. Noticeable is that this is true not only for the shape of the cyclotron lines but also for their centroid energies, which get smaller for smaller emission angles. This correlation of the cyclotron resonance criteria results from the bulk velocity boosting (Eq. 2.29). The beam pattern shown in Figs. 3.5 and 3.6 is integrated over the whole energy range and is therefore dominated by the continuum, hiding variations around the CRSFs. Further discussion on the topic of the angular dependency of the specific intensity due to cyclotron resonant scattering can be found in Schönherr et al. (2007) and Schwarm et al. (2017a,b).

3.2 Observables

In the following I present results of the physical accretion column model described previously in Sect. 3.1. I emphasize observable implications and predictions important for interpreting data. Note that in this section I only present results of the simulation based on the previously discussed model. The discussion of these results in comparison to observations is given separately in Sect. 3.3.

In particular, I show and compare results for a single column and an antipodal two-column setup in this section. In the latter case the columns themselves are identical, i.e., parameters are the same for both (see Table 3.1). In particular, these columns are cylindrical with a radius $r_{\mathrm{AC}} = 647\,\mathrm{m}$ (see Postnov et al., 2015), and height $h_{\mathrm{AC}} = 5\,\mathrm{km}$. The spatial extent of the columns is determined by the continuum model (see Sect. 3.1.1) and mainly depends on the initial free fall velocity and the mass accretion rate. As defined in Sect. 2.3 the position of the columns on the neutron star's surface is given by their polar angles $\Theta_{\mathrm{AC1,2}}$, corresponding to the inclination of the magnetic field, and their azimuthal angles $\Phi_{\mathrm{AC1,2}}$ (Fig. 3.7). The azimuthal position is only important in the case of two-column setups. The antipodal configuration requires the columns to fulfill $\Delta_{\Phi_{\mathrm{AC}}} = \Delta_{\Theta_{\mathrm{AC}}} = 0$ (see Eq. 2.39).

A symmetric configuration is the simplest choice and avoids the introduction of additional degrees of freedom, such as individual positioning of the columns and differing accretion parameters. Asymmetric configurations have only a small impact on the results presented in the following Section, for which an example is given in Sect. 3.2.5.6.

Based on this geometrical setup together with the emission profile provided by the physical accretion column model discussed in Sect. 3.1 we determine the energy- and phase-resolved observed flux, $F_E(\phi)$, using the ray tracing code as described in Chapter 2.

3.2.1 Intrinsic and observed luminosity

There are general geometrical constraints on the observable emission of the accretion column due to the presence of the neutron star. Only a fraction of the emission from the column is directly observable. In particular this means that photons exceeding a certain emission angle

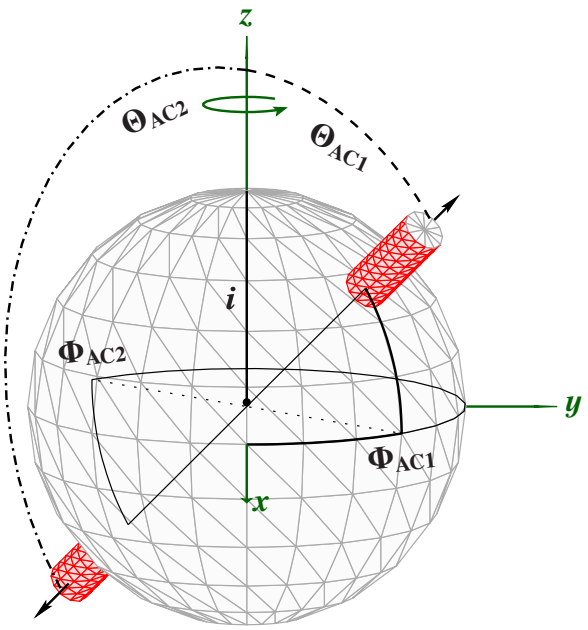

Figure 3.7.: Geometry of a neutron star with two antipodal accretion columns sampled with triangular surface elements. The size of the surface elements is enhanced for visualization purposes. The inclination i of the observer is defined to lie in the x,z-plane. i is measured with respect to the rotational axis z as well as the individual polar angles of the accretion columns, Θ_{AC1} and Θ_{AC2}, respectively. Φ_{AC1} and Φ_{AC2} refer to the azimuthal angles of the corresponding column.

(dependent on the height) will hit the neutron star. For a conical accretion column, using Eq. (2.13) and Eq. (2.6), the maximum observable emission angle is given by

$$\eta^{\star}_{\mathrm{max}}(h) = \pi - \arcsin\left(\frac{R_{\mathrm{NS}}}{R_{\mathrm{NS}}+h}\sqrt{\frac{1-\frac{R_{\mathrm{s}}}{R_{\mathrm{NS}}+h}}{1-\frac{R_{\mathrm{s}}}{R_{\mathrm{NS}}}}}\right) \quad . \tag{3.13}$$

We neglect the extent of the atmosphere as its scale height is only a few centimeters (e.g., Ho & Lai, 2001). Equation (3.13) is also suitable for cylindrical columns with small radii. Figure 3.8 visualizes the maximum observable emission angle, η'_{max}, in the rest frame of the emitting plasma for different bulk velocities[5]. Generally η'_{max} decreases with decreasing height, independent of the boosting factor. The boosting, however, clearly decreases the range of observable emission angles dramatically. As a result in our case 58% of the intrinsic luminosity $L^{\star}$ emitted from the column hits the neutron star, while it would be only 31% without accounting for relativistic boosting. The fraction of the flux not intercepted by the neutron star increases from 31% at the bottom of the column to 70% at a height of 5 km, which is also significantly lower than in the case without relativistic boosting.

[5]Note that the bulk velocity is constant over most of the column and only decreases at the bottom part (see Fig. 3.5).

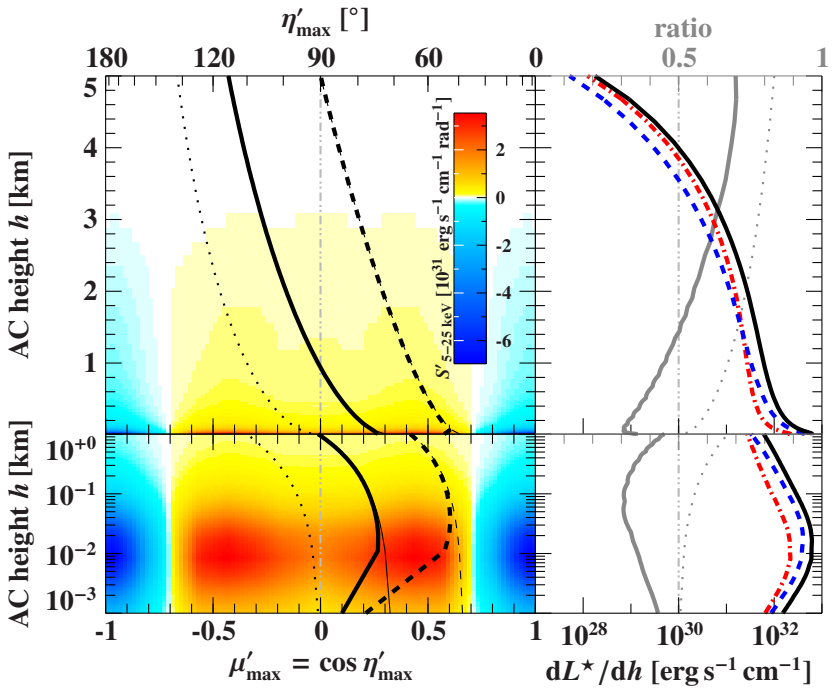

Figure 3.8.: **Left:** Maximum observable emission angle $\eta'_{\rm max}$. Photons emitted with larger angles hit the neutron star. Dotted line accounts for light bending, solid and dashed line also for bulk velocities, v_0 and $2v_0$, respectively. The dash-dot-dotted vertical line indicates the geometrical case in flat space-time. The color map indicates the line strength, S', of the CRSF in the energy range from 5 keV to 25 keV. **Right:** Total flux emitted from the column is shown as solid black line, flux directed to the neutron star as dashed blue line and escaping flux as dotted-dashed red line. The ratio of escaping to total flux is shown as gray solid line, where the gray dotted one shows the ratio assuming isotropic emission in the rest frame of the neutron star. **Bottom:** Zoom-in on the bottom part of the column in logarithmic presentation.

Using Eq. (2.25) the bolometric luminosity L in the band from between 1 keV to 100 keV is given by

$$L = D^2 \int_{1\,\rm keV}^{100\,\rm keV} \int_0^{2\pi} \int_{-1}^{1} F_E \, \mathrm{d}\cos i \, \mathrm{d}\phi \, \mathrm{d}E \quad , \tag{3.14}$$

where D is the distance of the observer to the source. The bolometric luminosity represents the observed luminosity and accounts for a potential anisotropy of the flux.

If we want to relate the bolometric luminosity L to the intrinsic luminosity $L^\star$ (Eq. 3.12) we have to account for gravitational redshifting and time dilatation (Thorne, 1977). Additionally L in Eq. (3.14) corresponds only to the directly-observed luminosity

$$L \approx \left(1 - \frac{R_{\rm s}}{R_{\rm NS}}\right) L^\star \big|_{\eta^\star < \eta^\star_{\rm max}} = (1 + z_{\rm NS})^{-2} \, L^\star \big|_{\eta^\star < \eta^\star_{\rm max}} \quad . \tag{3.15}$$

For our setup (see Table 3.1), $L = 0.8 \times 10^{37}$ erg s^{-1} for one column, which is only 35% of the corresponding total intrinsic luminosity, $L^\star$. Note that in general L cannot be deduced from

observations since information is missing on how the emission depends on the inclination, i. The best approximation is to assume the observed flux F_E to be constant in i, in order to get the flux derived luminosity

$$L_{4\pi} = 2D^2 \int_{1\,\mathrm{keV}}^{100\,\mathrm{keV}} \int_0^{2\pi} F_E \, \mathrm{d}\phi \, \mathrm{d}E \quad . \tag{3.16}$$

In other words, the flux derived luminosity represents the observed luminosity assuming the flux to be isotropic.

3.2.2 Phase-averaged spectra

Figure 3.9 shows the phase-averaged spectra of one accretion column in the observer frame for different inclinations i and Θ_{AC1},

$$\langle F_E \rangle_\phi = \frac{1}{2\pi} \int_0^{2\pi} F_E \, \mathrm{d}\phi \quad . \tag{3.17}$$

The continuum strongly depends on i and Θ_{AC1}, i.e., with increasing i the flux increases and the slope steepens. As expected, the observed cyclotron lines also strongly depend on these parameters as they directly influence the angles under which the column is seen. In comparison to the cyclotron line behavior in the rest frame of the column (see Fig. 3.6) the centroid energies E_{CRSF} are shifted to lower energies. This shift is a result of the gravitational redshift (Eq. 2.27), while the variation in the line energy seems to have decreased. In particular the observed CRSF energy is related to the intrinsic CRSF energy (Eq. 1.9) by

$$E_{\mathrm{CRSF}n} = E'_{\mathrm{CRSF}n} \frac{\sqrt{1-\beta^2}}{1+\beta\mu^\star} \sqrt{1-\frac{R_\mathrm{s}}{R}} \quad , \tag{3.18}$$

where n is the order of the Landau level and $n = 1$ corresponds to the fundamental line and $n = 2$ to the first harmonic. The large range of $E^\star_{\mathrm{CRSF}}$ in the rest frame of the neutron star is caused by the boosting due to the bulk velocity (Eq. 2.29). The observer, however, only sees photons emitted up to a maximum emission angle $\eta^\star_{\mathrm{max}}$ (Eq. 3.13). Photons emitted with larger angles will hit the neutron star's surface, which limits the observable emission angle range and therefore decreases the variation of E_{CRSF}.

In the antipodal two-column case (Fig. 3.10) we see a similar behavior. The fundamental CRSF, however, is now only seen in emission. The reason for this peculiarity – which contradicts observations – is that the fundamental CRSF is observed in absorption only if the viewing angles to the magnetic field are predominantly small over all rotational phases. This is the case, for example, for geometries with a small observer inclination as well as small polar angles of the B-field where the observer sees the column mainly from above. In these cases, the flux derived luminosity of this column is low, and in fact it is surpassed by the emission from the second column, which is located on the far side of the neutron star. This second column is seen under larger angles with respect to the B-field, where the fundamental CRSF is observed in emission. In combination, the greater part of the observed flux comes from the column showing a fundamental CRSF in emission. A more detailed discussion of the CRSFs is given in Sect. 3.2.5.5.

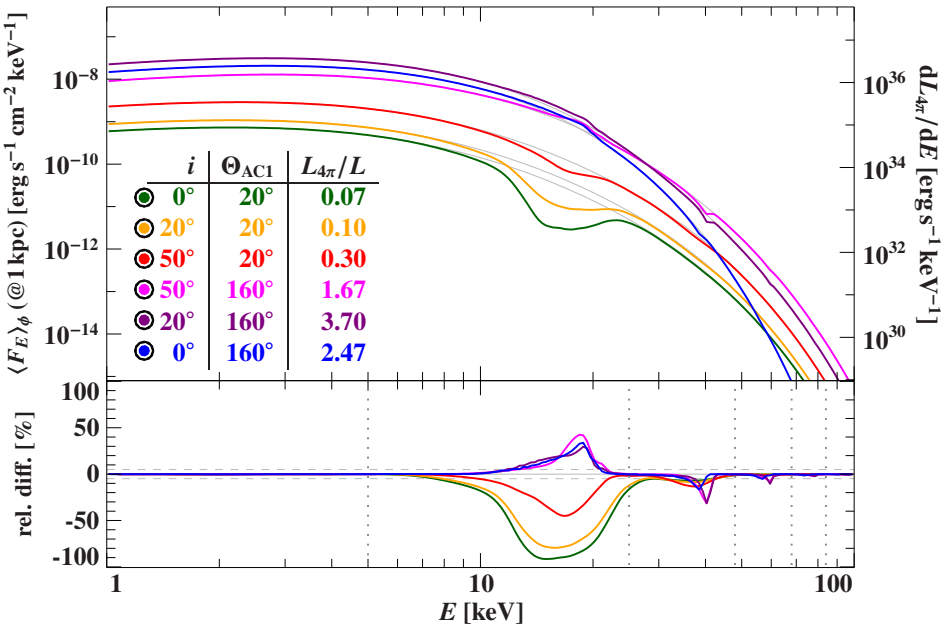

Figure 3.9.: Phase-averaged spectra of a single accretion column in the observer frame. Each spectrum corresponds to a different setup (i, Θ_{AC}) indicated in the table inset. Gray solid lines correspond to the case without CRSFs. The bottom panel shows the relative difference of the spectra to their pure continuum contribution, where horizontal gray dashed lines mark ±5%. CRSFs energy ranges are indicated with the vertical gray dotted lines.

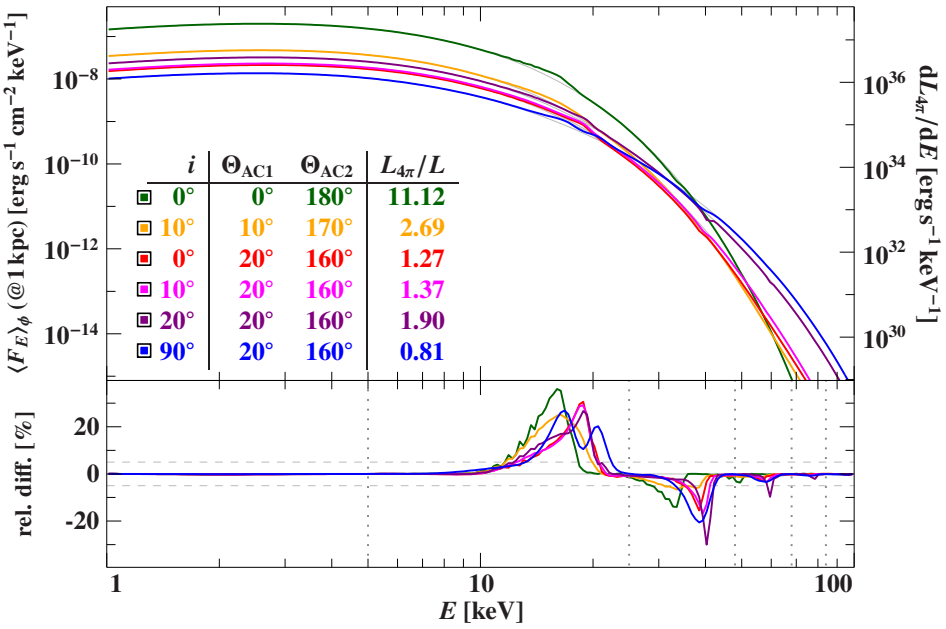

Figure 3.10.: Same as Fig. 3.9, but for two antipodal columns.

3.2.3 Bolometric pulse profiles

Figure 3.11 shows shapes of observed bolometric pulse profiles for various antipodal setups of two columns seen under different inclinations. We define the bolometric pulse profile to be

$$F(\phi) = \int_{1\,\mathrm{keV}}^{100\,\mathrm{keV}} F_E(\phi)\,\mathrm{d}E \tag{3.19}$$

and use the normalization given by

$$\tilde{F}_E = \frac{F_E - \langle F_E \rangle_\phi}{\sigma_{F_E}} \quad \text{or} \quad \tilde{F} = \frac{F - \langle F \rangle_\phi}{\sigma_F} \quad , \tag{3.20}$$

subtracting the phase-averaged flux, and dividing by the standard deviation σ_{F_E}. This normalization emphasizes the shape of the pulse profile and makes the line shapes comparable.

A large range of shapes can be distinguished, from one-peak sinusoidal over broad plateaus to two-peaked sinusoidal. Common to all profiles is their axis-symmetry with respect to $\phi = 0$ and 0.5, which is a result of the antipodal setup. Note that observed pulse profiles mostly are asymmetrical (see any reference listed in Fig. 1.10), which most likely is predominantly caused by an asymmetric configuration of the accretion columns. Figure 3.21 shows examples of asymmetric pulse profiles, which are the result of asymmetric positioned accretion columns.

Noticeable are the narrow but prominent peaks in the pulse profiles shown in Fig. 3.11. These peaks are related to the effect of strong light bending visualized in Fig. 3.12. This Figure shows the relativistic projection of a neutron star with two antipodal accretion columns onto the observer's sky (see Fig. 2.1) in comparison with the geometrical projection at different phases. Phase $\phi = 0$ shows a special configuration, in which the column on the opposite side of the neutron star is projected as an Einstein ring (Einstein, 1936), allowing the observer to see the complete circumference of the column at once. The resulting increase of the observable area yields in the narrow peaks in the pulse profiles seen in Fig. 3.11. Comparing the geometric projection to the relativistic projection in Fig. 3.12, it is noticeable that the second accretion column is only visible for $\phi = 0.4$ in the geometrical case, whereas it is the prominent, more luminous one in all phases in the relativistic case.

3.2.4 Shadowing and strong light bending

In the previous section we already have seen that in curved space-time peculiar features in the observed pulse profiles can occur. In the following we look at the reason behind this occurrence in more detail.

Depending on their visibility, we can divide the vicinity of the neutron star into three regions as shown in Fig. 3.13. First, there is the normal region which covers mostly the area in front of the neutron star and includes only those photon trajectories with one possibility to reach the observer. In other words, for each point within this region there is a unique photon trajectory. Second is the small shadow region on the far side of the neutron star, directly above the surface hidden from view. This shadow region transitions into the third region, the region of strong light bending in which each point possesses two possible trajectories reaching the observer. This region is a result of the strongly curved space-time in the vicinity of the neutron star. The transition of the emitting region, i.e., the accretion column, between those regions

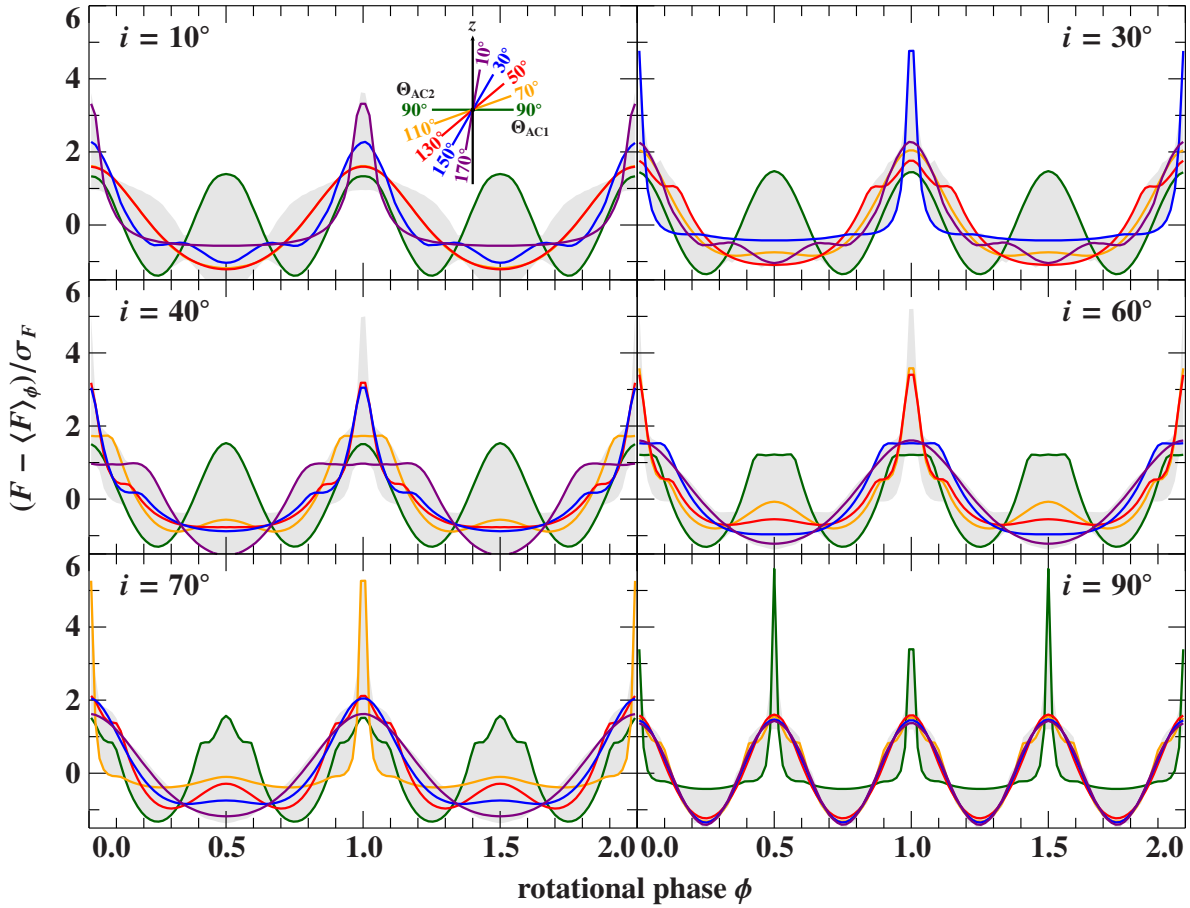

Figure 3.11.: Energy integrated normalized pulse profiles for different antipodal two-column geometries. Each panel shows a different observer inclination i for different B-field inclinations $\Theta_{\mathrm{AC1/2}}$ indicated with different colors in the upper left panel. The gray band represents the contour, in which the pulse profiles vary at the shown inclination.

over the neutron star's rotational phase causes significant changes in the observables. In the following we quantitatively describe the boundary of these regions. Combining the analytical approximation Eq. (2.16) with Eq. (2.6) the height of the shadow above the neutron star's surface can be written as

$$h_{\mathrm{S}}(\Psi) = \frac{2\left(\frac{b_{\mathrm{NS}}}{R_{\mathrm{s}}}\right)^2 R_{\mathrm{s}}}{C_\Psi^2 + \sqrt{C_\Psi^4 - 4C_\Psi(C_\Psi - 2)\left(\frac{b_{\mathrm{NS}}}{R_{\mathrm{s}}}\right)^2}} - R_{\mathrm{NS}} \tag{3.21}$$

with

$$C_\Psi = \begin{cases} 1 - \cos(\Psi_{\mathrm{p}}) & 0^\circ \le \Psi < \Psi_{\mathrm{p}} \\ 1 - \cos(2\Psi_{\mathrm{p}} - \Psi) \quad \text{for} & \Psi_{\mathrm{p}} \le \Psi \le 180^\circ \\ C_{2\pi-\Psi} & 180^\circ < \Psi < 360^\circ \end{cases},$$

where $b_{\mathrm{NS}} = R_{\mathrm{NS}}/\sqrt{1 - R_{\mathrm{s}}/R_{\mathrm{NS}}}$ is the impact parameter of the neutron star, and $\Psi_{\mathrm{p}} = \arccos(1 - 1/(1 - R_{\mathrm{s}}/R_{\mathrm{NS}}))$ is the polar angle at the periastron of the corresponding photon trajectory (schematic drawing in Fig. 2.1). The maximum shadow height is reached

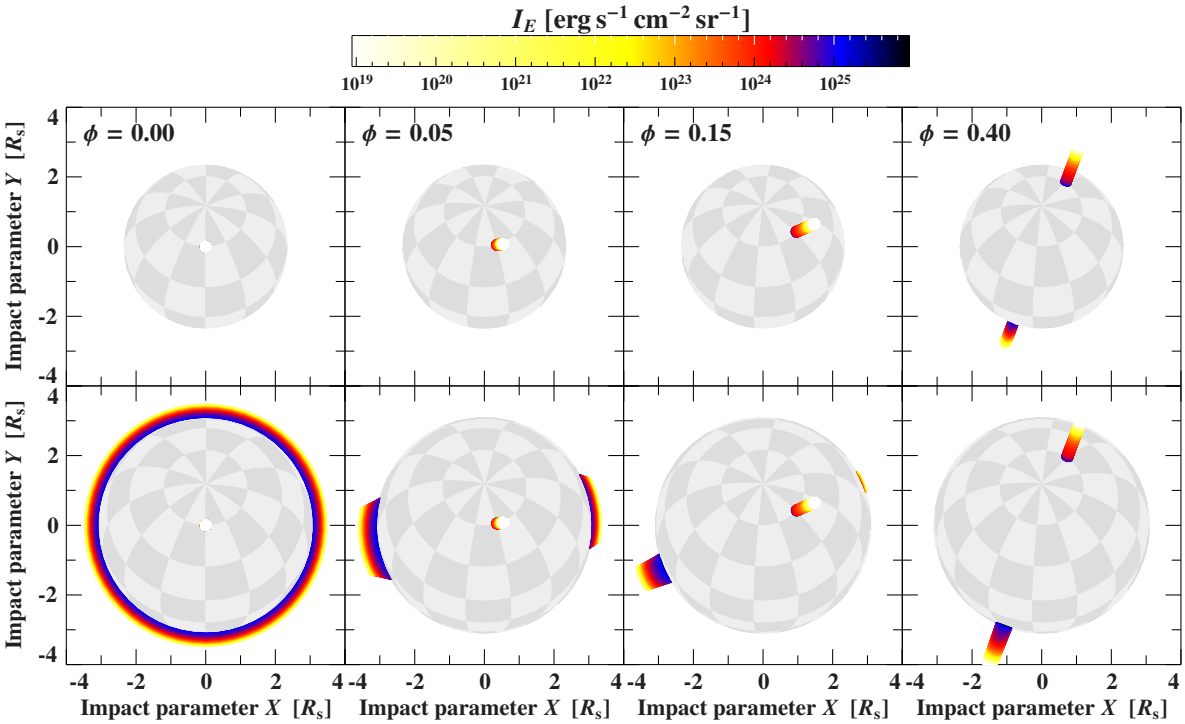

Figure 3.12.: Sky projection without (top) and with light bending (bottom). The projection is parameterized with the impact point (X, Y) (Eq. 2.17) in units of the Schwarzschild radius R_s at different rotational phases ϕ. The system is seen under $i = 30°$ and consists of two antipodal accretion columns, with $\Theta_{AC1} = 30$ and $\Theta_{AC2} = 150°$, and $\Phi_{AC1} = 0$ and $\Phi_{AC2} = 180°$. The color represents the intensity I_E (Eq. 2.26) in the rest frame of the observer.

for $\Psi = 180°$ directly on the opposite side of the neutron star along the line of sight, i.e., $h_S^{max} = h_S(180°)$. For our setup (Table 3.1) featuring a neutron star with a compactness $R_s/R_{NS} = 0.43$ we get $h_S^{max} = 1291$ m. Figure 3.13 also shows how the maximum shadow height increases for decreasing compactness of the neutron star. For example, for a neutron star with a compactness of 0.3 (i.e., 14 km, 1.4 $M_\odot$) the maximum shadow height is already at 8 km above the surface. Increasing the compactness to 0.67 causes the shadow to vanish completely, i.e., $h_S(R_s/R_{NS} \geq 0.67) \equiv 0$.

Using Eq. (2.22) we can relate Ψ to the observer inclination i, the polar angle of the column Θ_{AC}, and the rotational phase ϕ. For geometries with $i + \Theta_{AC1/2} = 180°$ and phase $\phi = 180° - \Phi_{AC1/2}$ the line of sight is aligned with one of the B-field axes, i.e., the column is centered around $\Psi = 180°$. In such cases the column is projected as a perfect Einstein ring (see Fig. 3.12), assuming that the height of the column exceeds approximately the maximum shadow height. A ring projection is possible as long as the shadow point is within the column,

$$180° - \Delta\Psi_{ring} < i + \Theta_{AC} < 180° + \Delta\Psi_{ring} \quad , \tag{3.22}$$

where

$$\Delta\Psi_{ring} \approx \arctan\left(\frac{r_{AC}}{R_{NS} + h_S^{max}}\right) \quad . \tag{3.23}$$

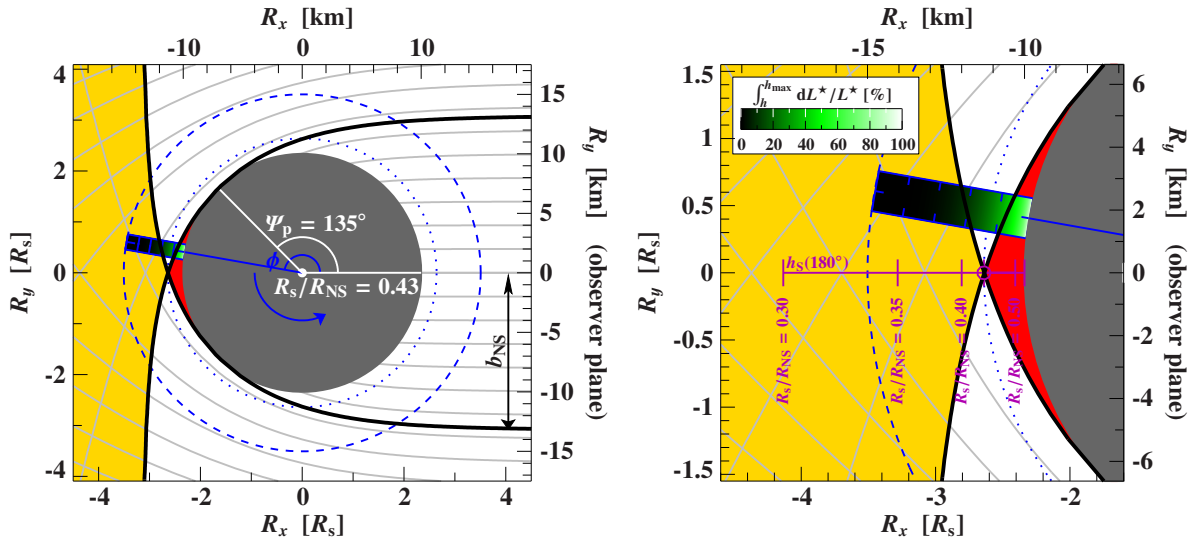

Figure 3.13.: Regions of visibility. **Left:** The regions are divided by the boundary trajectory (black solid line), touching the neutron star (gray) in the periastron of the trajectory at the polar angle Ψ_p. Gray lines represent a grid of possible trajectories to the observer at infinity to the right. For points in the red, white, and yellow region there are no, one, or two possible trajectories reaching the observer, respectively. The blue rectangle indicates the accretion column ($r_{AC} = 647\,\mathrm{m}$, $h_{max} = 5\,\mathrm{km}$) where its cumulative intrinsic luminosity, $\int_h^{h_{max}} dL^\star/L^\star$, is color coded (see right panel). The tic marks are separated by 1 km. The dashed and dotted blue line show the path of the accretion column around the neutron star at height h_{max} and $h_S(180°)$, respectively. The geometry is chosen such that the column rotates around the z-axis in the x-y-plane, i.e., $i = \Theta_{AC} = 90°$. **Right:** Zoom-in on the shadow region. The purple circle marks the maximum height of the shadow, $h_S(180°) = 1291\,\mathrm{m}$, above the neutron star's surface. The evolution of this shadow height for neutron stars of different compactnesses is indicated by the purple markers.

Further, the column is only passing through or within the shadow region if

$$\Psi_p + \Delta\Psi_{AC} < i + \Theta_{AC} < 360° - \Psi_p - \Delta\Psi_{AC} \quad , \tag{3.24}$$

where Ψ_p relates to the periastron and $\Delta\Psi_{AC} = \arctan(r_{AC}/R_{NS})$ is the the half opening angle of accretion column at its base. For our setup (Table 3.1) we get $\Delta\Psi_{ring} = 3.^\circ3$, $\Psi_p = 135°$ and $\Delta\Psi_{AC} = 4.^\circ7$. The small value of $\Delta\Psi_{ring}$ translates into a very narrow range in phase in which the Einstein ring is visible. Furthermore, as $\Delta\Psi_{AC}$ is also small, there are only few geometries for which this effect can even occur.

3.2.5 Dependency on geometry

In the previous sections we have shown that the observed, phase and energy dependent flux strongly depends on the geometry, i.e., on i and $\Theta_{AC1/2}$, for selected examples. In the following we investigate this dependency of our results on the geometry in more detail.

3.2.5.1 Energy- and phase-resolved flux

The energy- and phase-resolved flux, $F_E(\phi)$, is dominated by the spectral shape of the continuum. To enhance changes with phase and energy we use the normalization in Eq. (3.20) as presented in Fig. 3.14 (one column) and investigate how these columns look like in several different geometric setups. For most geometries the pulse profile is broad and single peaked and does not vary much with energy. The only visible deviations are in a small band around the CRSF energies. Spectral changes, that is variations with energy at a given phase, are also limited to the CRSF energies. The variability is much higher, however, in cases in which the column passes through the shadow region, i.e., when the column fulfills the condition of Eq. (3.24). For these parameters the pulse profiles evolve in general from single peaked at low energies to double peaked at high energies. The details of this evolution strongly depend on the geometry. In regions where only one peak is seen, the spectra are softer than the phase-averaged spectrum, while the spectral shape is harder when double peaked pulses are present. The antipodal two-column geometry in Fig. 3.15 shows the same general behavior, but with more complexity due to the mixed contribution of the two columns. Note the symmetry of the energy-phase maps in the antipodal two-column scenario. For example, the maps in the bottom left and the bottom right panel in Fig. 3.15 are identical, but shifted by half a rotational phase. This symmetry is explained by the similarity of the corresponding geometries, where basically only the polar angles of the columns are swapped, i.e., $\Theta_{\mathrm{AC1}} \leftrightarrow \Theta_{\mathrm{AC2}}$, while the difference in their azimuthal position is 180°.

The strong dependency of the CRSFs on the angle to magnetic field, η' (Fig. 3.6), explains the variations at the CRSF energies as different phases are related to different emission angles. The large scale variations with respect to energy, however, result from the column moving through the shadow region and the region of strong light bending (see Fig. 3.13) in combination with the properties of the columns emission profile. In particular the line of the sight to the bottommost and therefore hottest part of the column is blocked (see Eq. 3.2 and Fig. 3.5). As the temperature determines the exponential cutoff (Eq. 3.1) and therefore the spectral hardness, this effect strongly influences the observed spectrum. The observed spectrum softens the further the column is in the shadow region, while the observed luminosity increases as a result of strong light bending magnifying the upper part of the column. That means here the light bending is able to compensate for the decrease of the emissivity with height.

We note that the relation between the compactness of the neutron star, $R_{\mathrm{NS}}/R_{\mathrm{s}}$, and the height of the columns plays an important role. A detailed discussion of the impact of the compactness on the observables, however, is beyond the scope of this thesis. As long as the emissivity of the column is sufficiently above the maximum shadow height, $h_{\mathrm{S}}^{\mathrm{max}}$, the effect of strong light bending is observable as an enhancement in the flux. Otherwise, there will be a reduction of the observed flux.

3.2.5.2 Flux derived and bolometric luminosity

In Sect. 3.2.1 we defined the flux derived luminosity, $L_{4\pi}$, and the bolometric luminosity, L. Figure 3.16 shows the anisotropy factor of the flux derived luminosity, $L_{4\pi}/L$, and its dependency on the geometry. If only one accretion column is present, the anisotropy factor varies over several orders of magnitude. Looking directly into the column from above ($i = 0°$,

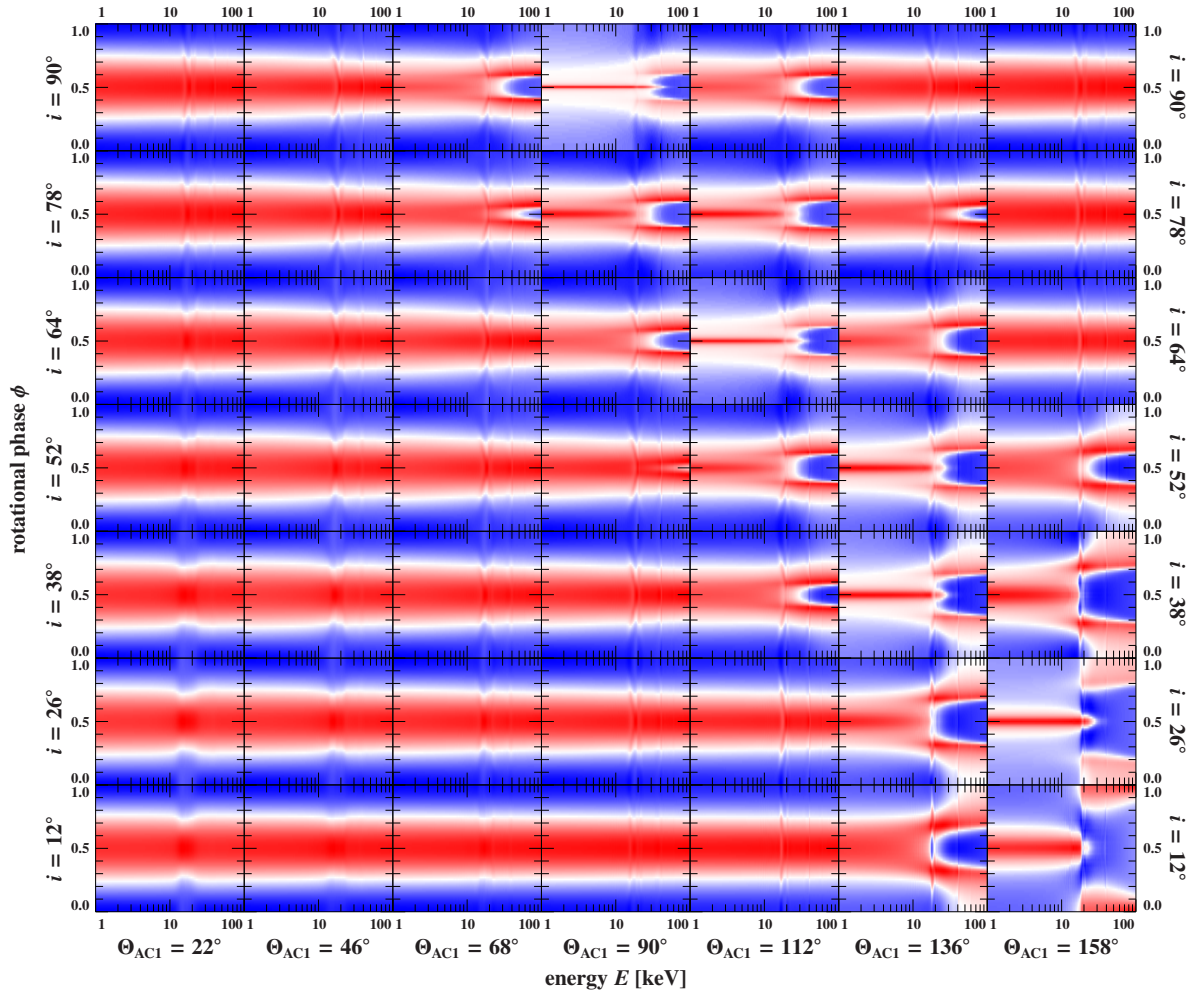

Figure 3.14.: Normalized observed phase and energy dependent flux, $\tilde{F}_E(\phi)$ (see Eq. 3.20), for different single column geometries (i, Θ_{AC1}). In each panel the color-scale is such that white corresponds to $\tilde{F}_E(\phi) = 0$, blue to $\tilde{F}_E(\phi) < 0$, and red to $\tilde{F}_E(\phi) > 0$. Note that the minimum and maximum values may differ between the individual panels.

$\Theta_{AC1} = 0°$) the luminosity is underestimated by a factor of 10^3, while it is overestimated by a factor of 22 when the column is constantly on the opposite side ($i = 0°$, $\Theta_{AC1} = 180°$). Figure 3.16 also shows that the enhancement in luminosity occurs for geometries where $i + \Theta_{AC1,2} \approx 180°$. The enhancement in the flux derived luminosity is due to the high visibility caused by strong light bending (Fig. 3.13), while the column is projected twice or even as ring (Fig. 3.12). For two antipodal columns, however, the anisotropy factor ranges only from 0.8 to 11 as the second column compensates the extreme amplitudes present when only one column is considered. Nevertheless, even in the case of two columns there is a significant systematic error for the flux derived luminosity. It is impossible to determine this systematic error without knowing the physical parameters of the system. Finally, note that the flux derived luminosity increases significantly even though that the bottom, most luminous parts of the column are in the shadow region (Fig. 3.13).

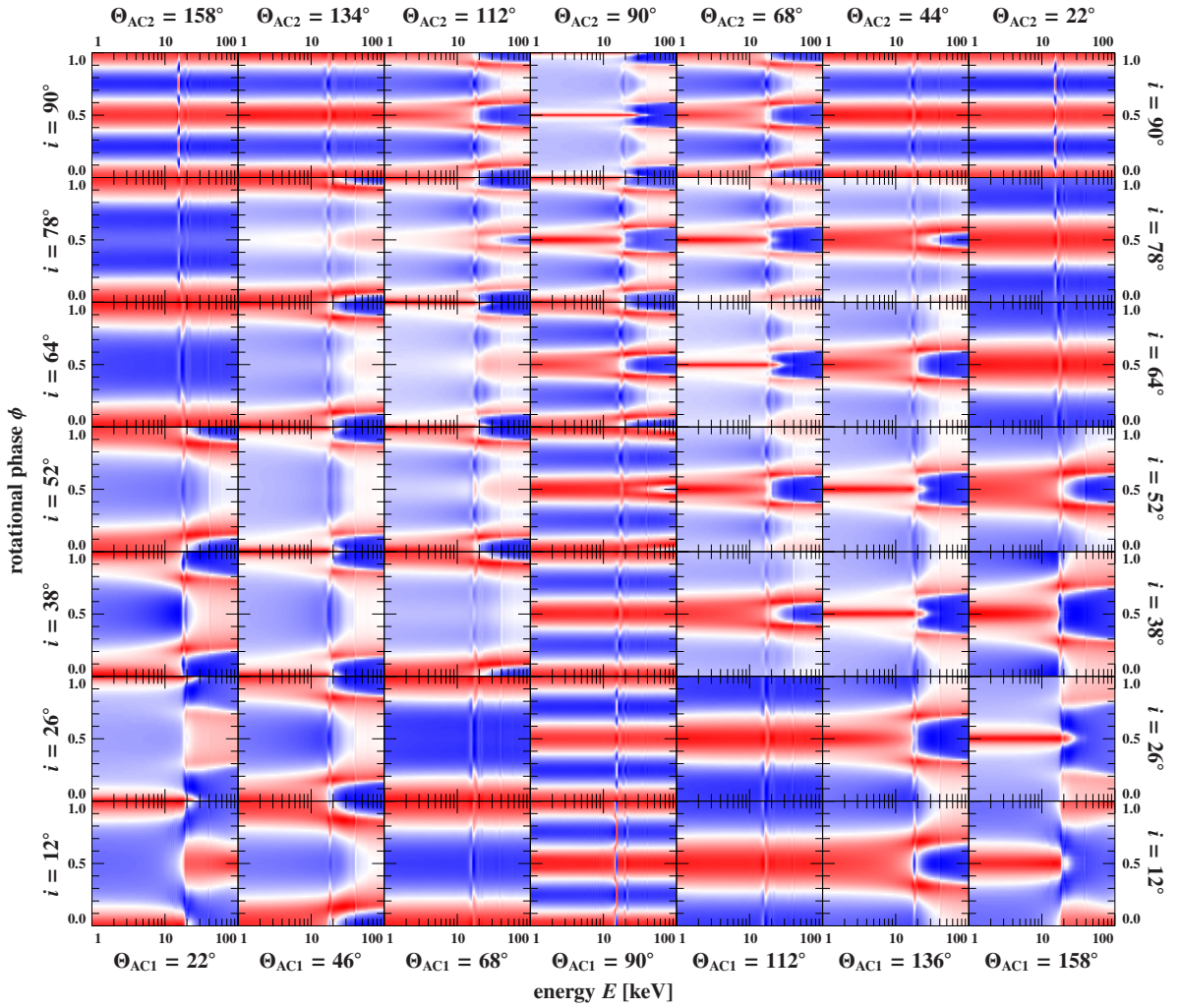

Figure 3.15.: Normalized observed phase and energy dependent flux, $\tilde{F}_E(\phi)$ (see Eq. 3.20). Same as in Fig. 3.14, but for different antipodal column geometries (i, $\Theta_{\rm AC1,2}$).

An additional effect that complicates the behavior of the flux derived luminosity is the strong Doppler boosting in the column. This boosting shifts the maximum of the emitted flux to larger angles and therefore most of column's emission is directed downwards (Fig. 3.5). In combination with the fact that the observable emission angle, $\eta^\star$, increases with the polar angle Ψ (Fig. 3.13), very large flux derived luminosities become possible. Using our example parameters (Table 3.1), Eq. (3.13) gives maximum observable emission angles $\eta^\star_{\rm max}(1\,{\rm km}) = 110°$ and $\eta^\star_{\rm max}(5\,{\rm km}) = 132°$, while the intrinsic luminosity emitted from the column, $\mathrm{d}L^\star/\,\mathrm{d}\mu^\star$, peaks at $\eta^\star = 131°$. In other words, for the present setup the directions of the peak emissivity coincide with those viewing angles strongest effected by the boosting of light bending.

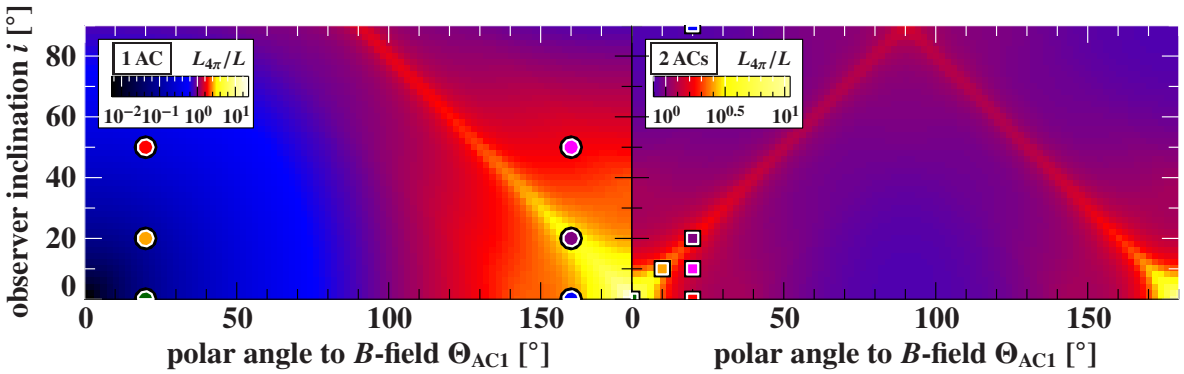

Figure 3.16.: Anisotropy of the flux derived luminosity. Flux derived luminosity, $L_{4\pi}$ (Eq. 3.16), dependent on the geometry i and Θ_{AC} in units of the bolometric luminosity, L (Eq. 3.14). **Left**: Case of one accretion column. **Right**: Case of two antipodal accretion columns. The colored markers correspond to the geometrical cases of the observed spectra shown in Fig. 3.9 (left) and Fig. 3.10 (right), respectively.

3.2.5.3 Pulsed fraction

A simple measure for the variability of the observed flux, F, with the rotational phase is the pulsed fraction,

$$\delta F = \frac{\max(F) - \min(F)}{\max(F) + \min(F)} \quad . \tag{3.25}$$

This simple parameter encodes information about the underlying geometry as shown in Fig. 3.17. In the single-column geometry the pulsed fraction peaks for geometries $i + \Theta_{AC1} \approx 180°$ and $i \approx \Theta_{AC1}$ for $\Theta_{AC1} > 90°$ and $\Theta_{AC1} < 90°$, respectively. In the first case the high pulsed fraction is the result of the prominent narrow peaks caused by strong light bending (Fig. 3.11). In the latter case at certain phases the column is seen directly from above. This line of sight results in a deep dip in the pulse profile, which increases also the pulsed fraction.

In the two-column geometry, however, the column which is mostly in the back is always brighter than the column that is in front (Fig. 3.16), such that the front column contributes little to the pulsed fraction. In other words, the pulsed fraction is dominated by peaks caused by strong light bending when one of the columns is on the opposite side of the neutron star, that is $i + \Theta_{AC1,2} \approx 180°$.

3.2.5.4 Continuum

We next study how the continuum shape influences the observations. We use a simple empirical model to describe the general behavior of the continuum. In particular we us a power law with a high energy exponential cutoff, `CutoffPL` (Eq. 1.11). Comparing the energy dependency of the `CutoffPL` to that in Eq. (3.1), we see that the folding energy corresponds to the (average) plasma temperature, that is $E^{\star}_{\rm fold} \approx kT$. Although Eq. (3.1) implies a photon index of $\Gamma^{\star} = 0$, we expect the index to be softer as we look at height and angle integrated spectra which mix

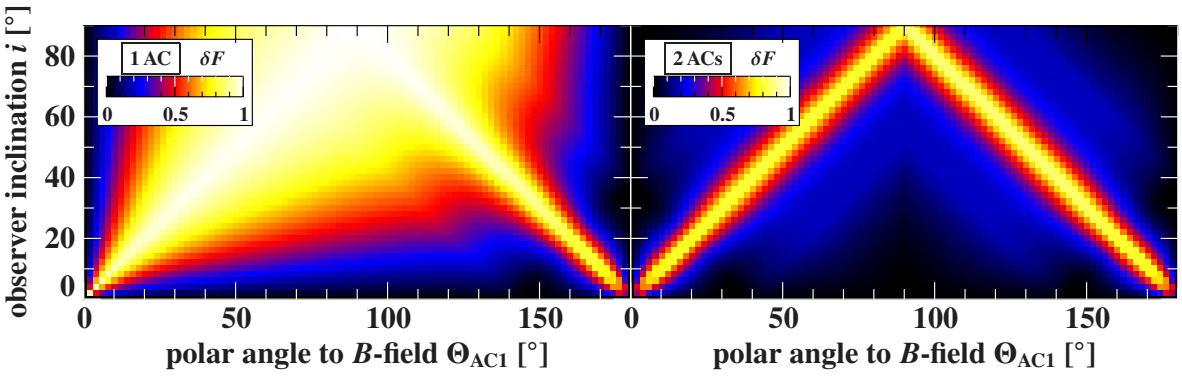

Figure 3.17.: Pulsed fraction of energy integrated pulse profiles. **Left**: Case of one accretion column. **Right**: Case of two antipodal accretion columns.

different plasma temperatures and boosting factors in the intrinsic frame. Furthermore, the height dependent gravitational redshift will soften the observed spectra.

We fit Eq. (1.11) to the intrinsic height- and angle-integrated continuum emitted by the accretion column, $\mathrm{d}L^\star / \mathrm{d}E^\star$, as well as to the phase-averaged observed continuum for different geometries, $\langle F_E \rangle_\phi \, (i, \Theta_{AC})$, in the energy range from 1 keV to 100 keV. For the parameters in Table 3.1 the intrinsic height- and angle-integrated continuum of the single column is well described by $\Gamma^\star = 0.23$ and $E^\star_{\mathrm{fold}} = 5.2\,\mathrm{keV}$. As expected this folding energy is approximately the plasma temperature at the height at which the emission is at a maximum (Figs. 3.5 and 3.8). The plasma temperature itself increases from 0.3 keV at a height of 5 km to 9.2 keV at the bottom of the column.

In the top panel of Fig. 3.18 we show the photon index of the phase-averaged continua and the dependency of the spectral shape on i and $\Theta_{AC1,2}$ for one and two antipodal columns, respectively. Quantities derived from the phase-averaged flux are denoted by an overline[6]. $\overline{\Gamma}$ ranges from 0.09 to 0.34 for one and from 0.09 to 0.27 for two columns. In both cases $\overline{\Gamma}$ decreases the closer the geometry is to $i + \Theta_{AC1,2} = 180°$. Additionally, the contour lines in Fig. 3.18 indicate the variability of the photon index with respect to pulse phase. These contours represent the phase amplitude at different levels relative to the maximum phase amplitude, A. Phase amplitude denotes the difference between the maximum and minimum value as function of pulse phase for a given parameter and geometry. The maximum phase amplitude then gives the maximum of these phase amplitudes occurring for all geometries [7]. The maximum phase variability is reached for geometries close to $i + \Theta_{AC1,2} = 180°$, where the maximum phase amplitude of the photon index is 0.24 and 0.17 in the case of one and two columns, respectively.

[6]For example, $\overline{\Gamma}$ corresponds to the photon index obtained from the phase-averaged spectrum, $\langle F_E \rangle_\phi$, and is defined as $\overline{\Gamma} = \Gamma(\langle F_E \rangle_\phi)$. This parameter should not be confused with the phase-averaged photon index, $\langle \Gamma \rangle_\phi$, which is obtained by averaging the photon indices of the phase-resolved spectra and using the bracket-notation in Eq. (3.17) would be written as $\langle \Gamma \rangle_\phi = \int_0^{2\pi} \Gamma(F_E(\phi))\, \mathrm{d}\phi / 2\pi$. These two definitions are fundamentally different, i.e., $\overline{\Gamma} \neq \langle \Gamma \rangle_\phi$.

[7]For example, the maximum phase amplitude of the photon index is given by $A_\Gamma = \max_{i,\Theta_{AC}} \left\{ \max_\phi \left[\Gamma\left(F_E(\phi)|_{i,\Theta_{AC}} \right) \right] - \min_\phi \left[\Gamma\left(F_E(\phi)|_{i,\Theta_{AC}} \right) \right] \right\}$, where $F_E(\phi)|_{i,\Theta_{AC}}$ is the energy- and phase-resolved flux observed for i and Θ_{AC}.

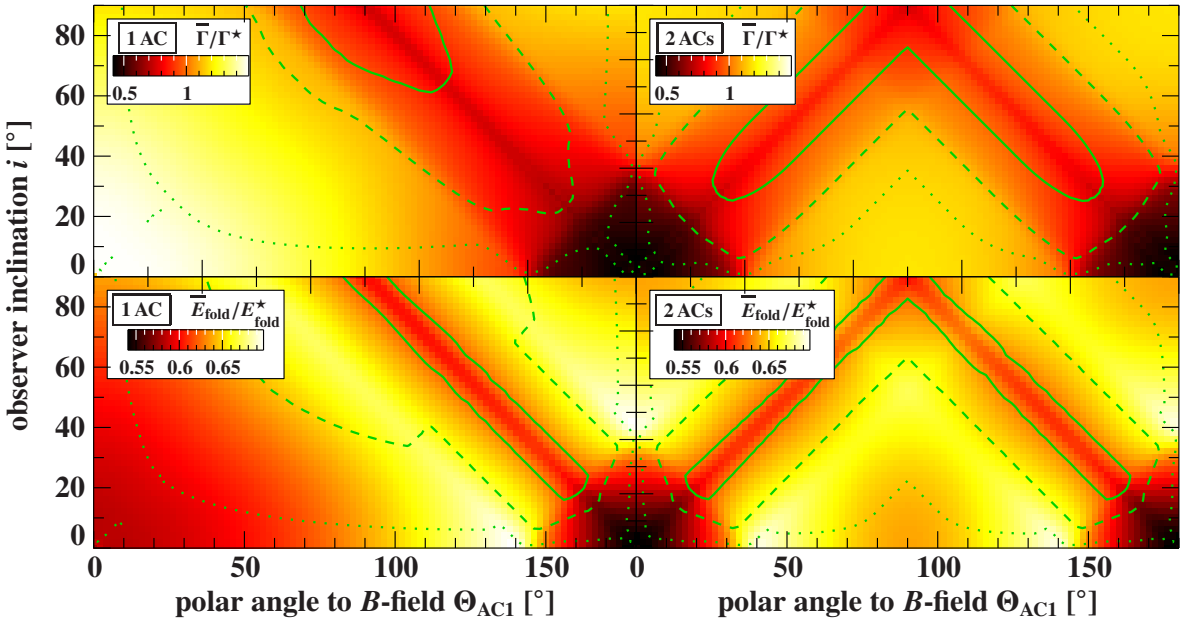

Figure 3.18.: Dependency of the continuum on the geometry i and $\Theta_{\rm AC}$. The photon index $\overline{\Gamma}$ (**top**) and folding energy $\overline{E}_{\rm fold}$ (**bottom**) are the `CutoffPL` parameters fitted to the phase averaged spectra in units of $\Gamma^\star = 0.23$ and $E^\star_{\rm fold} = 5.2\,\mathrm{keV}$, respectively. The solid, dashed and dotted green lines represent the contours of the amplitudes within the phase-resolved spectra at levels 90%, 50% and 10%, respectively, in units of the maximum phase amplitude A. **Left** panels correspond to the case of a single column with $A_\Gamma = 0.24$ and $A_{E_{\rm fold}} = 0.81\,\mathrm{keV}$. Panels on the **right** correspond to the case of two antipodal columns with $A_\Gamma = 0.17$ and $A_{E_{\rm fold}} = 0.81\,\mathrm{keV}$ (see Table 3.2).

Figure 3.18 also shows how the folding energy of the phase-averaged continua varies with the polar angle of magnetic field and inclination. The mean folding energy, $\overline{E}_{\rm fold}$, first increases as $i + \Theta_{\rm AC1,2}$ approaches 180°. Once the geometry is such that the hotter bottom parts of the column are within the shadow region a significantly long part of the rotational phase the mean folding energy decreases again. In both, the single and the antipodal two-column case, $\overline{E}_{\rm fold}$ ranges from 2.8 keV to 3.6 keV. The maximum amplitude with respect to the rotational phase is 0.81 keV in both cases. Note that the values of $\overline{E}_{\rm fold}$ are significantly lower than $E^\star_{\rm fold}$, which is due to the gravitational redshift (Eq. 2.27).

3.2.5.5 CRSFs

In Figs. 3.9 and 3.10 we see that the shape, width, depth, and position of the CRSFs also strongly depend on the geometry. It is surprising and contrary to observations that for many geometries the fundamental CRSF is in emission, especially in the case of two accretion columns.

The large variety of shapes of the fundamental CRSF prevents comparing it with a simple model, such as `gabs` or `cyclabs`. To investigate the dependency of fundamental CRSF on the

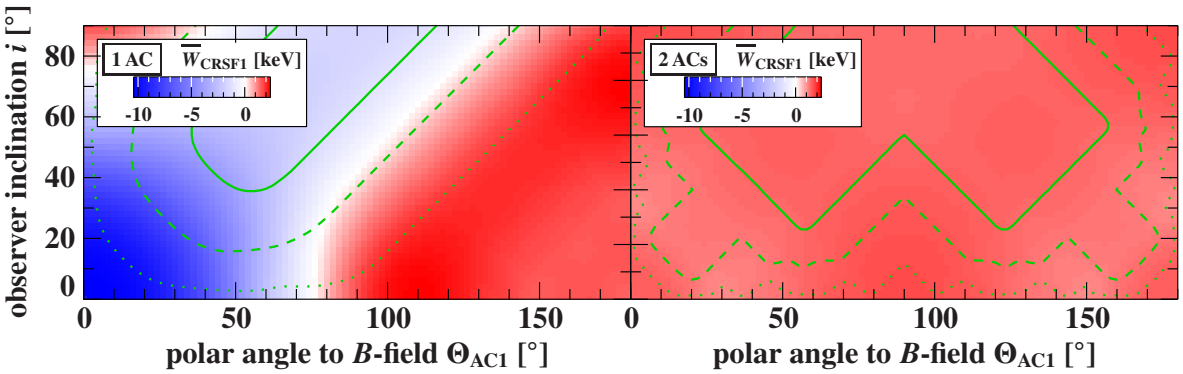

Figure 3.19.: Phase-averaged equivalent width of the fundamental CRSF, $\overline{W}_{\mathrm{CRSF0}}$, in the energy range from 5 keV to 25 keV. The solid, dashed and dotted green lines represent the contours of the amplitudes with respect to phase at levels 90%, 50% and 10%, respectively, in units of the maximum phase amplitude, A_W. Where A_W = 12.8 keV in the case of one accretion column (**left**) and A_W = 0.6 keV in the case of two antipodal columns (**right**).

geometry in Fig. 3.19 we therefore use the 5–25 keV equivalent width,

$$W = \int_{E_{\mathrm{lo}}}^{E_{\mathrm{hi}}} \frac{F_E - \mathcal{F}_E}{\mathcal{F}_E}\,\mathrm{d}E \quad \text{and} \quad \overline{W} = \int_{E_{\mathrm{lo}}}^{E_{\mathrm{hi}}} \frac{\langle F_E\rangle_\phi - \langle \mathcal{F}_E\rangle_\phi}{\langle \mathcal{F}_E\rangle_\phi}\,\mathrm{d}E \quad . \tag{3.26}$$

In Eq. (3.26), $\mathcal{F}_E$ is the observed flux without CRSFs, that is using $\mathcal{I}_E$ (Eq. 3.1) instead of I_E (Eq. 3.10). Obviously there is a huge difference between the one and two column setup showing very strong and no CRSF in absorption, respectively. For one accretion column we see the CRSF in absorption for geometries along $\Theta_{\mathrm{AC1}} \approx i$. Along this angle equality are phases which allow us to observe the accretion column from above, that is with a rather small angle to the magnetic field ($\lesssim 45°$; see Fig. 3.6). For the test setup (Table 3.1), the minimum and maximum equivalent width are −10.4 keV and 2.4 keV, respectively. Adding a second, roughly antipodal column, however, causes the fundamental line to be in emission for all geometries. The reason for this change is that the column in the back which shows the fundamental in emission outshines the front column (see Fig. 3.16). The resulting equivalent width in the two-column case is in a small range from 1.1 keV to 1.7 keV.

The phase variability is also much smaller in the case of the two antipodal columns than in the case of one, with a maximum phase amplitude, A_W, of 0.6 keV and 12.8 keV, respectively. That the phase amplitude is smaller than average equivalent width means that for two columns even in the phase-resolved case the fundamental CRSF is never observed in absorption.

To get a better understanding for this behavior we look again at Fig. 3.8, which shows the strength of the fundamental CRSF with respect to the continuum in the rest frame of the emitter. We define this line strength as

$$S' = 2\pi r_{\mathrm{AC}} \int_{E'_{\mathrm{lo}}}^{E'_{\mathrm{hi}}} \int_{-\pi/2}^{\pi/2} (I'_{E'} - \mathcal{I}'_{E'})\,\mathrm{d}\eta_{\mathrm{S}}\,\mathrm{d}E' \quad . \tag{3.27}$$

Besides the decrease of the line strength with height due to the decrease of the overall emissivity, we see that for $45° < \eta' < 135°$ the fundamental CRSF is in emission. It is in

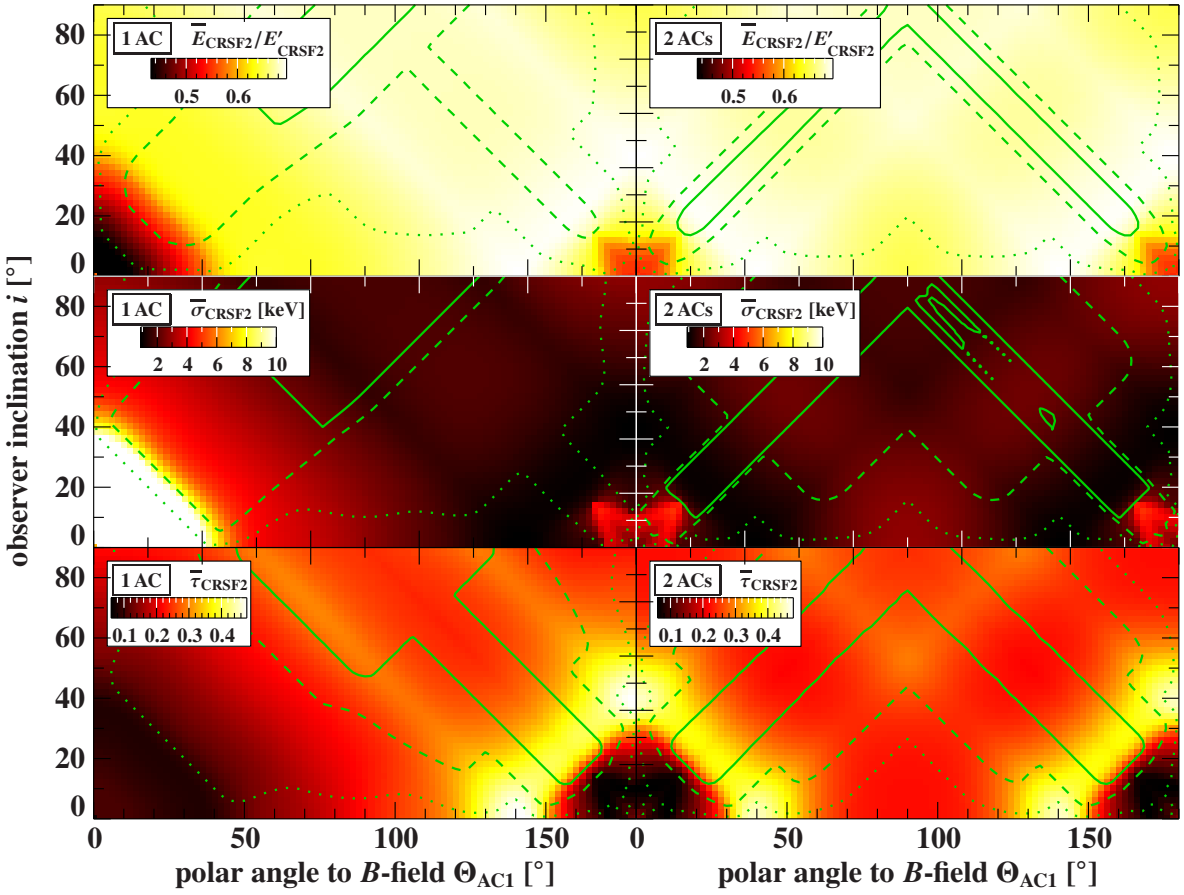

Figure 3.20.: Dependency of the first harmonic CRSF on the geometry i and $\Theta_{\rm AC}$. The line energy $\overline{E}_{\rm CRSF2}$ (**top**), width $\overline{\sigma}_{\rm CRSF2}$ (**middle**) and optical depth $\overline{\tau}_{\rm CRSF2}$ (**bottom**) are the `gabs` parameters fitted to the phase-averaged spectra in the energy range from 25 keV to 48 keV. The observed line energy is given in units of the intrinsic line energy $E'_{\rm CRSF2} = 58$ keV. The solid, dashed and dotted green lines represent the contours of the amplitudes within the phase-resolved spectra at levels 90%, 50% and 10%, respectively, in units of the maximum phase amplitude A. **Left** panels correspond to the case of a single column with $A_{E_{\rm CRSF2}} = 15$ keV, $A_{\sigma_{\rm CRSF2}} = 9.1$ keV and $A_{\tau_{\rm CRSF2}} = 0.42$. Panels on the **right** to the case of two antipodal columns with $A_{E_{\rm CRSF2}} = 9$ keV, $A_{\sigma_{\rm CRSF2}} = 3.2$ keV and $A_{\tau_{\rm CRSF2}} = 0.39$ (see Table 3.2).

absorption only for $\eta' > 135°$ and $\eta' < 45°$, that is for small angles with respect to the magnetic field.

Although the absolute value of the line strength is stronger in absorption than in emission, there are several conditions causing the observed fundamental line to be most prominent in emission. Firstly, the specific intensity of the column is a fan beam configuration which is proportional to $\sin\eta'$ (Eq. 3.1) with peak emissivity perpendicular to the magnetic field, i.e., $\eta' = 0°$. Secondly, the solid angle in which the line is visible in emission is much larger than for the absorption. Furthermore the light bending also increases the observed flux for those angles the line is in emission.

Contrary to the fundamental CRSF, its harmonics are always observed in absorption (Figs. 3.9 and 3.10). Their shape is clearly asymmetric and has a shallow extended lower energy flank. Nevertheless, the harmonic lines are well approximated by a Gaussian absorption line, which is not the case for the fundamental CRSF. We parameterize the shape of the harmonic CRSFs using the `gabs` model (Eq. 1.16).[8] Figure 3.20 shows how the first harmonic depends on the geometry. As expected from Eq. (3.18) the line energy is gravitationally redshifted. The energy varies with phase due to the variation of the viewing angle to the magnetic field and the related change of the boosting factor. In the single column case the line energy of the first harmonic varies between 25 keV and 40 keV. In addition, with a maximum phase amplitude of 15 keV the amplitude is quite large, corresponding to a variation of 43% around the average line energy. Adding the second antipodal column reduces the range in which the line energy of the first harmonic varies. The minimum line energy is increased to a value of 32 keV in the phase-averaged spectra and the phase amplitude is cut in half. Throughout the different geometrical configurations the width of the harmonic is anti-correlated to its energy. This anti-correlation is caused by to independent circumstances which, however, both are related to the viewing angle. The variation of line energy is due to angle dependent boosting factor in Eq. (3.18), while the angle dependency of the CRSF cross sections is responsible for the change of the line width (e.g., Schwarm et al., 2017b). In other words, assuming a bulk velocity of zero the line energy would not vary for different geometries but the line width would still the same geometry dependency.[9] The appearance of the line varies from narrow to very broad in a range of 0.9–10.0 keV, while the second column reduces the maximum width down to 4.9 keV. The same is true for the phase amplitude of the line width, which is reduced from 9.1 keV to 3.2 keV. This reduction of variability of the line energy and width by the second column seems to affect the optical depth of the harmonic only marginally. In both cases considered here the optical depth is in a similar range of 0.06–0.48 and has a phase amplitude of 0.42. Further there is also a clear anti-correlation between the width and optical depth of the CRSF, which is predicted by theory (e.g., Schwarm et al., 2017a,b). In particular, the lines are predicted to be wide and shallow for small viewing angles with respect to the B-field, while they are narrow and deep for viewing angles approximately perpendicular to the B-field.

The higher harmonics of the CRSF ($n > 2$) behave in a similar way as the first harmonic, however, the line strength reduces with increasing harmonic number n (Figs. 3.9 and 3.10). Although we are not able to parameterize the fundamental CRSF, its line energy is connected by the 12-B-12 rule (Eq. 1.9) and Eq. (3.18) to the line energy of the harmonic CRSFs. In other words, the fundamental CRSF energy also varies approximately with the same factor as the first harmonic (Fig. 3.20, top). In particular that is $\overline{E}_{\mathrm{CRSF2}}/E'_{\mathrm{CRSF2}} = 0.43$–$0.70$ for the single column and 0.55–0.70 for the antipodal columns.

[8] The `cyclabs` model for cyclotron absorption lines described the shape overall slightly worse.

[9] Note that geometries for which parts of the column are in the shadow region the line energy might still change even without bulk velocity. In that case, however, the corresponding geometry-dependency would look different.

3.2.5.6 Asymmetric accretion columns

Throughout the previous sections we presented results based on antipodal two-column configurations to avoid the additional degrees of freedom introduced by asymmetric column locations. We next turn to discussing the effects introduced by accretion columns which are not positioned antipodally for one specific asymmetric setup. For this setup we use the same displacement values for the accretion columns as Ferrigno et al. (2011), i.e., $\Delta_{\Phi_{\rm AC}} = -65°$ and $\Delta_{\Theta_{\rm AC}} = -43°$ (see Table 2.1). While we fix this relative displacement of the two columns, we also look at the dependency on i and $\Theta_{\rm AC}$ like for the previously discussed one-column and antipodal two-column setups.

The bolometric pulse profiles resulting from the asymmetric setup are shown in left panel of Fig. 3.21. The general behavior is similar to the antipodal profiles in Fig. 3.11. It is noticeable, however, that the pulse profiles in the asymmetric case are also asymmetric, which is the result of the displacement of the two columns in phase. The contribution of each individual column to the pulse profile is axis-symmetric, independent of the column's polar angle, $\Theta_{\rm AC}$.[10] An antipodal combination of these contributions conserves this axis-symmetry, while a displacement $\Delta_{\Phi_{\rm AC}} \neq 0°$ results in an asymmetric pulse profile.

The spectral characteristics for the asymmetric configuration are very similar to those of the antipodal one. In the right panel Fig. 3.21 the phase-averaged spectra are shown for some example geometries (the same as in Fig. 3.10). The general shape of the continuum and also that of the CRSFs is not significantly impacted by the asymmetric location of the accretion columns.

The top right panel in Fig. 3.22 shows the dependency of the pulsed fraction on i and $\Theta_{\rm AC}$. In comparison to the antipodal case (Fig. 3.17) we see in principle the same distribution governed by the influence of the light bending, which is strongest for $i + \Theta_{\rm AC1,2} \approx 180°$. The deviations are therefore a result of the displacement $\Delta_{\Theta_{\rm AC}}$. Looking at the geometrical dependency of the anisotropy of the flux derived luminosity in the top left panel of Fig. 3.22 we see the same shift of the pattern as for the pulsed fraction. In the case of the fundamental CRSF the asymmetry of the columns has also no effect on whether it is seen in absorption or emission. As shown in the bottom panel of Fig. 3.22 the the fundamental line is also predicted to be observed only in emission as in the antipodal case (Fig. 3.19).

Figure 3.23 shows the energy- and phase-resolved observed flux for the asymmetric columns. The flux is normalized (Eq. 3.20) such that the shape of the energy dependent pulse profiles is enhanced. In comparison to the antipodal case in Fig. 3.15 we see that there is more variety in the shapes. In most of the shown cases the pulse profiles are clearly asymmetric. Furthermore the evolution with energy appears smoother and in some cases looks similar to that observed in GS 0834−430 (see Figs. 3 and 4 in Miyasaka et al., 2013).

In conclusion we find that an asymmetric configuration of the accretion columns does not significantly change the results we presented for the antipodal two-column case. The only exception is the influence on the shape of the pulse profiles, which is caused by the displacement of the columns in phase.

[10] The reason for the symmetry in the observed phase dependent flux is the cylindrical symmetry of the accretion column and its emission pattern.

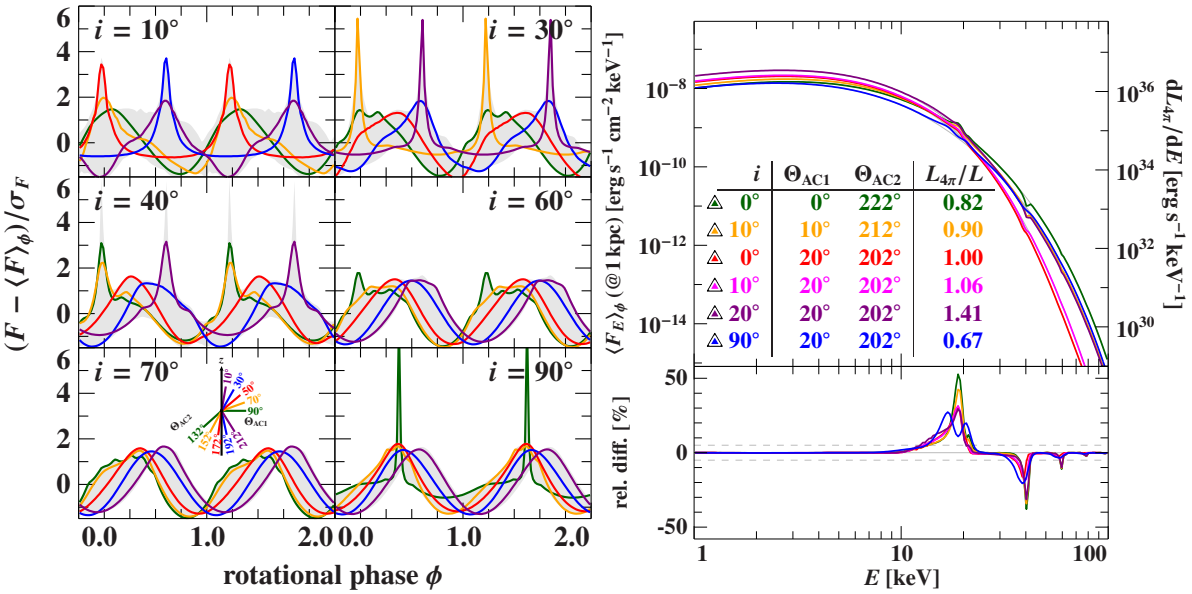

Figure 3.21.: Bolometric pulse profiles (**left**) and phase-averaged observed spectra (**right**), but for the asymmetric two-column setup (see Table 2.1). Compare Fig. 3.10 and Fig. 3.11, respectively.

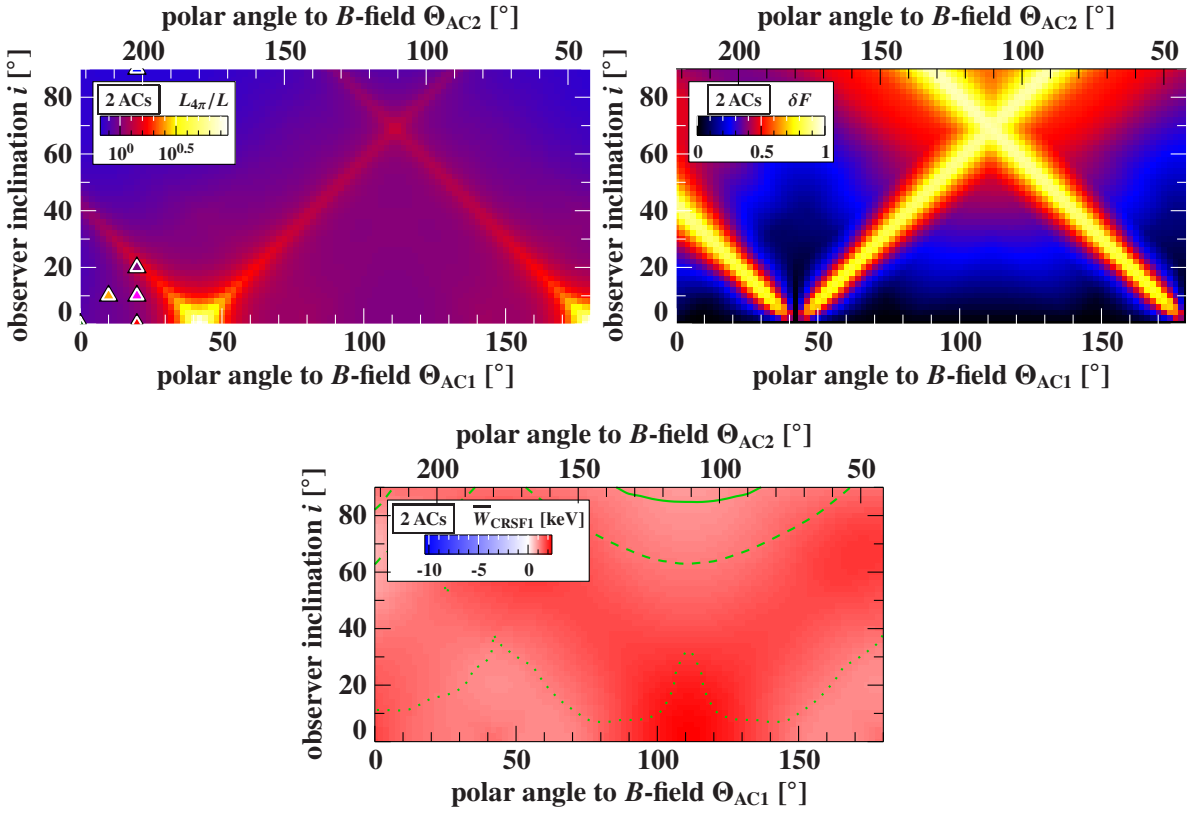

Figure 3.22.: Geometrical dependencies for the asymmetric two-column setup (see Table 2.1). **Top left:** Anisotropy of the flux derived luminosity (see Fig. 3.16) **Top right:** Pulsed fraction of energy integrated pulse profiles (see Fig. 3.17). **Bottom:** Phase averaged equivalent width of the CRSF in the energy range from 5 keV to 25 keV (see Fig. 3.19).

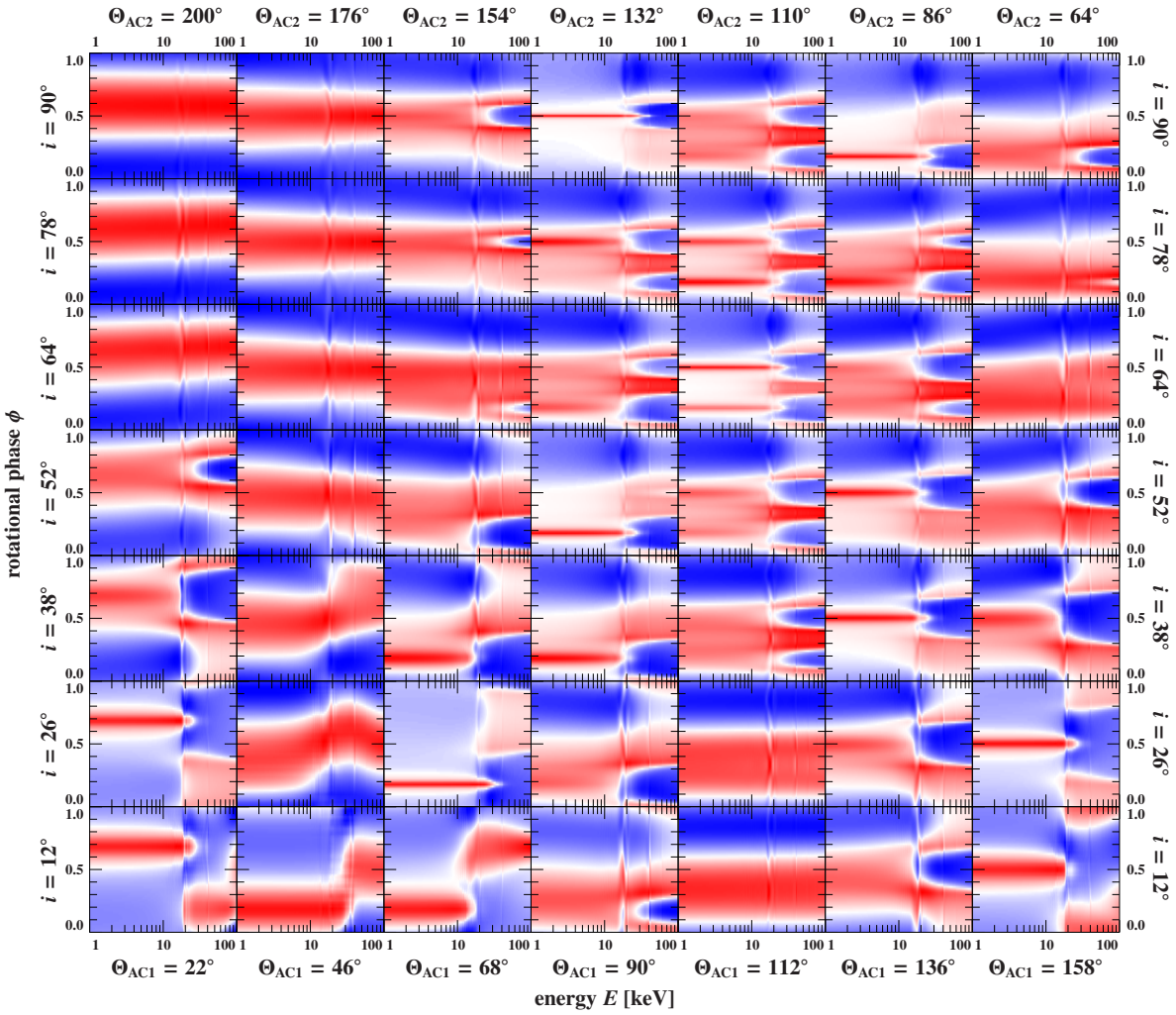

Figure 3.23.: Normalized observed phase and energy dependent flux, $\tilde{F}_E(\phi)$ (see Eq. 3.20). Same as in Fig. 3.14, but for the asymmetric two-column setup (see Table 2.1).

3.2.5.7 Summary

Table 3.2 shows an overview of the previously discussed observables, their minimum and maximum values occurring in the phase-averaged spectra, as well as the maximum phase amplitude in the phase-resolved spectra.

It is noticeable that the range in which the phase-averaged values vary is equal to the maximum phase amplitude. This observation is easily explained by the fact that we are looking at all possible combinations of i and $\Theta_{\rm AC}$. In particular, we see the minimum and maximum values in the phase-averaged spectra stepping through different polar angles $\Theta_{\rm AC}$ for $i = 0°$, for which there are no pulsations ($\delta F = 0$). On the other hand, the maximum phase amplitude is related to the geometry for $i = \Theta_{\rm AC} = 90°$. Both cases equally allow us to observe the magnetic field under all possible view angles.

Comparing the single and antipodal two-column case, the variability of the observables with the geometrical configuration (i, $\Theta_{\rm AC}$) and with phase are impacted in different ways. As in the antipodal case, the second column significantly reduces the range and amplitude

Table 3.2.: Ranges and phase amplitudes of the observed quantities.

parameter	unit	single column			antipodal columns			asymmetric columns[a]		
		$\overline{\text{min}}$	$\overline{\text{max}}$	A	$\overline{\text{min}}$	$\overline{\text{max}}$	A	$\overline{\text{min}}$	$\overline{\text{max}}$	A
$L_{4\pi}/L$		10^3	22	...	0.8	11	...	0.8	11	...
δF^b		0.00	1.00	1.00	0.00	0.87	0.87	0.00	0.93	0.93
Γ		0.09	0.34	0.24	0.09	0.27	0.17	0.10	0.27	0.20
E_{fold}	[keV]	2.8	3.6	0.81	2.8	3.6	0.81	2.8	3.6	0.82
W_{CRSF1}	[keV]	−10.4	2.4	12.8	1.1	1.7	0.6	0.7	2.4	4.7
W_{CRSF2}	[keV]	−1.5	−0.5	1.0	−1.5	−0.6	0.9	−1.4	−0.7	0.6
E_{CRSF2}	[keV]	25	40	15	32	40	9	32	40	9
σ_{CRSF2}	[keV]	0.9	10.0	9.1	0.9	4.9	3.2	0.9	5.3	4.5
d_{CRSF2}	[keV]	0.4	2.6	2.2	0.4	1.6	1.1	0.5	1.5	0.8
τ_{CRSF2}		0.06	0.48	0.42	0.06	0.45	0.39	0.06	0.48	0.42
W_{CRSF3}	[keV]	−0.33	−0.05	0.27	−0.31	−0.14	0.18	−0.32	−0.14	0.20
W_{CRSF4}	[keV]	−0.11	−0.00	0.11	−0.10	−0.00	0.10	−0.10	−0.02	0.09

Notes. Columns show the minimum, $\overline{\text{min}}$, and maximum, $\overline{\text{max}}$, values in the phase-averaged spectra and the maximum phase amplitudes, A, in the phase-resolved spectra for a single, two antipodal, and two asymmetric columns, respectively. $^{(a)}$ Displacement parameters of the asymmetric setup are given in Table 2.1. $^{(b)}$ Values are related to energy-averaged spectra.

of the anisotropy factor, the energy and width of the harmonic CRSF, and even results in the fundamental CRSF to be observed only in emission. In other cases the second column, whether antipodal or asymmetric, has almost no impact. This is the case, for example, for the folding energy of the `CutoffPL` continuum and the `gabs` optical depth of the harmonics.

As an example, Table 3.2 also shows the results for two columns located asymmetrically on the neutron star. Although the asymmetry does change the geometrical dependencies of the observables (see Sect. 3.2.5.6), the ranges and amplitudes are only slightly different compared to the antipodal case. The only exception is the equivalent width of the fundamental CRSF, which has a higher range and amplitude for the asymmetric columns. The reason for this behavior is the high sensitivity and variability of the fundamental CRSF shape with the viewing angle to the magnetic field, combined with the strong dependency of the flux derived luminosity of the individual columns on the geometry.

3.3 Discussion & Conclusions

With the modular model presented here we describe the energy and phase dependent observed flux of accreting neutron stars in X-rays in an unprecedented self-consistent way. Our approach is based on the combination of three individual models, each of which describes different aspects within and around the accretion column. We obtain the conditions within

the accretion column, its dimensions, and its continuum emission from Postnov et al. (2015). Onto this continuum we imprint CRSFs based on the model by Schwarm et al. (2017a,b). This combination of two models provides the specific intensity of the accretion column(s), which we transform into the observer frame accounting for general relativistic effects using a new ray tracing code (see Chapter 2).

The modularity of our approach also has some limitations. Especially at the interfaces of the continuum and the CRSF model. Each of these models addresses different specific problems of the radiative transfer within the column and has its own scope of application within different boundaries. Nevertheless, this separation is necessary, as a comprehensive model which includes both, the formation of the continuum and the CRSF, would be too computational expensive (see e.g., Schwarm et al., 2017b). The drawback of our approach, however, is that it implies an abrupt transition between the two regions. As discussed in Sect. 3.1.1, the continuum (Postnov et al., 2015) is formed at the surface of constant optical depth, $\tau_\perp = 1$. While the CRSF calculation (Schwarm et al., 2017a,b) assumes a very thin outermost layer which has an optical depth of $\sim 10^{-4}$. Nevertheless, we assume the electron temperature and the bulk velocity to be the same in both layers as the spatial separation is negligible. Within the CRSF layer we neglect the redistribution of photons in height due to its subdivision into spatially infinitesimal slabs in vertical direction to account for parameter gradients. Furthermore, the model by Postnov et al. (2015) used for the continuum emission is based on Lyubarskii (1986), which considers the photon energy to be smaller than the fundamental line energy, which itself is to exceed the electron temperature, i.e., $E' \ll E'_{\mathrm{CRSF1}}$ and $E'_{\mathrm{CRSF1}} \gg kT$. While the second condition is met, the first one is only partially fulfilled. As a consequence the contribution of ordinary photons to the continuum especially at higher energies is underestimated. An estimate of this deviation is only possible based on a more sophisticated description of the accretion column emission (e.g., based on Becker & Wolff, 2007, Becker et al., 2012).

In this work we present results based on one particular model setup using one continuum model in a specific configuration (Table 3.1), especially using one fixed mass accretion rate. Nevertheless it is possible to derive statements not only valid for this specific setup, but which are also generally true. Some of the discussed observables and their behaviors are not tied to the exact form of the emission pattern and geometry of the accretion columns as discussed in the following.

3.3.1 Special geometries

Throughout this work we investigated observables such as the flux derived luminosity, pulse profiles and the according pulsed fraction, the observed phase-resolved and phase-averaged continuum and CRSFs. In particular we focused on their dependency on the geometrical parameters, the inclination i of the observer, and the polar angles $\Theta_{\mathrm{AC1,2}}$ of the accretion columns. We find that geometries where $i + \Theta_{\mathrm{AC1,2}} \approx 180°$ are special. These geometries feature a column which roughly aligns with the line of sight on the opposite side of the neutron star at a certain rotation phase (see Sect. 3.2.4). For these geometries the visibility of the emitting region is significantly enhanced due to the effect of strong light bending. The compactness of the neutron star determines the size of the shadow region, which in

combination with the vertical distribution of the emissivity of the column influences the strength of this effect onto the observed flux.

The number of emission regions considered is also important. There are significant differences between the observables when comparing the single and the two-column cases. The best example is the effect of strong light bending, which boosts the emission observed from the column behind the neutron such that the column in the front is out-shined. As a consequence we are not able to observe flux emanating under small angles to the magnetic field as its contribution to the overall flux of both columns is insignificant. This effect increases with increasing compactness of the neutron star.

3.3.2 Pulse profiles

Regarding the simulated pulse profiles there is one peculiar effect resulting in narrow, but prominent peaks as seen in Fig. 3.11, with widths of only a few percent of the pulse phase. Such peaks are generally hard to explain as a fan beam emission feature, which normally emits into a large solid angle. The effect of strong light bending, however, provides a very good possible explanation. During a short phase interval the projected area is enlarged causing a short but strong pulse. This behavior is an effect that only occurs for certain geometries and therefore allows us to infer geometrical properties (see Sect. 3.2.4).

Observational examples, for which this effect is applicable, are the pulse profiles of KS 1947+300 (see, e.g., Fürst et al., 2014a, Ballhausen et al., 2016, Epili et al., 2016) and IGR J16393−4643 (see, e.g., Islam et al., 2015, Bodaghee et al., 2016). These sources show such narrow peaks in the hard X-rays, where it is difficult to argue that these peaks are a result of absorption. In case of KS 1947+300 the disappearing of the peak for energies below 10 keV could relate to a lowering of the emission region within the column for decreasing energy. In other words, a transition of the emission region into the shadow region would cause the fade-out of the corresponding peak. The pulse profiles of these two sources are observed at flux derived luminosities of $\sim 10^{37}$ erg s^{-1}. Above this luminosity we expect the column emission pattern to be mainly a fan beam, while at lower luminosities it is mixed with pencil beam emission (Becker et al., 2012). The prominent peaks in these pulse profiles result in a very high pulsed fraction in our simulations. They also dominate the correlation between the pulse fraction and the geometry in i and $\Theta_{\mathrm{AC1,2}}$ (see Sect. 3.2.5.3), especially in the two-column setup. For the single-column setup the high pulse fractions for $\Theta_{\mathrm{AC1}} < 90^{\circ}$ are caused by deep dips which occur when the column is observed from above due to the absence of a pencil beam.

The pulse profile of the accreting pulsar GS 0834−430 shows a steady shift with energy in the X-ray band (see Figs. 3 and 4 in Miyasaka et al., 2013) similar to some cases in Fig. 3.23 featuring asymmetric accretion columns (see Sect. 3.2.5.6). This behavior is especially interesting as GS 0834−430 shows no detectable CRSFs, which are usually associated with such so called phase lags (e.g., Ferrigno et al., 2011, Schönherr et al., 2014). Here, however, we show that such changes of the pulse profile with energy are also possible without CRSFs. When the column passes through the shadow region (Sect. 3.2.4) hard emission from its bottom is blocked and the observed flux is dominated by the softer continuum which originates form higher in the column (see Sect. 3.2.5.1).

3.3.3 Luminosities

We showed that it is important to distinguish between the flux derived luminosity inferred from observations, the bolometric luminosity seen on the unit sphere in the rest frame of the observer, and the intrinsic luminosity emitted from the accretion column. There is always a certain systematic error when relating the flux derived luminosity, $L_{4\pi}$, to the bolometric luminosity, L, as we lack information about the luminosity distribution with the observer inclination (see Sect. 3.2.5.2). The overestimate of the observed luminosity decreases with the decrease of the compactness of the neutron star, as the effect of light bending decreases. The amount of this systematic error, however, depends also on the exact model setup. We obtain anisotropy factors, $L_{4\pi}/L$, which in the case of a two-column setup imply that the real and inferred luminosity can differ by a factor up to 11.

Another factor of uncertainty is the amount of the gravitational redshift. The exact value not only depends on the compactness of the neutron star, but also on the spatial distribution of the emission. Assuming a peak emissivity close to the neutron star's surface and theoretical possible mass-radius relations (see e.g., Steiner et al., 2013), we get $R_s/R_{NS} \approx 0.15$–0.74 corresponding to a gravitational correction factor of 0.26–0.85 between the bolometric luminosity, L, and intrinsic luminosity, $L^\star$.

Together, the anisotropy factor and the uncertainty in the gravitational redshift can cause an over- or underestimate of the intrinsic luminosity by roughly a factor of 4–10.

Finally, one has to keep in mind that it is possible that a large fraction of the fan-beam emission is directed towards the neutron star's surface and therefore is not directly observable (see Sect. 3.2.1). In our case 58% of the intrinsic luminosity emitted from the column is intercepted by the neutron star. Higher bulk velocities increase this fraction due to the increase of the downward boosting of the emission. Therefore reflection off the neutron star atmosphere or neutron star's surface has to be considered when relating the flux derived luminosity to the intrinsic luminosity.

3.3.4 Continuum

In Sect. 3.2.5.4 we fit the phase-averaged as well as the phase-resolved observed continuum with a simple `CutoffPL`. We find that the photon index depends on the folding energy, and therefore on the plasma temperature. This dependency results from the integrated contribution of emission from different heights and viewing angles to the observed flux. Furthermore we consider only the direct observed emission. Emission reflected from the atmosphere of the neutron star increases the hardness ratio of the observed spectrum (Postnov et al., 2015). Additionally it is possible that the emission at higher energies ($E > E_{CRSF1}$) is underestimated due to the negligence of ordinary photons, which might cause lower values of E_{fold} and Γ.

As shown in Fig. 1.9 observations of accreting X-ray pulsar cover a broad range of phase-averaged spectral shapes in terms of photon indices and folding energies. In the different sources $\overline{\Gamma}$ ranges from -2.2 to 2.2 and $\overline{E}_{fold}$ ranges from 2 keV to 49 keV.[11] While our simulated values (Table 3.2) lie within these ranges, they are still lower than those observed in most sources. The spectral shape also changes within each source depending on its current

[11] Note that these values where obtained based on different continuum models.

luminosity, which ranges from 3×10^{34} erg s^{-1} up to 10×10^{37} erg s^{-1}, linked to different mass accretion rates. Our simulations are based on a fixed mass accretion rate, that is intrinsic luminosity. The presented variability in the flux derived luminosity, however, is due to its geometrical dependency.

In the recent years also more and more phase-resolved analyses were performed (see Fig. 1.10) thanks to the increasing data quality with new missions (like, e.g., *NuSTAR*). For the sample of sources shown in Fig. 1.10 the variability of the continuum with pulse phase covers a large range with maximum amplitudes between $A_\Gamma = 0.0$–1.8 and $A_{E_{\rm fold}} = 0.3$–38 keV. Compared to these observational amplitudes the phase variability of the continuum in our simulations is small ($A_\Gamma \leq 0.17$, $A_{E_{\rm fold}} \leq 0.81$ keV; Table 3.2).

3.3.5 CRSF

Regarding the fundamental CRSF the predictions of our simulations are surprising and in contradiction to observations. Amongst all those accreting X-ray pulsars featuring CRSFs, there is no evidence of a CRSF in emission or with emission wings yet (Figs. 1.9 and 1.10), despite the fact that all theoretical models of CRSFs predict these emission features as a result of photon spawning (see Isenberg et al., 1998, Nishimura, 2008, Schwarm et al., 2017a,b, and references therein).

With our comprehensive simulation we show that for any two-column geometry the fundamental CRSF is in emission with equivalent widths large enough to be detectable (Fig. 3.19). Asymmetric positioned columns do not significantly change this observable (Fig. 3.22). There are several interlinked conditions leading to this problem, starting with the fact that the spawned photons are predominantly emitted perpendicular to the magnetic field. As a result the emitted intensity is enhanced in a broad angle range between $45° < \eta' < 135°$ (Fig. 3.8). Considering any fan beam like emission pattern provides an angle distribution of the emission which peaks perpendicular to magnetic field (Eq. 3.1; Fig. 3.2). Such fan beam patterns increase the intensity of the CRSF emission relative to the CRSF absorption at smaller angles to the magnetic field. Lastly relativistic light bending not only increases the range of visibility of the column being behind the neutron star (Fig. 3.13), but additionally gives a boost to the observed flux (Fig. 3.16) in these cases, in which the column is seen also mostly sideways. Altogether the described model predicts the fundamental CRSF to be observed mostly in emission for a two column setup with fan beam like emission.

There are some possible approaches to solve the problem, but none of them resolves this discrepancy between model and observations completely. As the fundamental CRSF is in absorption for small angles to the magnetic field and in emission for angles roughly perpendicular, one solution would be that the fan beam is not the predominant kind of emission, but pencil beam emission is in any case. For example, emission regions, which are not vertically extended would automatically favor a pencil beam. Fan beam emitting accretion columns, however, are a commonly accepted concept (e.g., White et al., 1983, Becker et al., 2012). It might also be the case that the direct observed fan beam emission is out-shined by the reflection off the neutron star's surface. Focusing a sufficient fraction of the emission down to the surface, however, requires a high bulk velocity, especially in cases of a vertically extended emissivity profile of the column. Even then it is questionable, if there are significant less

spawned photons filling up the fundamental CRSF in the reflected spectra. Another solution would be that the timescale for collisional de-excitation of the Landau levels is lower than the radiative one, which would eliminate the existence of spawned photons in the first place. In that scenario, however, the plasma density would have to be significantly higher, especially in the CRSF forming region. Generally the line formation is completed roughly within the first Thomson optical depth. In the case of the CRSFs the cross sections in the resonance are several magnitudes higher than in the off-resonance (Schwarm et al., 2017b), and therefore need only a tiny fraction of a Thomson optical depth to be formed. As a consequence this scenario would require the accretion stream to be confined in a very small radius with an extremely sharp transition zone.

Another case partially improving the situation are neutron stars of lower compactness, that is neutron stars exhibiting a larger shadow region (Fig. 3.13). In combination with an emissivity distribution, which has a small extent in height, a lower compactness would decrease the impact of strong light bending. As a result, the emission from the front column seen under small angles to the magnetic field, which provides deep absorption lines in the fundamental CRSF, would be observable also in two-column configurations. That, however, is only the case for some geometries and also only for some part of the pulse phase.

Besides the fundamental CRSF, we additionally find also the first three harmonics ($n = 2, 3, 4$) in our simulated spectra all behaving similar, but with rapidly decreasing equivalent widths with respect to n (Table 3.2). A detailed investigation of the first harmonic CRSF, that is fitting it with the `gabs` model, shows a strong anti-correlation of the width and optical depth of the CRSFs. The harmonics further show a clear asymmetry with shallow extended lower energy flanks. Observations of V 0332−53 (Pottschmidt et al., 2005), Cep X-4 (Fürst et al., 2015) and 4U 1626−67 (Iwakiri et al., 2018) reveal a very similar asymmetry of the CRSF.

Accounting for the relativistic bulk velocity of the in-falling plasma is important as the corresponding angle dependent boosting (Eq. 2.29) can lead to strong variations of the CRSF with phase. This boosting is especially interesting in the case of the CRSF energy. The intrinsic line energy is almost independent of the viewing angle (Eq. 1.9) as is the gravitational redshift (Eq. 2.27). The consideration of the bulk velocity (Eq. 3.18), however, introduces an angle dependency and therefore significant phase variations in the observed flux. Many explanations for observed phase variations of the CRSF energy are based on the visibility of different magnetic field strengths. Our simulations, however, show that the phase-resolved CRSF energy can vary up to 23% (antipodal two-column setup) around its phase-averaged value just due to the angle dependent boosting factor. The pulse phase dependency of the CRSF energy in GX 301-2, for example, can be explained solely with this effect as discussed in Sect. 4.2.

Chapter 4 Applications to observational data

In the last chapter we discussed the flux observed of accreting X-ray pulsars in great detail from the theoretical point of view. In the following chapter I present an observational approach on the basis of two examples. In Sect. 4.1 I discuss the pulse profiles of 4U 1626−67 and their peculiar dependency on energy. I show that a simple emission profile consisting of a fan- and pencil-beam mixture is able to model these pulse profiles. In Sect. 4.2 I utilize the angle-dependency of the boosting factor due to the bulk velocity (see Chapter 3) to model the variations of the CRSF energy with phase observed in GX 301−2.

4.1 The pulse profile of 4U 1626–67

In this section I present my work on modeling pulse profiles of 4U 1626−67. This analysis is my contribution to the upcoming publication by Iwakiri et al. (2018) and therefore this section is following it closely and in larger parts in verbatim.

4U 1626−67 is an X-ray source discovered by *UHURU* (Giacconi et al., 1972). Rappaport et al. (1977) later found a pulse period of 7.7 s in X-rays. This source is in an ultra compact binary system with a very low mass companion (Levine et al., 1988). The orbital period of this binary is only 42 min, while the system is located at a distance between 5 and 13 kpc (Middleditch et al., 1981, Chakrabarty, 1998). The stellar wind from the companion is not sufficient to explain the observed X-ray luminosity on the order of $\sim 10^{37}$ erg s^{-1}. The accretion is most likely driven by Roche lobe overflow (Chakrabarty, 1998). Orlandini et al. (1998) discovered that the spectrum of 4U 1626−67 features a CRSF at ∼ 37 keV, which was later found to be of asymmetrical shape with a shallow low energy flank (D'Aì et al., 2017, Iwakiri et al., 2018).

The pulse profile of 4U 1626−67 shows a very peculiar evolution with energy in X-rays. The center panels of Figs. 4.1 and 4.2 show the energy-resolved and background subtracted pulse profiles in eleven different energy bands obtained with *NuSTAR* in 2015 (see Iwakiri et al., 2018, and references therein). The pulse profiles strongly depend on energy, with a

double-peaked structure below 10 keV which become single-peaked and almost sinusoidal in the higher energy bands. The characteristics of the pulse profiles seen by *NuSTAR* are consistent with the *RXTE* results observed in 2010 (Beri et al., 2014).

To investigate the geometry of the neutron star quantitatively, we performed pulse profile modeling using the relativistic ray tracing code discussed in Chapter 2. In our model for 4U 1626−67 we consider a canonical neutron star of mass $M_{\rm NS} = 1.4 M_\odot$ and radius $R_{\rm NS} = 10\,$km. Further, we assume the observed X-rays to be emitted by two cylindrical accretion columns AC1 and AC2 of height $h_{\rm AC1,2}$ and radius $r_{\rm AC1,2}$. Allowing for an asymmetric magnetic field, the columns are positioned individually at azimuthal angles $\Phi_{\rm AC1,2}$ and polar angles $\Theta_{\rm AC1,2}$, respectively. These angles are measured in a coordinate system with respect to the neutron star's rotational axis (see Fig. 3.7). The angle between the line of sight and the neutron star's angular momentum vector specifies the inclination i of the neutron star. Therefore $i = 0°$ would correspond to a face-on system.

We make the simplified assumption that the emission pattern of the columns can be described as a mixture of Gaussian-like fan and pencil beam emission components in the frame of rest of the neutron star's surface. At a given observed energy the emissivity of one accretion column is given by

$$I'_E(\eta') = N_{\rm p} \exp\left(-\left[\frac{\eta' - \bar{\eta}_{\rm p}}{\sqrt{2}\sigma_{\rm p}}\right]^2\right) + N_{\rm f} \exp\left(-\left[\frac{\eta' - \bar{\eta}_{\rm f}}{\sqrt{2}\sigma_{\rm f}}\right]^2\right) \quad , \tag{4.1}$$

where η' is the angle of the emitted photons measured with respect to the magnetic field axis in the frame of rest of the emitter (see Fig. 3.2). The energy dependent quantities $\bar{\eta}$, σ, and N describe the direction of peak emissivity, the width, and the strength of the pencil-beam (p) and fan-beam (f) components, respectively. Note that all these quantities are given in the rest frame of the emitter, which is indicated with a prime in same cases for clarity following the notation given in Sect. 2.1.4. As we do not assume any bulk velocity ($\beta = 0$) the rest frame of the emitter is the same as the rest frame of the neutron star. For the fan beam we set $\bar{\eta}_{\rm f} = 90°$, i.e., the fan beam is fixed to emit perpendicular to the magnetic field from the sides of the accretion column.

We model the energy-dependence of the pulse profile by allowing the parameters N, σ, and $\bar{\eta}$ of the emission pattern to change with energy. For the model described in the following we assume that the emissivity of the accretion column is independent of height and thus constant over the whole column. From Eq. (4.1) we then derive the observed energy- and phase- dependent total flux,

$$\mathcal{F}_E(\phi) = F_{\rm AC1}(\phi, I'_E) + F_{\rm AC2}(\phi, I'_E) \quad , \tag{4.2}$$

where ϕ is the rotational phase and $F_{\rm AC1,2}$ is the flux of the individual accretion columns emitting with the given emission pattern I'_E. The fluxes in Eq. (4.2) are calculated following the description in Chapter 2 accounting for general relativistic effects. While we impose the same model for the emissivity pattern on both poles, the fluxes of the beams are allowed to vary freely. In particular that means $N_{\rm p_2} = N_{\rm p_1}$, $\sigma_{\rm p_2} = \sigma_{\rm p_1}$, $\bar{\eta}_{\rm p_2} = \bar{\eta}_{\rm p_1}$ for the pencil beam, and $\sigma_{\rm f_2} = \sigma_{\rm f_1}$ and $\bar{\eta}_{\rm f_2} = \bar{\eta}_{\rm f_1} = 90°$ for the fan beam.

The center panels in Figs. 4.1 and 4.2 include the best-fit model described above for the energy-resolved and background subtracted *NuSTAR* pulse profiles in the eleven energy bands. Lines show the overall model and the individual contributions of the fan and pencil beams

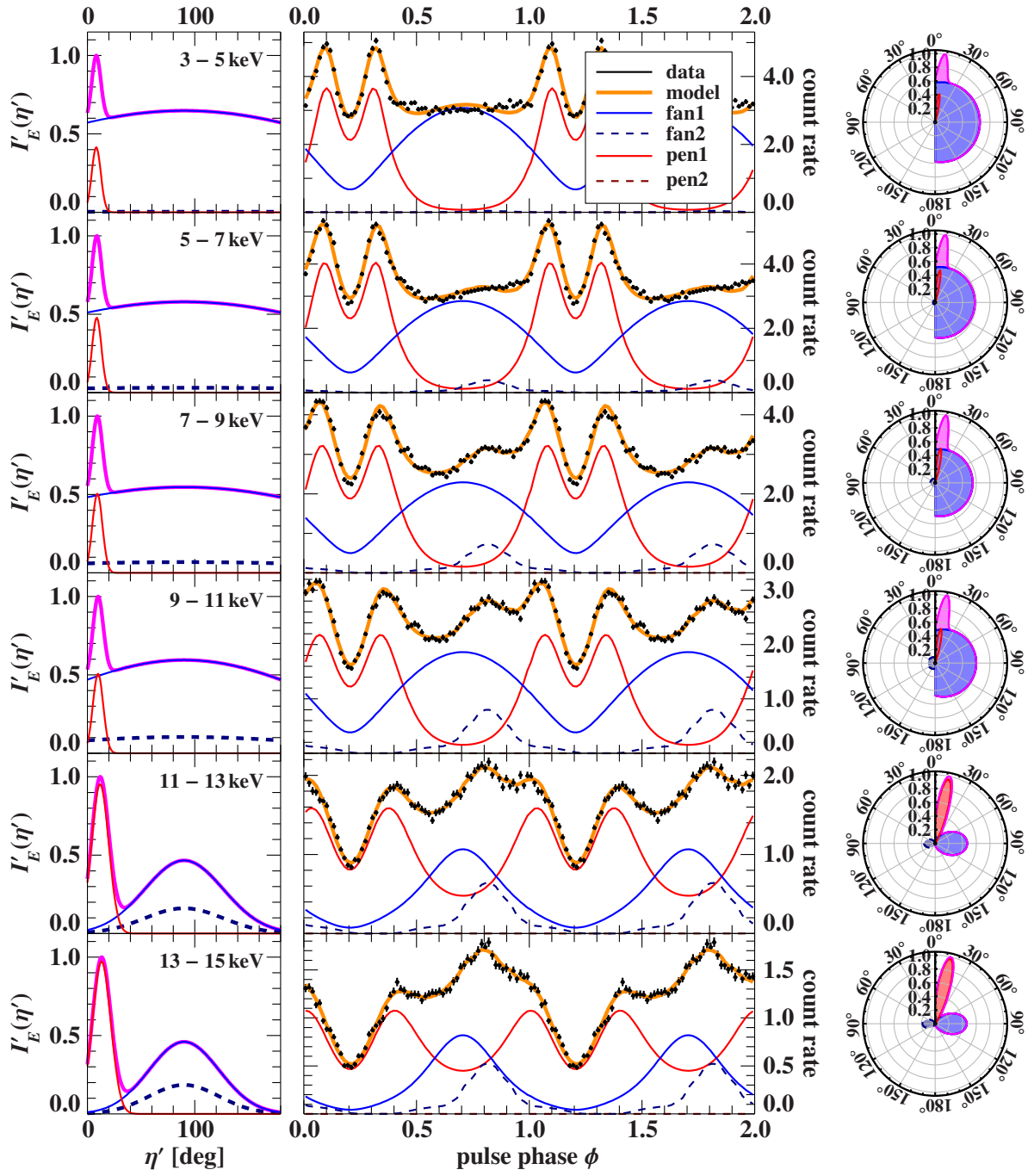

Figure 4.1.: Modeled emission patterns and pulse profiles of 4U 1626−67 in different energy bands. The center panels show the pulse profiles obtained with *NuSTAR* (black points) and the fitted model (orange) with its individual components, i.e., the fan (solid blue, dashed navy) and pencil emission (solid red, dashed maroon) of both accretion columns. The left-hand panels show the corresponding normalized emission patterns of the two accretion columns. The solid magenta line corresponds to the combined emission pattern of the fan and pencil beam of the first column. The right-hand panels show the same emission patterns as polar plot, where the right and left side counting η' clockwise and counter-clockwise correspond to the first and second accretion column, respectively. The best-fit parameters are shown in Table 4.1.

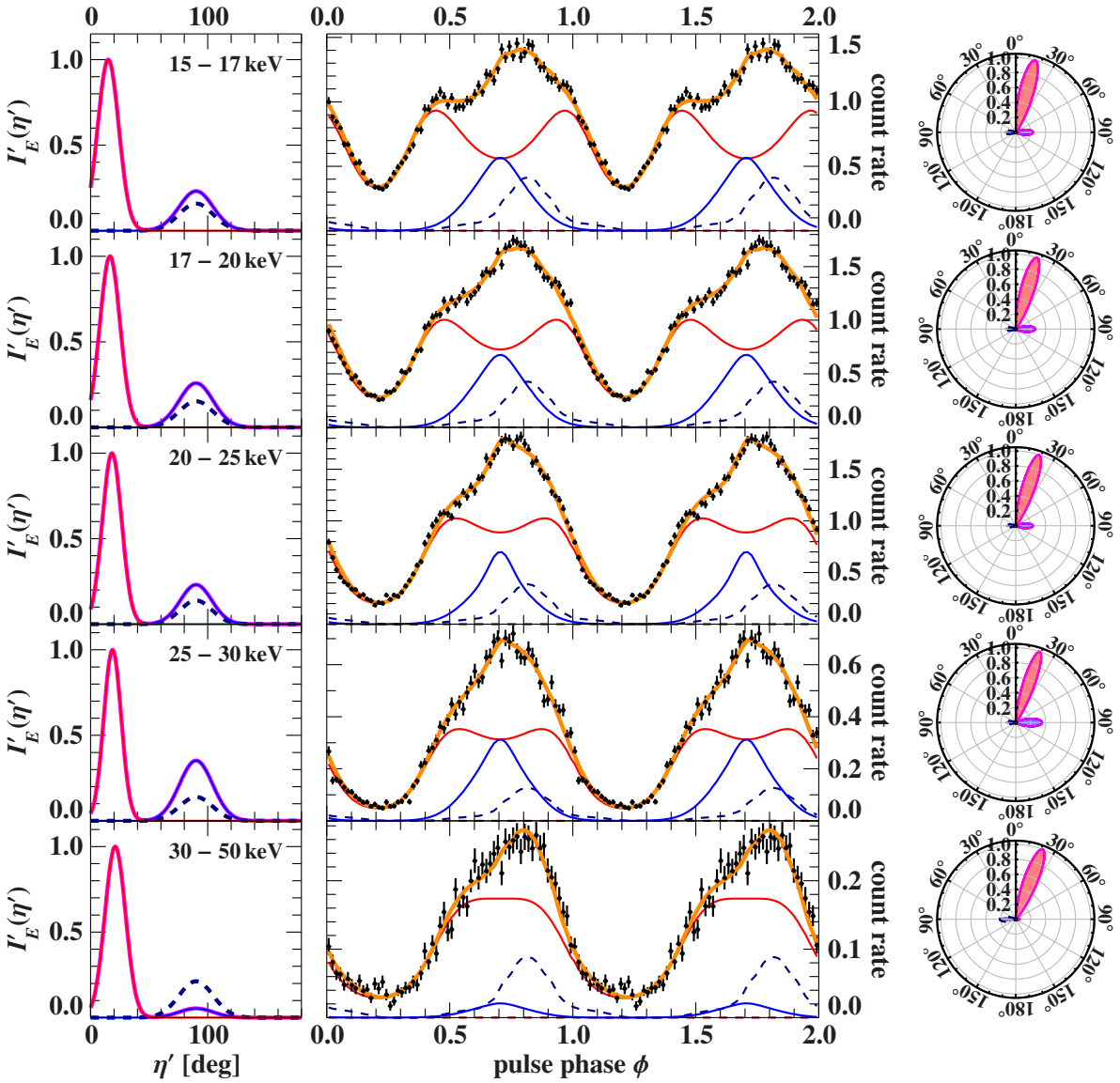

Figure 4.2.: Figure 4.1 continued.

from each accretion column. The corresponding parameters are listed in Table 4.1. While the parameters of the emissivity profile are allowed to change with energy, the geometrical parameters describing the locations and dimensions of the columns are not. Another global parameter is the observer inclination, which naturally also does not change with energy.

The best-fit solution shows that the magnetic field of the first column passes through close to the line of sight during each rotation. That is at pulse phase $\phi = \Phi_{\mathrm{AC1}}$, when the first column is in the front, we look at the first column from above with an angle to its magnetic field axis of approximately $\Theta_{\mathrm{AC1}} - i = 6.^{\circ}1$. Despite the simplified assumptions entering the beam pattern, the model describes the observed pulse profiles and their energy evolution remarkably well and with a smooth variation of all relevant parameters of the emission characteristics. Figure 4.3 shows the energy dependency of the parameter values. The evolution of the pulse profile is characterized by a very wide fan beam which strongly decreases in width as the energy increases. In contrast, the shape of the pencil beam component only slightly changes.

Table 4.1.: Fit parameters of the accretion column model. Parameters not listed here are fixed or tied. In particular we impose $N_{p_2} = N_{p_1}$, $\sigma_{p_2} = \sigma_{p_1}$, $\bar{\eta}_{p_2} = \bar{\eta}_{p_1}$ for the pencil beam, and $\sigma_{f_2} = \sigma_{f_1}$ and $\bar{\eta}_{f_2} = \bar{\eta}_{f_1} = 90°$ for the fan beam.

global	AC1				AC2				
i [deg]	Φ_{AC1} [deg]	Θ_{AC1} [deg]	r_{AC1} [m]	h_{AC1} [m]	Φ_{AC2} [deg]	Θ_{AC2} [deg]	r_{AC2} [m]	h_{AC2} [m]	χ^2_{red} (d.o.f.)
10.8	74.0	16.9	123	150	294.0	159.0	634	221	2.13 (629)

	pencil$_1$			fan$_1$		fan$_2$	
ΔE [keV]	N_{p_1} [cts/s]	σ_{p_1} [deg]	$\bar{\eta}_{p_1}$ [deg]	N_{f_1} [cts/s]	σ_{f_1} [deg]	N_{f_2} [cts/s]	χ^2_{red} (d.o.f.)
3 – 5	0.848	4.2	8.2	1.322	180.0	0.007	5.15 (58)
5 – 7	1.013	4.4	8.7	1.225	180.0	0.066	3.45 (58)
7 – 9	0.911	4.7	9.3	0.986	180.0	0.124	2.58 (58)
9 – 11	0.671	4.9	9.9	0.787	130.7	0.137	1.28 (58)
11 – 13	0.642	8.1	11.8	0.314	36.6	0.109	1.18 (58)
13 – 15	0.466	8.6	13.1	0.220	32.7	0.089	1.24 (58)
15 – 17	0.431	9.0	15.0	0.100	14.5	0.068	1.18 (58)
17 – 20	0.462	8.6	16.5	0.120	14.5	0.071	1.82 (58)
20 – 25	0.454	8.2	18.2	0.105	13.4	0.063	2.15 (58)
25 – 30	0.149	7.4	18.7	0.053	14.2	0.021	1.85 (58)
30 – 50	0.069	8.8	21.0	0.004	14.6	0.015	1.23 (58)

The widening of the pencil beam width with energy is negligible, while the increase of the angle of the peak emission from 8 deg to 21 deg is relevant. This shift explains the widening of the gap between the double peak in the pulse profile. From 3 keV to 10 keV the parameters corresponding to the first column change only slightly, while the normalization of the second column's fan beam increases by an order of magnitude. This increasing contribution of the second column explains the changes seen in the pulse profile at these lower energies, which are noticeable as a raising third peak located slightly asymmetric regarding the double peak at the phases of the plateau.

The decomposition of the pulse profiles in the middle columns of Figs. 4.1 and 4.2 illustrates how these parameter changes manage to reproduce the pulse profiles so well: The pencil beam is responsible for the distinct and symmetric double peak that characterizes the softer energy bands. The peaks are close together since the pencil beam is directed upwards, with only a small offset, $\bar{\eta}_p$, to the magnetic field. The strong non-pulsed continuum between the two peaks is produced by the broad fan beam, which is shifted by half a phase with respect to the dip between the double peak of the pencil beam. With increasing energy the double peak decreases in importance and its width broadens while the gap in between increases. This behavior is reflected in the best-fit parameters by showing that the offset angle $\bar{\eta}_p$ and the beam width σ_p increase with energy (see Fig. 4.3). In addition, the flat plateau at low energies evolves into an asymmetric peak, which is caused by the narrowing of the fan beam. The asymmetry visible

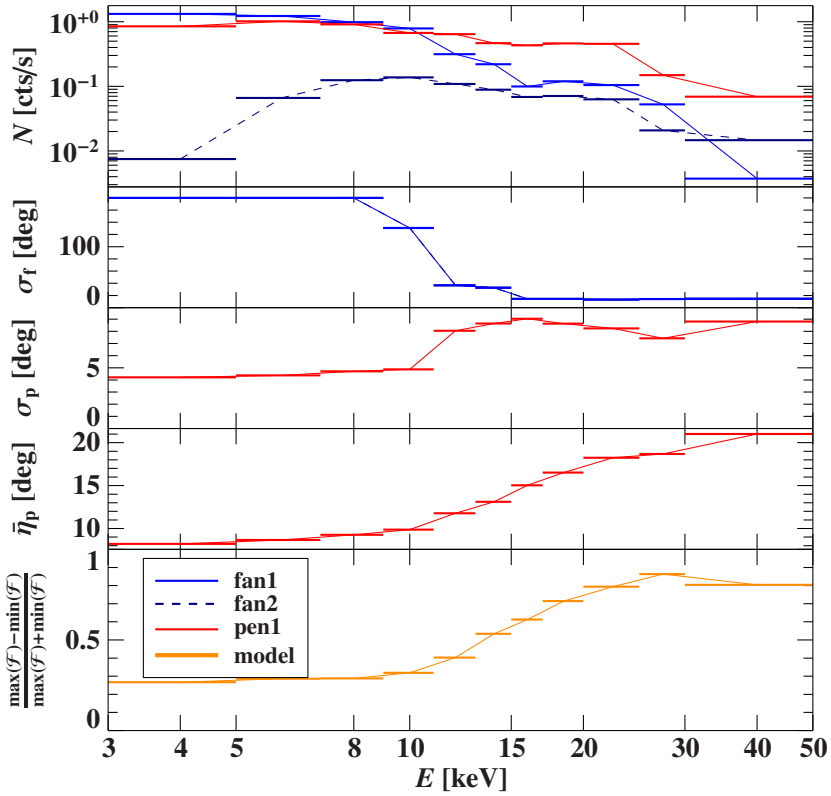

Figure 4.3.: Energy dependent fit parameters of the accretion column model, with the model's pulsed fraction in the bottom panel. See Table 4.1 for the best-fit parameters. Note that the emission angle for the fan beam is fixed at $\bar{\eta}_f = 90°$.

in this pulse is caused by the fan beam of the slightly-misaligned second accretion column. As a consequence of this best-fit geometry the pencil beam of the second column is directed away from the observer at all pulse phases, and thus it is not observable. In Fig. 4.3 we see that the pulsed fraction increases significantly with energy. That evolution is driven by the changes of the primary pencil beam. While at lower energies the peak contribution of pencil and fan beam to the pulse profile are shifted by half a phase causing a small pulsed fraction, the evolution of the pencil beam causes both contributions to coincide in phase which results in a high pulse fraction (Figs. 4.1 and 4.2).

We note that extrapolating the behavior of the pencil and fan beams to even lower energies than considered here predicts an evolution of the pulse profile towards a shape dominated by the single broad hump of the fan beam, consistent with the pulse profiles seen by *XMM-Newton* (Krauss et al., 2007) and *Chandra* (Hemphill et al., 2017).

Modeling the pulse profiles also yields our viewing angle onto the two accretion columns. This parameter is important for the interpretation of the CRSF, whose shape strongly depends on the angle under which we see the magnetic field (Schwarm et al., 2017b,a). The viewing angle, under which the magnetic field is seen, relates directly to the emission angle η' in the rest frame of the emitter.[1] As shown in Fig. 4.4, η' is strongly influenced by light bending.

[1]This relation is analog to the relation of the apparent emission angle (Ψ) and the radial emission angle (α) of the photon trajectory as discussed in Chapter 2 (see Fig. 2.1).

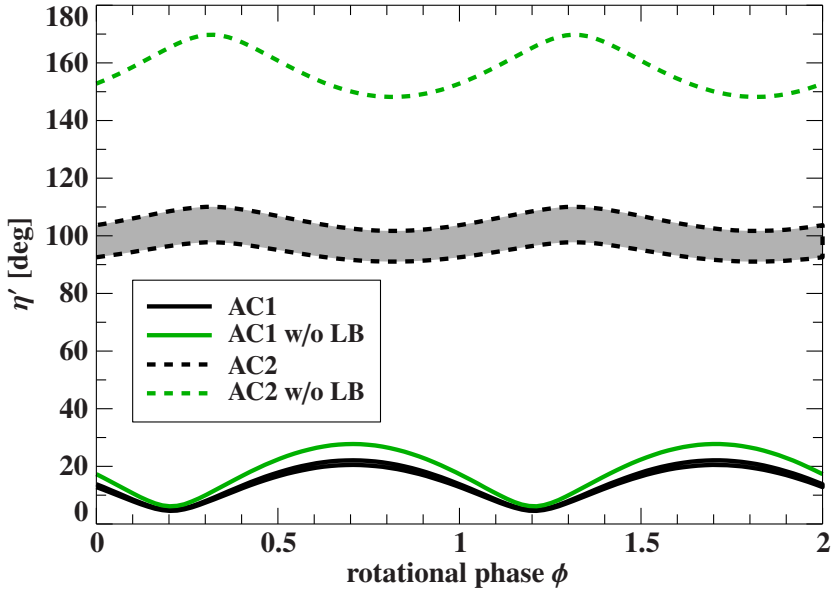

Figure 4.4.: Phase dependent angle, η', under which the magnetic field is seen at either pole according to the best-fit values in Table 4.1. Solid and dashed black lines enclose η' values corresponding to the first and second accretion column, AC1 and AC2, respectively, accounting for light bending. Green lines show the case of neglecting light bending.

The larger the viewing angle, the larger is the deviation from the non-relativistic case. For the first column η' varies between 5° and 22° in a small band with mean width ∼1°, whereas for the second column the mean width of the band is ∼11° between 91° and 110°. The second accretion column is only visible due to light bending as it is located on the dark side of the neutron star. Comparing the contribution of the first and the second accretion column to the observed pulse profiles in Figs. 4.1 and 4.2, we see that the first column dominates for all energies. That is also true for the energy band 30–50 keV, which includes the CRSF at ∼37 keV. Consequently the CRSF is mainly formed by the first column, to which the viewing angle is very small (Fig. 4.4) in our best-fit model. CRSFs seen under a small angle to the magnetic field are predicted to be deep and strong (Schwarm et al., 2017b), which is in agreement with the observations of the 37 keV line in 4U 1626−67 (D'Aì et al., 2017, Iwakiri et al., 2018).

Compared to other models put forward for explaining the energy dependent change of the pulse profile of 4U 1626−67, our pulse decomposition explains the observed energy dependent behavior solely by a change in the emission characteristics of the accretion column, without invoking foreground effects. Specifically, the model does not require a reprocessing of the primary radiation in the accretion disk as suggested in the qualitative picture by Koliopanos & Gilfanov (2016). Our model also does not require any absorption by intervening material such as the accretion stream effects proposed by Beri et al. (2014). The simpler explanation is possible by virtue of the low inclination of $i = 10.^{\circ}8$, where relativistic effects allow a complex interplay between the pencil and fan beam to produce the observed profiles. The complexity of the pulse profile modeling does not allow us to quote uncertainties for the fit parameters. However, we note that the inclination is in reasonable agreement with the face on inclination of $\lesssim 8°$ inferred by studies of the orbit of the system that assume that the donor star is a

0.08 $M_\odot$ hydrogen-depleted and partially degenerate star (Levine et al., 1988, Verbunt et al., 1990, Chakrabarty, 1998).

The inclination is in moderate disagreement, however, with the $i \lesssim 33°$ estimate for a $0.02 M_\odot$ helium or carbon-oxygen white dwarf donor (Verbunt et al., 1990, Chakrabarty, 1998). This higher-inclination case is supported by the presence of a complex of broad and double-peaked emission lines around 1 keV (Schulz et al., 2001, Krauss et al., 2007), which are consistent with an inclination in the range of 30–40° (Schulz et al., 2013, Hemphill et al., 2017). The low inclination found by our pulse profile modeling can possibly be reconciled with the high inclination implied by the disk lines if the angular momenta of the accretion disk and neutron star are misaligned. This would result in a strong warp in the accretion disk, which could explain the disk flips that have been invoked to explain the torque reversals of 4U 1626−67 (van Kerkwijk et al., 1998, Wijers & Pringle, 1999).

4.2 The CRSFs in GX 301–2

In the following, my work on modeling the phase dependency of the CRSF line energy in GX 301−2 is presented. This work will be also part of the publication by Fürst et al. (2018), therefore this section is following it closely and in larger parts in verbatim.

The X-ray pulsar GX 301−2 was discovered by balloon experiments in 1969 (Lewin et al., 1971, McClintock et al., 1971) showing pulsations with a moderate pulse period of ∼ 696 s (White et al., 1976). This HMXB (Vidal, 1973, Parkes et al., 1980) has an orbital period of ∼ 41.5 d with an eccentricity of $e = 0.47$ and is located at a distance of 3 kpc (White & Swank, 1984). Accretion in this system takes place by direct accretion from the strong stellar wind. During the orbit a regular pre-periastron flare occurs, which is associated with the neutron star overtaking a dense accretion stream (Leahy, 2002, Leahy & Kostka, 2008).

A CRSF in the hard X-ray spectrum in GX 301−2 was first discovered by Mihara (1995) using *Ginga* data. They found a strong and very broad ($\sigma_{\mathrm{CRSF}} \approx 16.4$ keV) absorption feature at a centroid energy of 35 keV. Their pulse-phase-resolved analysis shows that the line energy varies between 23 and 40 keV. The CRSF was confirmed by Coburn et al. (2002, *RXTE*) and a similar strong phase-dependence of the line energy was found by Kreykenbohm et al. (2004, *RXTE*) and Suchy et al. (2012, *Suzaku*). Depending on the orbital phase La Barbera et al. (2005) found the CRSF at significant higher energies in *BeppoSAX* data, i.e., at around 45–53 keV. An overview of the phase-averaged and phase-resolved CRSF parameters is shown in Figs. 1.9 and 1.10, respectively.

Fürst et al. (2018) analyze observations of GX 301−2 taken with *NuSTAR*, which reveals two distinct, Gaussian shaped CRSFs in the phase-averaged spectra, one at 35 keV and the other at 50 keV. The large line widths of 5 and 9 keV, respectively, cause the lines to overlap. Thanks to the unprecedented spectral resolution of *NuSTAR* it is possible to disentangle the lines. Phase-resolved analyses of the spectra show that the line energies dependent on the pulse phase (see Fig. 4.5). In the following the focus is on the energy of the two CRSFs and their phase dependency. For a full description of the data analysis, spectral model, and spectral fitting see Fürst et al. (2018).

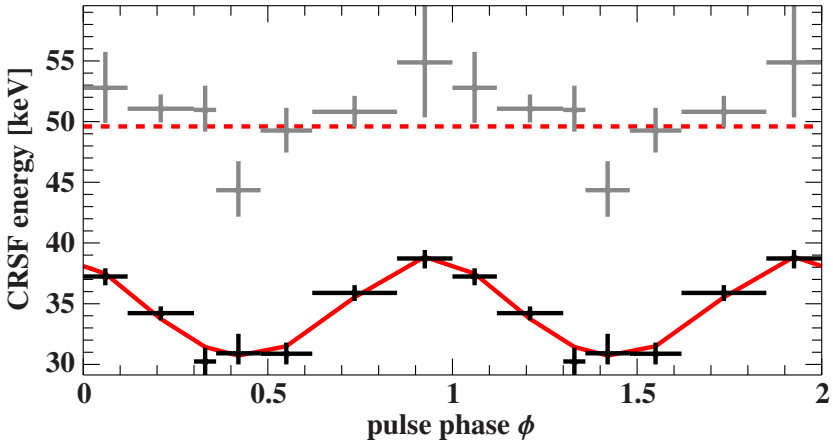

Figure 4.5.: Phase-dependence of the CRSF energies obtained by *NuSTAR* (Fürst et al., 2018), together with the predicted energies by our simple accretion column model in red. The energy of the higher energy line has been fixed to 49.6 keV in the model

4.2.1 The nature of the CRSFs

In about half of the CRSF sources more than one CRSF was measured (see Fig. 1.9). Usually they are interpreted as fundamental and harmonic lines related to the different Landau levels. In that case the energies of the harmonics should be related by integer multiples of the fundamental line energy (Eq. 1.9). Taking into account relativistic effects (Eq. 1.8), the factor between the individual lines can be lower (as seen by Pottschmidt et al., 2005, Müller et al., 2013b). In the case of GX 301−2 the ratio of the two CRSF line energies, however, is ∼1.4, which deviates much more from the factor of 2 than expected (Mészáros, 1992).

It is possible that the two observed lines correspond to the first and second harmonic. In this case we would expect the fundamental line to be at ∼17 keV. Fürst et al. (2018), however, found no evidence for a CRSF at this energy. Previous observations of GX 301−2 also did not show any hint of a CRSF at ∼17 keV (Mihara, 1995, Coburn et al., 2002, Kreykenbohm et al., 2004, La Barbera et al., 2005, Suchy et al., 2012). Spawned photons produced by the radiative de-excitation of the higher Landau levels can cause the fundamental CRSF to be shallower than the first harmonic (Schwarm et al., 2017b,a). This effect is seen in several of the sources shown in Fig. 1.9, e.g., 4U 1907+09 (Hemphill et al., 2013), 4U 1538−522 (Hemphill et al., 2013, Rodes-Roca et al., 2009), and Vela X-1 (Makishima et al., 1999, Maitra & Paul, 2013b, Odaka et al., 2013, Fürst et al., 2014b, La Parola et al., 2016). However, it seems unlikely that photon-spawning would perfectly fill up the fundamental line, without any measurable deviations from a smooth continuum.

The simulations discussed in Chapter 3 show that the shape of the observed CRSFs can differ from a simple Gaussian. The asymmetry is noticeable as a shallow extended lower energy flank. Observations of V 0442+53 (Kreykenbohm et al., 2005, Pottschmidt et al., 2005), Cep X-4 (Fürst et al., 2015), and 4U 1626−67 (D'Aì et al., 2017, Iwakiri et al., 2018) show similar asymmetric CRSFs, which are modeled with a superposition of two Gaussian lines. Therefore it might be possible that there is only a single, but significant distorted line

in GX 301−2. Compared to the examples above, however, the lower energy feature is much stronger and much easier to be identified as an individual line.

Another possibility is that both the CRSFs represent a fundamental line corresponding to two different emission regions. It might be that each line corresponds to an individual accretion column. A highly asymmetric magnetic field would be required to result in fundamental CRSF energies so much apart. Two individual fundamental lines also could be produced by a single accretion column which features two emission regions at different heights. As the magnetic field strength decreases with height so does the CRSF energy.

4.2.2 Modeling the phase-dependence of the CRSF energy

The phase-dependence of the CRSF energy allows us to obtain further information about the accretion and emission geometries. In the following we present a simple model based on the picture of a single accretion column producing the two fundamental CRSF lines at different heights.

The 35 keV-line (CRSF*b*) shows a very significant, almost sinusoidal variation as function of phase (Fig. 4.5). Variations of the CRSF energy are often linked to different heights of the accretion column with different intrinsic magnetic field strengths. Such a clear sinusoidal variation with the rotational phase, however, would indicate we observe emission from a small and confined region of the column moving in altitude with phase. It is unclear how such an emission profile would be produced physically.

The infalling material within the accretion column can obtain relativistic velocities up to $\sim 0.6\,\mathrm{c}$ (Basko & Sunyaev, 1976). Such high velocities will result in the emitted radiation being strongly boosted towards the neutron star's surface. Depending on the viewing angle the emission seen by the observer experiences a significant shift in energy. As the angle of our line of sight towards the velocity vector changes with phase, we will observe different boosting factors and therefore different energies. In this picture the amplitude of the phase variation of the CRSF energy strongly depends on the velocity in the line-forming region. As seen in Fig. 4.5 the phase-dependence of the 50 keV line (CRSF*a*) is negligible, i.e., consistent with a constant within the errors. Therefore a possibility is that the line is formed close to the surface, where the plasma has already decelerated and the bulk velocity is basically 0. In contrast, CRSF*b* is formed much higher in the column where there is a significant bulk velocity. Due to this bulk velocity CRSF*b* experiences a strong relativistic boosting and therefore shows variation with phase.

Here we present a simple model based on this idea. The model features a single accretion column with a negligible radius extended only in height. Adapting Eq. (3.18) the observed CRSF energy at a given rotational phase ϕ is given by

$$E_{\mathrm{CRSF}}(\phi) = E'_{\mathrm{CRSF}}(h)\frac{\sqrt{1-\beta^2}}{1+\beta\cos\eta^\star}\sqrt{1-\frac{R_\mathrm{s}}{R_\mathrm{NS}+h}} \quad , \tag{4.3}$$

taking into account the gravitational redshift (Eq. 2.27) at height h above the neutron star of radius R_NS and with the Schwarzschild radius $R_\mathrm{S} = 2GM_\mathrm{NS}/c^2$ corresponding to its mass M_NS. Also accounted for is the relativistic boosting (Eq. 2.29) due to the local bulk velocity $\beta = v/c$, which depends on the emission angle $\eta^\star$ with respect to the magnetic field in the rest frame of

Table 4.2.: Parameter constraints on GX 301−2.

model parameter	symbol	unit	χ^2-minimization	`emcee`
	free parameters			
observer inclination	i	[deg]	60^{+30}_{-38}	> 20
polar angle of B-field	$\Theta_{\rm AC}$	[deg]	48^{+113}_{-26}	22 - 162
local bulk velocity of CRSFb	β_b		$0.39^{+0.16}_{-0.24}$	0.16 - 0.60
height of emission of CRSFb	h_b	[km]	$0.27^{+0.96}_{-0.27}$	< 1.3
derived intrinsic energy of CRSFb	$E'_{{\rm CRSF}b}$	[keV]	60^{+5}_{-15}	45 - 65
	fixed parameters			
neutron star mass	$M_{\rm NS}$	[$M_\odot$]	1.4	
neutron star radius	$R_{\rm NS}$	[km]	10	
phase offset	$\Phi_{\rm AC}$		0.562 ± 0.025	
observed CRSF energy of line a	$E_{{\rm CRSF}a}$	[keV]	49.6	
intrinsic CRSF energy of line a	$E'_{{\rm CRSF}a}$	[keV]	64.9	

the neutron star (Fig. 3.2). The intrinsic energy of the CRSF in the rest frame of the emitter,

$$E'_{\rm CRSF}(h) = E'_{\rm CRSF}(0)\frac{R_{\rm NS}^3}{(R_{\rm NS}+h)^3} \quad , \tag{4.4}$$

follows a dipolar decrease with h (Eq. 3.11), where $E'_{\rm CRSF}(0)$ is the intrinsic CRSF energy at the neutron star's surface. If the surface B-field strength is known, $E'_{\rm CRSF}(0)$ can be determined using the 12-B-12 rule (Eq. 1.9).

In the simple picture of a cylindrical accretion column with negligible radius, $\eta^\star$ can be identified with the radial emission angle α (Fig. 2.1). Using this identification and the analytical approximation for the light bended photon trajectory (Beloborodov, 2002), $\eta^\star$ can be written as

$$\cos\eta^\star(\phi) = 1 - (1-\cos\Psi)\left(1 - \frac{R_{\rm S}}{R_{\rm NS}+h}\right) \quad , \tag{4.5}$$

where Ψ is the apparent emission angle. From Eq. (2.22) we know the relation between the apparent emission angle and the geometrical setup, which is

$$\cos\Psi(\phi) = \cos i\cos\Theta_{\rm AC} + \sin i\sin\Theta_{\rm AC}\cos(\phi-\Phi_{\rm AC}) \quad , \tag{4.6}$$

where i is the observer inclination, ϕ the rotational phase, and $\Phi_{\rm AC}$ and $\Theta_{\rm AC}$ are the phase offset and the polar angle of the accretion column, respectively (Fig. 3.7).

We now apply this model to the data of GX 301−2. The observed energy of CRSFa is denoted by $E_{{\rm CRSF}a}$ and is set to its weighted mean of 49.6 keV (Fig. 4.5). As $E_{{\rm CRSF}a}$ is formed at the bottom of the accretion column ($h = 0$) where $\beta = 0$, we get an intrinsic energy of $E'_{{\rm CRSF}a} = 64.9$ keV (Eq. 4.3). We use CRSFa to set the intrinsic CRSF energy at the bottom of the column in Eq. (4.4), i.e., $E'_{\rm CRSF}(0) = E'_{{\rm CRSF}a}$. Fitting Eq. (4.3) to the data of CRSFb (Fig. 4.5) we can determine the height (h_b) and velocity (β_b) of CRSFb and the parameters of geometrical setup (i, $\Theta_{\rm AC}$, $\Phi_{\rm AC}$).

A preliminary analysis showed that the phase offset is well constrained and not correlated to any other parameter and is therefore fixed to $\Phi_{\rm AC} = 0.562$. To obtain values for the other

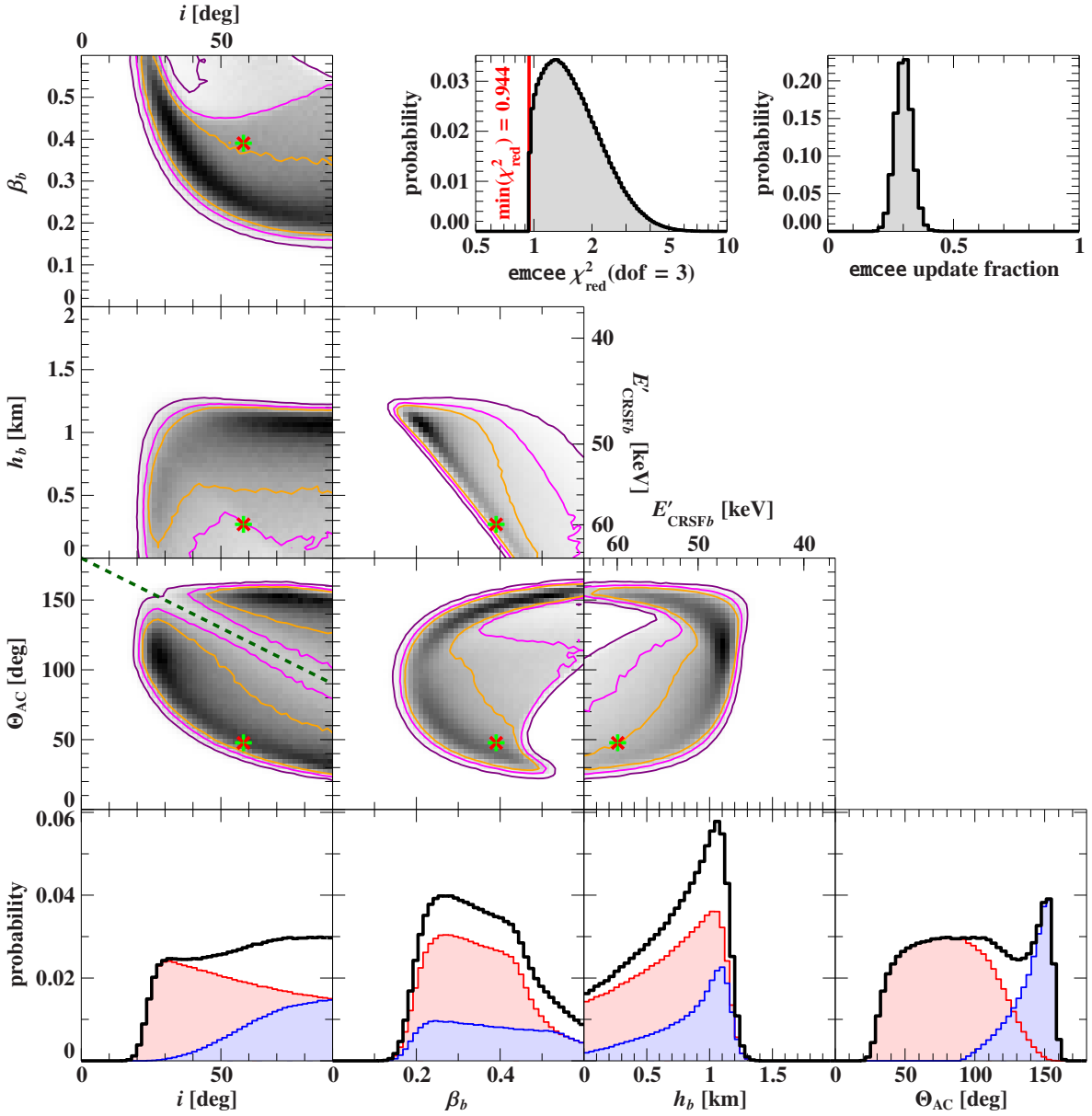

Figure 4.6.: Parameter probabilities obtained from Monte Carlo simulations (`emcee`). Parameter correlations are shown as color-maps, where black corresponds to highest probability. Purple, magenta and orange contours correspond to the 99%, 90% and 68% probability level, respectively. In the i-$\Theta_{\rm AC}$ space there are two distinct probability distributions visible. These two solutions are separated by $\Theta_{\rm AC} = -i + 180°$ (green dashed line), where i is the observer inclination and $\Theta_{\rm AC}$ is the polar angle of the accretion column (see Fig. 3.7). The bottom panels show the one dimensional parameter probabilities, where red ($\Theta_{\rm AC} < -i + 180°$) and blue ($\Theta_{\rm AC} > -i + 180°$) histograms correspond to the individual solutions. The red cross and the green plus indicate the parameter combination corresponding to the minimal $\chi^2_{\rm red}$-value obtained with independently with the `emcee` routine and χ^2-minimization, respectively.

parameters best describing the data we used χ^2-minimization as well as Markov-Chain-Monte-Carlo methods. The latter was performed due to the high degeneracies of the parameters in this simple model. In particular we used the `emcee` routine, which is based upon the parallel "simple stretch" method presented by Foreman-Mackey et al. (2013). The `emcee` routine was applied with 50 free walkers for each free parameter and 100000 iterations, which corresponds to $4 \times 50 \times 100000$ single evaluations. To verify the convergence of the `emcee` run, Fig. 4.6 shows the distribution of the update fraction, which peaks at ~ 0.3 and is perfectly in the preferable range (Foreman-Mackey et al., 2013). Further, the minimal χ^2_{red} of 0.944 and the corresponding parameter combination are identical for the χ^2-minimization and the `emcee` method.

Figure 4.6 also shows the probability distribution of the parameters and Table 4.2 gives the resulting parameter constraints. This simple model provides an excellent description of the observed phase dependence of the CRSF energy, as shown in Fig. 4.5. It also provides some limits on the geometry of the system, for example it indicates an observer inclination $i > 20°$ and a polar angle of the magnetic field $\Theta_{\mathrm{AC}} > 22°$. We obtain bulk velocities between 0.2–0.4 c, which are well in agreement with theoretical calculations. We also find a column height of around 1 km, which is very similar to the height of 1.4 km Fürst et al. (2018) estimated independently from the shock height in the accretion column model by Becker et al. (2012).

Note that in a further step we could assume a certain velocity profile within the accretion column, e.g., the shock model as discussed by Becker et al. (2012). In this case, the velocity below the shock would be much slower, and the emission region would be constrained to be around 1 km. This will lead to better constraints of the other parameters. However, this would introduce specific assumptions about the bulk velocity and the structure of the accretion column. The model as it is presented here is free of any assumption of such kind.

Of course, a possible solution could also include contributions from both accretion columns. However, we do not consider this case here, as we cannot constrain the relative contribution of each column to the observed flux with the available data. In such a model, we would need to make sophisticated assumptions about the altitude-dependent emission profile in each column, which is not necessary in the present setup.

Chapter 5 Conclusion and Outlook

The topic of this work are highly magnetized accreting X-ray pulsars in HMXBs. These neutron stars are amongst the most compact objects we know, with masses of $\sim 1.4\,M_\odot$ and radii of $\sim 10\,\mathrm{km}$. In their vicinity space-time is not flat and general relativity is needed to describe it. In addition these pulsars exhibit strong magnetic fields of $\sim 10^{12}\,\mathrm{G}$ and accretion rates in the order of $\sim 10^{17}\,\mathrm{g\,s^{-1}}$. Such strong B-fields force accreted matter to follow its field lines onto the magnetic poles of the neutron star where accretion columns are formed. There the matter is stopped and its kinetic energy is released, producing an X-ray spectrum roughly following a power-law with high energy roll-over. These spectra often also show broad absorption features caused by cyclotron resonant scattering off electrons forced into quantized Landau levels by the strong magnetic field. Due to the localized emission region at the magnetic poles, which do not have to be aligned with the rotational axis, pulsation with the rotational period in the range of 1–1000 s are visible.

Chapter 2 laid the theoretical foundation for the general relativistic treatment of the photon trajectories based on the Schwarzschild metric. This ray tracing method has no requirements to the geometry of the emission region unlike in other works before, which are restricted to spheric symmetrical hot spots (Beloborodov, 2002, Poutanen & Beloborodov, 2006) or conical accretion columns (Ferrigno et al., 2011). This flexibility is achieved by sampling the emission region with a mesh of triangular surface elements. Each of these elements can feature its own individual emission profile. The emission profile itself may depend on parameters, such as the location, the photon energy, and the emission angle and may even evolve with time. Based on such given emission profiles the ray tracing code calculates the energy- and phase-resolved observed flux accounting for general relativistic effects, such as gravitational redshift and light bending.

Chapter 3 presented the combination of two physical models which describe the formation of the accretion column's continuum emission (Postnov et al., 2015) and the formation of cyclotron resonant scattering features (Schwarm et al., 2017a,b), respectively. The combination of these models yields a physical description of the accretion column's specific intensity, which fits the requirements of the relativistic ray tracing code presented in Chapter 2. Together with

the ray tracing code we self-consistently determine the energy- and phase-resolved flux in the reference frame of the observer.

We discuss the directly observable emission resulting from this physical and self-consistent accretion column model. Our focus is on the implications and predictions on observable quantities derived from the energy- and phase-resolved flux, which are important for interpreting observational data. The main focus is on the general dependency of those observables on the geometrical setup, i.e., the inclination of the observer and the polar angle of the accretion columns. We show that this dependency is strong due to the gravitational light bending. In our investigation we compare single and double column setups and find that including a second column changes the observables substantially, while the impact of asymmetric positioned columns is marginally. We also find that the boosting caused by the high bulk velocity has a significant effect on the observables.

We find that in cases in which one of the columns is on the dark side of the neutron star and roughly aligned with the line of sight, i.e., $i + \Theta_{\mathrm{AC1,2}} \approx \pi$, the effect of light bending is most prominent resulting in strong changes of the observables. We point out that the apparent luminosity derived from the observed flux underlies systematic errors caused by the anisotropy of the neutron star emission, which is enhanced by the effect of light bending. The predicted shape and behavior of the spectral shape and the harmonic CRSF are in agreement with observational results. We find, however, that the predicted fundamental CRSF is solely seen in emission in the phase averaged spectra for any two column configuration. Only in an one-column setup there are geometries allowing to see the fundamental CRSF in absorption.

An advantage of the modular approach of this model is the possibility to modify or replace each individual model with another one or even add a model. This modularity not only allows us to compare different models and their predictions, but also expand our model to include additional effects, which might be important to physically describe the observed emission of accretion columns self-consistently. For instance, the model by Becker & Wolff (2007) could be used to provide the specific intensity of the column. However, it would have to be modified such that it allows to obtain the height and angle dependence of the emission in addition to the spectral information. Another possibility is to add a model which calculates the reprocessed and reflected fraction of the emission intercepted by the atmosphere of the neutron star (Eq. 2.35), which for instance was suggested by Poutanen et al. (2013) to be important for explaining the correlation of CRSF energy and X-ray luminosity.

Future work on this topic is necessary to resolve the discrepancies between models and observations, especially with respect to the fundamental CRSF. The inclusion and comparison of more continuum models that derive height dependent continua and emissivity profiles might give further insights. Especially these models should be applied for a broader range of luminosities and accretion rates to get a more general picture. A more immediate step might be to investigate the indirect emission component given by the reflected fraction of the fan beam emission.

Chapter 4 presented two different applications of the ray tracing code to fit observational data. The pulse profile of 4U 1626−67 shows a particular evolution with energy. At low energies the pulse profile is double peaked with a broad plateau in between, while for increasing energy the double peak diminishes and a broad single peak rises at the location of the plateau. This evolution is well described with a phenomenological emission pattern consisting of a

mixture of a upwards directed pencil and sideways directed fan beam, whose contribution to the emission changes with energy.

GX 301−2 was discovered to exhibit two CRSFs, where the CRSF with a lower energy shows strong variations of its energy with pulse phase while the energy of the other cyclotron line is consistent with being constant. A model featuring a single accretion column with two cyclotron line forming regions at different heights can explain these observations. While the constant CRSF is formed at the bottom of the column, where the accreted matter is settling, the varying CRSF with a lower energy is formed higher in the column where the bulk velocity is still relativistic. The boosting caused by the bulk velocity is dependent on the viewing angle to the column, which causes the apparent variation of this second line.

There is still a huge gap between observational data of highly magnetized accreting X-ray pulsars and their self-consistent and physical interpretation. Although there are many physical models explaining the different aspects in these systems, a combined description of the overall picture is still needed. Pushing forward into this direction of physical models, which take into account the various relevant effects in a common framework, can help to reveal shortcomings in our theoretical understanding. The inconsistency between the predicted and observed behavior of the fundamental CRSF are a good example for this need.

Bibliography

Araya R.A., Harding A.K., 1999, ApJ 517, 334

Baade W., 1938, ApJ 88, 285

Baade W., Zwicky F., 1934, Contributions from the Mount Wilson Observatory, vol. 3, pp.79-83 3, 79

Ballhausen R., Kühnel M., Pottschmidt K., et al., 2016, A&A 591, A65

Ballhausen R., Pottschmidt K., Fürst F., et al., 2017, A&A 608, A105

Basko M.M., Sunyaev R.A., 1976, MNRAS 175, 395

Becker P.A., 1998, ApJ 498, 790

Becker P.A., Klochkov D., Schönherr G., et al., 2012, A&A 544, A123

Becker P.A., Wolff M.T., 2005a, ApJL 621, L45

Becker P.A., Wolff M.T., 2005b, ApJ 630, 465

Becker P.A., Wolff M.T., 2007, ApJ 654, 435

Bellm E.C., Fürst F., Pottschmidt K., et al., 2014, ApJ 792, 108

Beloborodov A.M., 2002, ApJL 566, L85

Beri A., Jain C., Paul B., Raichur H., 2014, MNRAS 439, 1940

Bhattacharya D., van den Heuvel E.P.J., 1991, Physics Reports 203, 1

Bildsten L., Chakrabarty D., Chiu J., et al., 1997, ApJS 113, 367

Blum S., Kraus U., 2000, ApJ 529, 968

Bodaghee A., Tomsick J.A., Fornasini F.M., et al., 2016, ApJ 823, 146

Bonazzola S., Heyvaerts J., Puget J.L., 1979, A&A 78, 53

Burderi L., Di Salvo T., Robba N.R., et al., 2000, ApJ 530, 429

Caballero I., Kraus U., Santangelo A., et al., 2011, A&A 526, A131

Caballero I., Pottschmidt K., Marcu D.M., et al., 2013, ApJL 764, L23

Caballero I., Wilms J., 2012, Memorie della Societa Astronomica Italiana 83, 230

Caballero-García M.D., Camero-Arranz A., Özbey Arabacı M., et al., 2016, A&A 589, A9

Camero-Arranz A., Pottschmidt K., Finger M.H., et al., 2012, A&A 546, A40

Canuto V., Lodenquai J., Ruderman M., 1971, Phys. Rev. D 3, 2303

Canuto V., Ventura J., 1977, Fundamentals of Cosmic Physics 2, 203

Chadwick J., 1932, Nature 129, 312

Chakrabarty D., 1998, ApJ 492, 342

Clark G.W., Woo J.W., Nagase F., et al., 1990, ApJ 353, 274

Coburn W., Heindl W.A., Rothschild R.E., et al., 2002, ApJ 580, 394

Cox N.L.J., Kaper L., Mokiem M.R., 2005, A&A 436, 661

D'Aì A., Cusumano G., Del Santo M., et al., 2017, MNRAS 470, 2457

D'Aì A., Cusumano G., La Parola V., et al., 2011, A&A 532, A73

Davidson K., 1973, Nature Physical Science 246, 1

De Falco V., Falanga M., Stella L., 2016, A&A 595, A38

DeCesar M.E., Boyd P.T., Pottschmidt K., et al., 2013, ApJ 762, 61

Devasia J., James M., Paul B., Indulekha K., 2011, MNRAS 414, 1023

Doroshenko R., Santangelo A., Doroshenko V., Piraino S., 2017, A&A 600, A52

Einstein A., 1905, Annalen der Physik 322, 891

Einstein A., 1936, Science 84, 506

Elsner R.F., Lamb F.K., 1977, ApJ 215, 897

Epili P., Naik S., Jaisawal G.K., 2016, Research in Astronomy and Astrophysics 16, 77

Euclid ca. 300 BC, Elements, Book I

Falkner S., 2013, Light bending around neutron stars, Master's Thesis, FAU Erlangen

Falkner S., Schwarm F.W., Dauser T., et al., 2018a, A&A submitted
Falkner S., Schwarm F.W., Kühnel M., et al., 2018b, A&A submitted
Farinelli R., Ferrigno C., Bozzo E., Becker P.A., 2016, A&A 591, A29
Ferrigno C., Ducci L., Bozzo E., et al., 2016a, A&A 595, A17
Ferrigno C., Falanga M., Bozzo E., et al., 2011, A&A 532, A76
Ferrigno C., Pjanka P., Bozzo E., et al., 2016b, A&A 593, A105
Foreman-Mackey D., Hogg D.W., Lang D., Goodman J., 2013, PASP 125, 306
Ftaclas C., Kearney M.W., Pechenick K., 1986, ApJ 300, 203
Fürst F., et al., 2018, A&A submitted
Fürst F., Grefenstette B.W., Staubert R., et al., 2013, ApJ 779, 69
Fürst F., Kretschmar P., Kajava J.J.E., et al., 2017, A&A 606, A89
Fürst F., Kreykenbohm I., Suchy S., et al., 2011a, A&A 525, A73
Fürst F., Pottschmidt K., Kreykenbohm I., et al., 2012, A&A 547, A2
Fürst F., Pottschmidt K., Miyasaka H., et al., 2015, ApJL 806, L24
Fürst F., Pottschmidt K., Wilms J., et al., 2014a, ApJL 784, L40
Fürst F., Pottschmidt K., Wilms J., et al., 2014b, ApJ 780, 133
Fürst F., Suchy S., Kreykenbohm I., et al., 2011b, A&A 535, A9
Giacconi R., Murray S., Gursky H., et al., 1972, ApJ 178, 281
Gold T., 1968, Nature 218, 731
Haensel P., Potekhin A.Y., Yakovlev D.G., 2007, Neutron Stars 1: Equation of State and Structure, Vol. 326 of *Astrophysics and Space Science Library*, Astrophysics and Space Science Library, Springer, New York
Harding A.K., 2013, Frontiers of Physics 8, 679
Harrison F.A., Craig W.W., Christensen F.E., et al., 2013, ApJ 770, 103
Hemphill P.B., Rothschild R.E., Caballero I., et al., 2013, ApJ 777, 61
Hemphill P.B., Rothschild R.E., Fürst F., et al., 2016, MNRAS 458, 2745
Hemphill P.B., Schulz N.S., Marshall H.L., Chakrabarty D., 2017, In: From Chandra to Lynx: Taking the Sharpest X-ray Vision Fainter and Farther, p. 3
Hessels J.W.T., Ransom S.M., Stairs I.H., et al., 2006, Science 311, 1901
Hewish A., Bell S.J., Pilkington J.D.H., et al., 1968, Nature 217, 709
Hewish A., Okoye S.E., 1965, Nature 207, 59
Ho W.C.G., Lai D., 2001, MNRAS 327, 1081
Isenberg M., Lamb D.Q., Wang J.C.L., 1998, ApJ 505, 688
Islam N., Maitra C., Pradhan P., Paul B., 2015, MNRAS 446, 4148
Islam N., Paul B., 2016, New Astronomy 47, 81
Iwakiri W.B., Pottschmidt K., Falkner S., et al., 2018, ApJ submitted
Iyer N., Mukherjee D., Dewangan G.C., et al., 2015, MNRAS 454, 741
Jaisawal G.K., Naik S., 2015, MNRAS 453, L21
Jaisawal G.K., Naik S., Epili P., 2016, MNRAS 457, 2749
Jaisawal G.K., Naik S., Paul B., 2013, ApJ 779, 54
Karttunen H., Kroeger P., Oja H., et al., 2003, Fundamental astronomy, Springer, Berlin
Klochkov D., Horns D., Santangelo A., et al., 2007, A&A 464, L45
Klochkov D., Santangelo A., Staubert R., Ferrigno C., 2008, A&A 491, 833
Koliopanos F., Gilfanov M., 2016, MNRAS 456, 3535
Kraus U., 2001, ApJ 563, 289
Kraus U., Blum S., Schulte J., et al., 1996, ApJ 467, 794
Kraus U., Nollert H.P., Ruder H., Riffert H., 1995, ApJ 450, 763
Kraus U., Rebetzky A., Herold H., et al., 1989, In: Hunt J., Battrick B. (eds.) Two Topics in X-Ray Astronomy, ESA Special Publication 296, p.433
Krauss M.I., Schulz N.S., Chakrabarty D., et al., 2007, ApJ 660, 605
Kreykenbohm I., Coburn W., Wilms J., et al., 2002, A&A 395, 129
Kreykenbohm I., Mowlavi N., Produit N., et al., 2005, A&A 433, L45

Kreykenbohm I., Wilms J., Coburn W., et al., 2004, A&A 427, 975
Kreykenbohm I., Wilms J., Kretschmar P., et al., 2008, A&A 492, 511
Kühnel M., Fürst F., Pottschmidt K., et al., 2017, A&A 607, A88
La Barbera A., Segreto A., Santangelo A., et al., 2005, A&A 438, 617
La Parola V., Cusumano G., Segreto A., D'Aì A., 2016, MNRAS 463, 185
Lamb F.K., Pethick C.J., Pines D., 1973, ApJ 184, 271
Landau L.D., 1932, Phys. Zs. Sowjet., vol.1, p.285, 1932 (English and German) 1, 285
Lattimer J.M., 2012, Ann. Rev. Nucl. Part. Sci. 62, 485
Lattimer J.M., Prakash M., 2007, Physics Reports 442, 109
Leahy D.A., 2002, A&A 391, 219
Leahy D.A., 2003, ApJ 596, 1131
Leahy D.A., Kostka M., 2008, MNRAS 384, 747
Levine A., Ma C.P., McClintock J., et al., 1988, ApJ 327, 732
Lewin W.H.G., McClintock J.E., Ryckman S.G., Smith W.B., 1971, ApJL 166, L69
Lutovinov A., Tsygankov S., Chernyakova M., 2012, MNRAS 423, 1978
Lutovinov A.A., Buckley D.A.H., Townsend L.J., et al., 2016, MNRAS 462, 3823
Lutovinov A.A., Tsygankov S.S., Suleimanov V.F., et al., 2015, MNRAS 448, 2175
Lyubarskii Y.É., 1986, Astrophysics 25, 577
Maitra C., Paul B., 2013a, ApJ 771, 96
Maitra C., Paul B., 2013b, ApJ 763, 79
Maitra C., Paul B., Naik S., 2012, MNRAS 420, 2307
Maitra C., Raichur H., Pradhan P., Paul B., 2017, MNRAS 470, 713
Makishima K., Mihara T., Ishida M., et al., 1990, ApJL 365, L59
Makishima K., Mihara T., Nagase F., Tanaka Y., 1999, ApJ 525, 978
Malacaria C., Klochkov D., Santangelo A., Staubert R., 2015, A&A 581, A121
Manchester R.N., Hobbs G.B., Teoh A., Hobbs M., 2005, AJ 129, 1993
Marcu-Cheatham D.M., Pottschmidt K., Kühnel M., et al., 2015, ApJ 815, 44
McBride V.A., Wilms J., Coe M.J., et al., 2006, A&A 451, 267
McBride V.A., Wilms J., Kreykenbohm I., et al., 2007, A&A 470, 1065
McClintock J.E., Ricker G.R., Lewin W.H.G., 1971, ApJL 166, L73
Mészáros P., 1992, High-energy radiation from magnetized neutron stars., University of Chicago Press, Chicago
Mészáros P., Ventura J., 1978, Physical Review Letters 41
Middleditch J., Mason K.O., Nelson J.E., White N.E., 1981, ApJ 244, 1001
Mihalas D., 1978, Stellar atmospheres, W. H. Freeman, San Francisco, 2nd edition
Mihara T., 1995, Ph.D. thesis, , Dept. of Physics, Univ. of Tokyo (M95), (1995)
Mihara T., Makishima K., Kamijo S., et al., 1991, ApJL 379, L61
Mihara T., Makishima K., Nagase F., 2004, ApJ 610, 390
Mihara T., Makishima K., Ohashi T., et al., 1990, Nature 346, 250
Misner C.W., Thorne K.S., Wheeler J.A., 1973, Gravitation, W.H. Freeman and Co.
Miyasaka H., Bachetti M., Harrison F.A., et al., 2013, ApJ 775, 65
Mowlavi N., Kreykenbohm I., Shaw S.E., et al., 2006, A&A 451, 187
Müller D., Klochkov D., Caballero I., Santangelo A., 2013a, A&A 552, A81
Müller S., Ferrigno C., Kühnel M., et al., 2013b, A&A 551, A6
Müller S., Kühnel M., Caballero I., et al., 2012, A&A 546, A125
Mushtukov A.A., Suleimanov V.F., Tsygankov S.S., Poutanen J., 2015, MNRAS 447, 1847
Naik S., Maitra C., Jaisawal G.K., Paul B., 2013, ApJ 764, 158
Naik S., Paul B., Kachhara C., Vadawale S.V., 2011, MNRAS 413, 241
Nespoli E., Reig P., Zezas A., 2012, A&A 547, A103
Nishimura O., 2008, ApJ 672, 1127

Odaka H., Khangulyan D., Tanaka Y.T., et al., 2013, ApJ 767, 70
Orlandini M., Dal Fiume D., Frontera F., et al., 1998, ApJL 500, L163
Pacini F., 1967, Nature 216, 567
Parkes G.E., Culhane J.L., Mason K.O., Murdin P.G., 1980, MNRAS 191, 547
Parmar A.N., White N.E., Stella L., 1989, ApJ 338, 373
Pavlov G.G., Shibanov I.A., Iakovlev D.G., 1980, Ap&SS 73, 33
Postnov K.A., Gornostaev M.I., Klochkov D., et al., 2015, MNRAS 452, 1601
Pottschmidt K., Kreykenbohm I., Wilms J., et al., 2005, ApJL 634, L97
Poutanen J., Beloborodov A.M., 2006, MNRAS 373, 836
Poutanen J., Gierliński M., 2003, MNRAS 343, 1301
Poutanen J., Mushtukov A.A., Suleimanov V.F., et al., 2013, ApJ 777, 115
Rappaport S., Markert T., Li F.K., et al., 1977, ApJL 217, L29
Reig P., Coe M.J., 1999, MNRAS 302, 700
Reig P., Milonaki F., 2016, A&A 594, A45
Reig P., Nespoli E., 2013, A&A 551, A1
Riffert H., Meszaros P., 1988, ApJ 325, 207
Rivers E., Markowitz A., Pottschmidt K., et al., 2010, ApJ 709, 179
Rodes-Roca J.J., Torrejón J.M., Kreykenbohm I., et al., 2009, A&A 508, 395
Rothschild R.E., Kühnel M., Pottschmidt K., et al., 2017, MNRAS 466, 2752
Sasaki M., Klochkov D., Kraus U., et al., 2010, A&A 517, A8
Sasaki M., Müller D., Kraus U., et al., 2012, A&A 540, A35
Schönherr G., Schwarm F.W., Falkner S., et al., 2014, A&A 564, L8
Schönherr G., Wilms J., Kretschmar P., et al., 2008, In: 37th COSPAR Scientific Assembly, COSPAR Meeting 37, p. 2781
Schönherr G., Wilms J., Kretschmar P., et al., 2007, A&A 472, 353
Schulz N.S., Chakrabarty D., Marshall H.L., et al., 2001, ApJ 563, 941
Schulz N.S., Marshall H.L., Chakrabarty D., 2013, In: AAS/High Energy Astrophysics Division, AAS/High Energy Astrophysics Division 13, p. 126.46
Schwarm F., Schönherr G., Wilms J., Kretschmar P., 2012, PoS INTEGRAL 2012, 153
Schwarm F.W., Ballhausen R., Falkner S., et al., 2017a, A&A 601, A99
Schwarm F.W., Schönherr G., Falkner S., et al., 2017b, A&A 597, A3
Schwarm F.W., Schönherr G., Kühnel M., Wilms J., 2014, European Phys. J. Web of Conferences 64, 02007
Staubert R., et al., 2018, A&A in prep.
Staubert R., Klochkov D., Vybornov V., et al., 2016, A&A 590, A91
Staubert R., Shakura N.I., Postnov K., et al., 2007, A&A 465, L25
Steiner A.W., Lattimer J.M., Brown E.F., 2013, ApJL 765, L5
Suchy S., Fürst F., Pottschmidt K., et al., 2012, ApJ 745, 124
Suchy S., Pottschmidt K., Rothschild R.E., et al., 2011, ApJ 733, 15
Suchy S., Pottschmidt K., Wilms J., et al., 2008, ApJ 675, 1487
Tanaka Y., 1986, In: Mihalas D., Winkler K.H.A. (eds.) IAU Colloq. 89: Radiation Hydrodynamics in Stars and Compact Objects, Lecture Notes in Physics 255, Berlin Springer Verlag, p. 198
Thorne K.S., 1977, ApJ 212, 825
Trümper J., Pietsch W., Reppin C., et al., 1978, ApJL 219, L105
Tsygankov S.S., Lutovinov A.A., Krivonos R.A., et al., 2016, MNRAS 457, 258
Tsygankov S.S., Lutovinov A.A., Serber A.V., 2010, MNRAS 401, 1628
van Kerkwijk M.H., Chakrabarty D., Pringle J.E., Wijers R.A.M.J., 1998, ApJL 499, L27
Verbunt F., Wijers R.A.M.J., Burm H.M.G., 1990, A&A 234, 195
Vidal N.V., 1973, ApJ 186, L81
Viironen K., Poutanen J., 2004, A&A 426, 985
Vybornov V., Klochkov D., Gornostaev M., et al., 2017, A&A 601, A126
Wang L.J., 2000, Nuovo Cimento B Serie 115, 615
Wang Y.M., Frank J., 1981, A&A 93, 255

Wang Y.M., Welter G.L., 1981, A&A 102, 97
White N.E., Mason K.O., Huckle H.E., et al., 1976, ApJ 209, L119
White N.E., Swank J.H., 1984, ApJ 287, 856
White N.E., Swank J.H., Holt S.S., 1983, ApJ 270, 711
Wijers R.A.M.J., Pringle J.E., 1999, MNRAS 308, 207
Wilms J., 2014, In: European Physical Journal Web of Conferences, European Physical Journal Web of Conferences 64, p. 06001
Wilson C.A., Finger M.H., Camero-Arranz A., 2008, ApJ 678, 1263
Wolff M.T., Becker P.A., Gottlieb A.M., et al., 2016, ApJ 831, 194
Woltjer L., 1964, ApJ 140, 1309
Yakovlev D.G., Haensel P., Baym G., Pethick C., 2013, Physics Uspekhi 56, 289
Zhang C.M., Kojima Y., 2006, MNRAS 366, 137
Zwicky F., 1939, Physical Review 55, 726

Acknowledgments

First for all I want to thank my advisor and 'Doktorvater' Jörn Wilms for giving me the opportunity to do my PhD at the Remeis observatory and contribute scientifically to the topic of accreting X-ray binaries. Thanks to his support and effort to get funding I had the chance to travel to international conferences to present my work.

Now, a chapter of my life is about to end and I want to thank everyone at the observatory for the great time and the support during all these years. I am thankful for the great time with Felicia Krauß and Tobias Beuchert from the beginning of our physic studies until the end of the PhD. Thomas Dauser already guided me through my Master's thesis and I am thankful for his patience in the office answering all my confused questions and all the funny moments. I enjoyed sharing a office with him and Maria Hirsch for all those years. Thanks to Matthias Kühnel, Moritz Böck, and Manfred Hanke I learned a lot about programming and other 'useful' things. My still growing physical understanding is rooted in many fruitful discussions with Matthias Kühnel, Ralf Ballhausen, Felix Fürst, Fritz Schwarm, Gabriele Schönherr and lately also Ekaterina Sokolopa-Lapa. I also enjoyed the discussions within the MAGNET collaboration very much, especially during our collaboration meetings. A special thanks to Maurizio Falanga, Peter Kretschmar, and Katja Pottschmidt for their support.

For me the observatory was not only a place of work, but also a second home thanks to the great community, which managed to create a very pleasant atmosphere. I really enjoyed all the social events, which we had plenty of. I am happy that I was part of the first Remeis Skiing Trip, which became an annual tradition with a lot of 'Hüttengaudi' also with alumni. And thanks to Captain Chaos, I am now confident cruising through deep powdersnow. We had exciting works outings and the 'Bierdiplom' event thanks to Sebastian Müller. For all the unofficial excursions and lots of laughter I also want to thank Cornelia Müller, Eva Ziegerer, Christian Schmidt, Simon Kreuzer, and all the others Remeisen and friends.

Thanks to all of you, who took care of my mental health and made sure that I did not get lost in space. I have many nice and funny memories of my vacation and hiking trips with Christina Gräfe, Johannes Hölzl, Florian Horn, and Ralf Ballhausen, during which I could regenerate and enjoy nature. Andrea Gokus always made me smile and supported me also in my procrastination. Thanks to my roommate, Johannes Veh, I did not starve in the stressful times especially in while finishing this thesis.

There are also people acting in the background ensuring that the observatory is up and running. I want to thank our Professors Horst Drechsel, Ulrich Heber, Jörn Wilms and also Manami Sasaki. Also a special thanks to our Secretary Edith Day for handling all the daily bureaucratic chaos and everyone on the admin-team for maintaining the computer system, with Ingo Kreykenbohm leading the way. I thank Eugenia Litzinger and Ralf Ballhausen for caring for our coffee machine and ensuring the necessary caffeine supply.

Finally, I want to thank my whole family, my parents, and my grandparents, who always supported me in any imaginable way and in all my decisions. They made it possible for me to follow my path.

This research has made use of ISIS functions (ISISscripts) provided by ECAP/Remeis observatory and MIT (http://www.sternwarte.uni-erlangen.de/isis/). The figures in this work

have been produced with the `S-Lang` module `slxfig`. This research has also made use of NASA's Astrophysics Data System Bibliographic Services.